To the University of Wyoming:

The members of the Committee approve[1] the thesis of Dongdong Wang presented on May 15th, 2014.

Dr. Ye Zhang, Chair of Committee

Dr. Dongliang Duan, External Department Member

Dr. Po Chen, Department Member

APPROVED:

Dr. Paul Heller, Department Head, Geology and Geophysics

Dr. Paula Lutz, Dean, College of Arts and Sciences

[1]Signatures on file in the Office of the Registrar.

Physically Based Stochastic Inversion and Parameter Uncertainty Assessment on a Confined Aquifer with a Highly Scalable Parallel Solver

by

Dongdong Wang

A thesis submitted to the University of Wyoming
in partial fulfillment of the requirements
for the degree of

MASTER OF SCIENCE
in
GEOLOGY

Laramie, Wyoming
May 2014

Declaration of Authorship

I, Dongdong Wang, declare that this thesis titled, *Physically Based Stochastic Inversion and Parameter Uncertainty Assessment on a Confined Aquifer with a Highly Scalable Parallel Solver* and the work presented in it are my own. I confirm that:

- This work was done wholly or mainly while in candidature for a research degree at this University.
- Where any part of this thesis has previously been submitted for a degree or any other qualification at this University or any other institution, this has been clearly stated.
- Where I have consulted the published work of others, this is always clearly attributed.
- Where I have quoted from the work of others, the source is always given. With the exception of such quotations, this thesis is entirely my own work.
- I have acknowledged all main sources of help.
- Where the thesis is based on work done by myself jointly with others, I have made clear exactly what was done by others and what I have contributed myself.

Signed: _____

Date: _____

Abstract

Department of Geology and Geophysics

Master of Sciences

by Dongdong Wang

The scope of this research is to investigate the applicability of a new physically based inverse method [1]for aquifer flow inversion, to significantly improve the computation efficiency of the stochastic inverse modeling, and to incorporate uncertainty measures in the inversion outcomes. The problem considered is to invert two-dimensional steady-state flow in a heterogeneous groundtruth model (500×500 grid) with two hydrofacies. From the true model, an increasing number of wells were sampled to obtain facies types, hydraulic heads, and fluxes. Based on experimental indicator histograms and directional variograms computed from the sampled facies, Sequential Indicator Simulation (SIS) was employed to generate 100 hydrofacies realizations with a 100×100 geostatistical grid. Each realization was conditioned to the facies measurements at the wells for which a set of estimated hydrofacies hydraulic conductivities (Ks), flow fields, and boundary conditions (BCs) were estimated using the physically based inverse method.

Because of the parameter quantification, a large number of inverse simulations are needed for which computation efficiency is critical. However, because inverse problems can be ill-posed given insufficient or inaccurate observation data, the inversion systems of equations can exhibit high condition numbers. In such cases, inverse solution time was greatly increased, for which robust, accurate, and efficient solution techniques (i.e., preconditioning and solvers) are needed. First, to improve the condition number of the inversion coefficient matrix, coordinate transform, scaling, and Gaussian Noise Perturbation (GNP) techniques were implemented, which results in a speedup of 200X by calling the same serial iterative solver. Some model reduction studies were also conducted and discussed. Then, to further improve the speed of the iterative solution therefore the inverse problem can be scaled up to much larger grids, a highly scalable parallel solver was developed and implemented. With the parallel solver, it took only 150s (CPU time) to invert a 500×500 problem with 100 processors. A parallel scaling study further reveals that ideal speedup was achieved in solving the inversion matrices Moreover, model reduction is explored to understand the computation-resolution trade-off in inversion. Here, resolution reduction and equation reduction were both explored. Using error-free

observation data sampled from 12 wells (e.g., facies types, hydraulic heads, and fluxes) of a groundtruth model, inversion was carried out with three grids with different heterogeneity resolutions, i.e., a geostatistical facies grid (100×100) generated with Sequential Indicator Simulation (SIS), a Simulated Annealing (SA) grid (100×100) with smoothed heterogeneity, and a coarsened gird (50×50) based on the SA grid. Using the serial iterative solver, the average CPU time for solving these inverse problems was 550s (SIS), 450s (SA), and 330s (coarsened). Compared to the true values, the distributions of Ks exhibit increasing biases: 2%(SIS), 1.6% (SA), 3.5% (Coarsened); the bias of recovered BCs was 0.3% (SIS), 3% (SA), 6% (coarsened).

After computation improvement, uncertainty quantification becomes feasible. The accuracy of inversion is evaluated against: (a) heterogeneity representation and resolution of the inverse problem, (b) observation data quality, and (b) data quantity. Three inverse grids, an SIS grid, a Simulated Annealing (SA) grid with smoothed facies distribution, and a Coarsening gird (50×50), were first inverted using the same error-free data from 12 wells. Conductivities were estimated with a precision of $\pm 0.15\%$ (SIS), $\pm 1.5\%$ (SA), $\pm 3\%$ (coarsened) of their true values, respectively. Compared to the true values, the distributions of Ks also exhibit increasing biases: 0.3% (SIS), 3% (SA), 6% (coarsened). In terms of BC recovery, the uncertainty region was within $\pm 3\%$ (SIS), $\pm 3.5\%$ (SA), and $\pm 1.5\%$ (coarsened) of the true BC, and the bias was 2% (SIS), 1.5% (SA), 3.5% (coarsened). Next, inverse problems (with the SIS grid using the same 12 sampling wells) were solved using observed hydraulic heads that were corrupted by increasingly higher measurement errors (0, $\pm 2\%$, $\pm 5\%$ of the total head variation of the true model). The resultant uncertainty in K estimations was $\pm 7.5\%$ (0), $\pm 9.5\%$ (2%), and $\pm 13\%$ (5%) of the true values, respectively, with increasing biases of 0.3% (0), 6% (2%), and $\pm 29\%$ (5%). The uncertainty of the estimated BCs was $\pm 2.17\%$ (0), $\pm 2.18\%$ (2%) and $\pm 2.02\%$ (5%) of the true BC. Finally, using both static and dynamic(error-free) data sampled from a decreasing number of wells (12, 6, 3), SIS-based facies simulation was carried out and inverted with decreasing data support. The computed Ks were spread over an uncertainty region of $\pm 7.5\%$ (12 wells), $\pm 11\%$ (6 wells), $\pm 19\%$ (3 wells) of their true values, while the accuracy of the recovered BC was within $\pm 3\%$ (12 wells), $\pm 3.17\%$ (6 wells), and $\pm 2.83\%$ (3 wells) of the true BC. In all problems investigated, when the measurement errors are small ($> \pm 2\%$), both the estimated Ks and the recovered BC are centered on the true solutions from the groundtruth model.

Also, some co-effect analyses were conducted to reveal the importance of each factor

to different model evaluation criteria, such as model precision (MP) and model accuracy (MA). After some quantifications, it is obtained that data quantity always play a prominent role in MP and MA. Data quality is critical to MA but has limited influence on MP. The impact of heterogeneity resolution is always mild, which implies the possibility of upscaling and computation-resolution trade-off. In addition, for BCs, different sections exhibit distinctive model behaviors which were discussed also. In general, exploration regions always yield lower precision and poor accuracy, but good robustness to the change of model conditions is also shown in these areas. Finally, decent stability of the uncertainty of MA and MP makes it possible to predict model behavior using observed model status information.

Acknowledgements

First and foremost, I would like to express my sincere thanks to my advisor, Prof. Ye Zhang for her guidance, encouragement, patience, and financial support over the last two years. I would also like to acknowledge my committee members: Prof. Po Chen and Prof. Dongliang Duan for their time and input.

My thanks are also extended to the previous postdoc, Dr. Juraj Irsa for this support in addressing programming problems. I am also extremely grateful to our departmental support, staff and office associates, Alexis Edwards, Diane Gerhart, Deborah Prusia, Genee Vidakovich, and Yaping Zheng for their patience and assistance. In additional to that, I would like to give special thanks to my dear friends for their support.

Finally, I wish to acknowledge the funding source for this study, the Center for Fundamentals of Subsurface Flow, Roy J. Shlemon Center for Quaternary Studies, and the College of Arts and Sciences.

Contents

List of Figures

List of Tables

Abbreviations

BC	**B**oundary **C**ondition
CN	**C**ondition **N**umber
DoE	**D**esign **o**f **E**xperiment
DQl	**D**ata **Q**ua**l**ity
DQn	**D**ata **Q**ua**n**tity
FP-LSQR	**F**ully **P**arallel **LSQR**
GNP	**G**aussian **N**oise **P**erturbation
GTM	**G**round **T**ruth **M**odel
LSQR	**L**east **S**quare **QR**-factoring
MA	**M**odel **A**ccuracy
MP	**M**odel **P**recision
MPS	**M**ultiple **P**oints **S**tatistics
MR	**M**odel **R**eliability
MU	**M**odel **U**ncertainty
OF	**O**bjective **F**unction
PP-LSQR	**P**artially **P**arallel **LSQR**
RHS	**R**ight **H**and **S**ide
SP-LSQR	**S**calable **P**arallel **LSQR**
SA	**S**imulated **A**nnealing
SIS	**S**equepntial **I**ndicator **S**imulation
THV	**T**otal **H**ead **V**ariation
VG	**V**ariogram-based **G**eostatistics
VM	**V**ariogram **M**odel

Physical Constants

Gravity Coefficient $g = 9.81\ \mathrm{m/s}^2$ (approximate)

Symbols

K	hydraulic conductivity	ft/yr
ρ_w	water density	lb/ft^3
Re	Reynolds number	dimensionless
D_H	hydraulic diameter	ft
γ	variogram	ft^2
h	lag distance	ft
h_q	hydraulic head	ft
$\boldsymbol{q}$	flux	ft/s
q_t	tangential flux	ft/s
q_n	normal flux	ft/s
q_x	lateral flux	ft/s
q_z	vertical flux	ft/s
ν_w	water kinematic viscosity	ft^2/s

Dedicated to my parents

Chapter 1

Introduction

Groundwater plays a prominent role in the water resource distribution on the Earth. Groundwater is a critical water resource, providing 30% of the total freshwater on the Earth. In comparison, surface water (all rivers, lakes, soil moisture, and wetlands combined) provides 0.34% of all freshwater, while the remaining freshwater (70%) is mostly locked up in ice and snow at the poles and is inaccessible for use. Apparently, the aquifers beneath the ground provide the largest sources of drinking water worldwide, and understanding the distribution and sustainable use of this resource are of high importance.

Some technical challenges, however, make it infeasible to perceive groundwater distribution pattern physically. First, it is difficult to obtain groundwater data. Groundwater resources are commonly located at least hundreds of feet beneath the land surface, and it is indispensable to drill wells for data sampling which requires complex mechanical techniques. Secondly, the risk of out-of-control water wells limits well drilling and data sampling. Geological structure is usually fragile and cracks on some formations caused by well drilling may lead to liquid flush out without control. One of notorious accident is Gulf of Mexico Oil Spill in 2010. Even if the water spill is not so terrible, the resultant flood and groundwater contamination will be also severe. Therefore, demanding structural geology analysis is obligatory to well drilling in spite of mature drilling technology. Thirdly, extremely high expenditure for each well impedes the increase of sampling wells. Not only does drilling well cost a fortune, but the expenditure of water well maintenance will be exorbitant as well. Accordingly, economic obstacles limit the number of monitoring water wells.

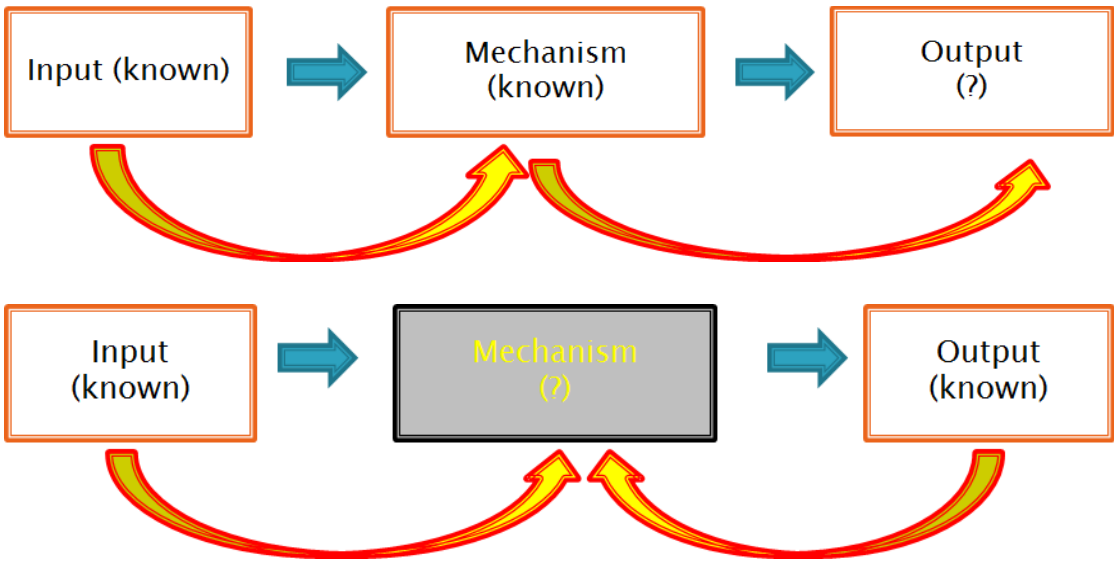

FIGURE 1.1: Forward modeling procedures (above) versus inverse modeling procedures (below). The bent arrows indicate the modeling procedures.

To address this issue, hydrogeologists borrowed the technical supports from computer simulation and developed numerical modeling approaches replacing physical measurement to detect groundwater. In terms of computer simulation, affordable expenses of model development stand out first. Instead of million dollars drilling, computer modeling saves much money as well as takes much less time to obtain accurate subsurface water distribution patterns. In addition, researchers will take smaller risk if numerical modeling is employed to test an innovative idea. Hence, numerical modeling based computer simulation is widely favored by groundwater researchers, and also increasingly developed by hydrogeological modelers. According to the properties of proposed problems, principal modeling approaches consist of forward modeling and inverse modeling. Forward modeling pertains to simulating outputs based on informed input conditions and model mechanism. Inverse modeling involves estimating model structures using groups of input-output data pairs, and thus, it usually refers to parameterization. The comparison between these two modeling techniques is illustrated by Figure 1.1.

Parameterization on an aquifer is always a critical and challenged topic for hydrogeological modelers. In real problems, groundwater modeling usually suffers highly uncertain understanding of model structures, and thus, hydrogeologists are obligated to confront with parameterization difficulties when subsurface aquifers are studied. Meanwhile, accuracy and precision of a parameterization model are considerably constrained by limited access to subsurface, therefore significant uncertainty hinders our ability to use models for water resource management. These facts drive groundwater modelers to explore

highly sophisticated inverse models with well-informed and low uncertainty.

Nowadays, more and more inverse techniques were investigated by hydrogeologists. Generally, these approaches can be categorized into indirect methods and direct methods. In respect of indirect inverse method, hydrogeologists have comprehensively investigated this area (see reviews by, e.g., [4][5][6][7][8][9]). According to different proposed problems, a variety of approaches were put forward, such as imposing parameter bounds of parameter lumping [10], regularization [11][12][13][14], sample network design[15][16][17][18], reducing model structure error[19], adopting a highly parameterized or geostatiscial formulation [20] [21][22][23], incorporating static geologic data[24][25][26], and utilizing auxiliary data such as solute concentration[27][28][29][30], geophysical measurements[31][32][33][34], and temperature[35][36][37]. Direct methods are also explored to parameterize subsurface aquifer and becomes noticeable owing to its mathematical straightforwardness and computational efficiency. Some related exploration studies were accomplished to reveal different problems, such as high sensitivity to data errors at streamlines[38][39][40], reducing uncertainty through imposing bounds on data errors[41], higher accuracy with smaller dimension[42], the parameter and observed data condition for accurate inverse modeling[43]. From the reviews, most research rely on BC and objective function (OF), and both of them induce many problems with significant uncertainties. Therefore, BC and OF are two bottlenecks for groundwater modeling research.

Recently, a novel direct method, which is independent from BC and OF, was proposed by Irsa and Zhang (2012). This approach is developed from a new theory technique, referred to as stress trajectories element method, in geophysics modeling field. Its solution uniqueness and decent stability to data errors [44][45][46] show its potentials to be applied in groundwater modeling. Based on this theory and Darcy's equations, a physically based fundamental solution of inversion is proposed and validated by both a two-dimensional and a three-dimensional inverse problems based on a heterogeneous aquifer with steady state flow[1]. Unlike conventional inverse approaches, this new method directly incorporates corrupted observed data at measurement locations in a single step rather than fits and optimizes an objective function using forward simulation and iterative updates. Also, boundary values and hydraulic conductivities will be assessed instead of being imposed. These breakthroughs definitely render this approach a standout method. However, its limited investigation field constrains the applicability of the method to practical problems. First, researched grid sizes are not comparable to the high resolutions of real problems. The maximum size of tested problem is 32×32

which is far from large enough. Secondly, the proposed fundamental solution relies on the knowledge of the ratio between different hydraulic conductivities which is rarely obtained in real world. Thirdly, computation performance is still not impressive even if it is referred to be computationally efficient. Finally, uncertainty quantification study has not been further explored, and thus, the users fails to have a clear picture for the risks of this method.

This research aims to address these issues and investigate the applicability of the physically based method to large-scale problems. In terms of large aquifer modeling, limited observed data source usually hinders the model development since data sampling requires extremely expensive well drilling. Accordingly, synthetic modeling approaches are widely favored by hydrogeology modelers to test some innovative ideas. Here, a synthetic confined aquifer was developed for inverse research and forward modeling was employed. Chapter 2 will describe the entire implementation procedures as well as discuss and address modeling issues.

The stochastic inversion modeling will be mainly discussed in Chapter 3. This research will modify the physically based fundamental solution [1] to develop a model independent from the ratio between different hydraulic conductivities, and thus, each hydraulic conductivity can be inverted independently and simultaneously. Data integration is implemented to conduct a stochastic inversion. Geostatistical modeling was adopted to integrate static hydrofacies observed data; dynamic hydraulic data were integrated using the new physically based approach. A family of realizations were generated to examine the model accuracy, precision, and uncertainty. Inverted Ks and BCs will be examined to evaluate the quality of inverted results. Uncertainty quantification study in Chapter 6 will also rely on the similar analysis scheme.

The investigation study on a large aquifer also demands for decent computation performance, and thus, solver improvement will be explored in Chapter 4. Since the computation performance of a solver is highly dependent on a proposed problem, a study on the properties of our proposed numerical model was conducted to seek the effective schemes for solver improvement. Based on proposed linear problems, condition numbers (CNs) were examined to reveal some important properties of proposed problems, such as condition, and thus, effective solutions were searched out. In addition to serial solver research, parallel computing was explored to speed up the computation process. For a parallel solver, not only do the features of a problem influence solving efficiency, but parallelization strategies also determine the computation cost. Generally, partition

method and communication study are two central topics for parallelization research. In Chapter 4, both of them will be discussed to develop an highly efficient parallel solver.

With an efficient solver, uncertainty quantification was conducted to investigate the role of different factor in inverse modeling in Chapter 5. Due to data assimilation, our inverse model incorporates many data sources of which each has influence on model quality. To improve the model quality, it is necessary to understand the relation between different data source and modeling outcomes, and then, uncertainty quantification is involved. Many researchers employed this approach to perceive the reliability of inverse model, and also developed many effective methods such as Design of Experiment (DoE). The primary idea is to examine the alterations of model outcomes after a variety of perturbations on each factor or input source, and then, to reveal the link between the model parameters and the model outputs. This investigation study mainly fathomed the roles of three factors, including data quantity, data quality, and heterogeneity resolution, in inverse model. The uncertainty analysis results helped provide advisable strategies for data sampling, thus rendering inverse modeling more efficient, inexpensive, precise, and accurate.

Chapter 2

Forward Modeling

This chapter discusses the approach to develop a synthetic aquifer using forward modeling method. Due to high expense of data sampling in real fields, many hydrogeological modelers usually establish some synthetic models using forward modeling to obtain sampled data and test new ideas. This research also employed this strategy and developed a synthetic aquifer to sample observed hydraulic data. With respect to forward modeling, Finite Different Method (FDM) was adopted to conduct simulation and related conditions were specified based on the property of the studied synthetic aquifer. Mass balance was also examined to validate the aquifer conditions. After the synthetic aquifer was produced, 12 sampling wells as an example were drilled to obtain observed hydrofacies categories, hydraulic heads and fluxes at each well location.

2.1 Finite Difference Method

Recently, increasingly many approaches are developed to establish a synthetic model, such as Finite Difference Method (FDM), Finite Element Method (FEM), and Finite Volume Method (FVM). Among these methods, FEM and FVM are commonly used in three dimensional model research; in particular, FVM will be more effective when the turbulence exists in an aquifer. Concerning our researched problem, i.e., a two dimensional and steady state confined aquifer, FDM is chosen due its generally efficient performance and satisfactory simulation outcomes on the similar problems.

FDM commonly yields a linear equation system when the physical condition of an aquifer is steady-state. For steady-state problems, an equation system is derived from Laplace

Equation (LE) illustrated by Equation 2.1. Since there is no sink or source within the aquifer, the right hand side (RHS) of the equation system exhibits zeros all the time. Based on this equation,a linear hydraulic head approximate function is developed using adjacent four points (Equation 2.2). The estimated location and adjacent observed locations are illustrated by Figure 2.1. A series of equations focusing on different cells can be constructed using this fundamental solution, thus resulting in a linear equation system which is capable of being resolved by appropriate solvers. From the description of FDM, the computation cost is not demanding, and feasible mesh scheme renders an equation system easily developed. Hence, FDM is a good choice for steady-state problem.

$$\frac{\partial}{\partial x}(K_x\frac{\partial h}{\partial x}) + \frac{\partial}{\partial z}(K_z\frac{\partial h}{\partial z}) = 0 \tag{2.1}$$

$$h_{i,j} = \frac{1}{4}[h_{i+1,j} + h_{i-1,j} + h_{i,j+1} + h_{i,j-1}] \tag{2.2}$$

2.2 Synthetic Aquifer Based on Laminar Flow

This research adopted FDM to develop a synthetic steady state confined aquifer as a data sampling field owing to high data sampling expense in real field. Conventional FDM requires two input parameters, including hydrofacies patterns and boundary conditions, and thus, setting these two parameters is a primary step for FDM-based modeling. First, after several reviews, a published hydrofacies pattern [2] illustrated by Figure 2.2 is assigned to true hydrofacies K field since this pattern resembles some true aquifers and its hydrofacies exhibit good heterogeneity with spatial correlation features, both of which facilitate the exploration study for the applicability of our innovative method. According to the hydrofacies pattern, the synthetic matrices were categorized into two hydrofacies: coarse grained sand and fine grained sand in that a common confined aquifer consists of these two materials. According to lithology knowledge [47], the hydraulic conductivities were set to $K_1 = 1$ ft/yr (Silty Sand)and $K_2 = 10$ ft/yr (Clean Sand). Next, boundary conditions were specified by constant heads and no flow boundary according to confined aquifer conditions. In real world, lateral flows are commonly exhibited within aquifers, and thus, constant heads were assigned to the vertical boundary conditions and horizontal boundaries were set to no flow.

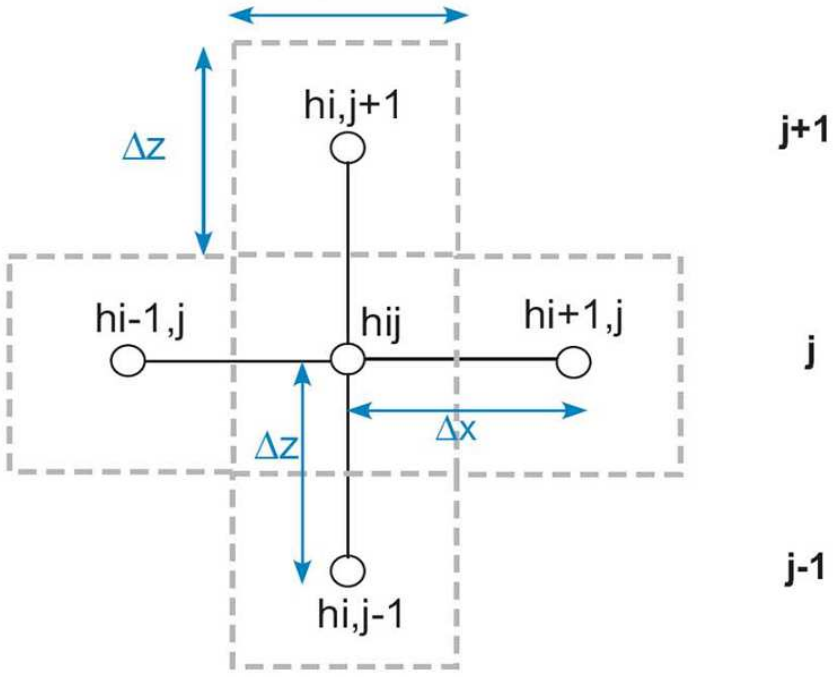

FIGURE 2.1: Primary algorithm description for FDM. The center cell is estimated location and neighbor cells are used to assess the value at the center cell. All of the values are hydraulic heads. Here, the square mesh is adopted and Δx and Δz are equal.

Since our research is focused on Darcy flow study, laminar conditions are required to follow, which is reflected by Reynolds number (Equation 2.3). Based on the architecture of the aquifer, the Reynold's number was calculated to 4, which meets laminar condition. After the condition setting is complete, FDM is ready to simulate the hydraulic conditions of this aquifer which includes hydraulic heads and fluxes.

$$Re = \frac{\boldsymbol{v} D_H}{\nu} \tag{2.3}$$

D_H denotes the hydraulic diameter of the pipe. Here, according to the property of porous media, i.e., sandstones, D_{50} is searched out and chosen as the D_H value. $\boldsymbol{v}$ is the mean velocity of a fluid. Considering the lateral flow pattern of the aquifer, horizontal flux is dominant at velocity components and approximates the velocity as 3.60×10^{-4} ft/yr. ν represents the kinematic viscosity of a fluid. The researched fluid is viewed as pure water, and then, the ν is $1.004 \times 10^{-6} m^2/\text{s}$.

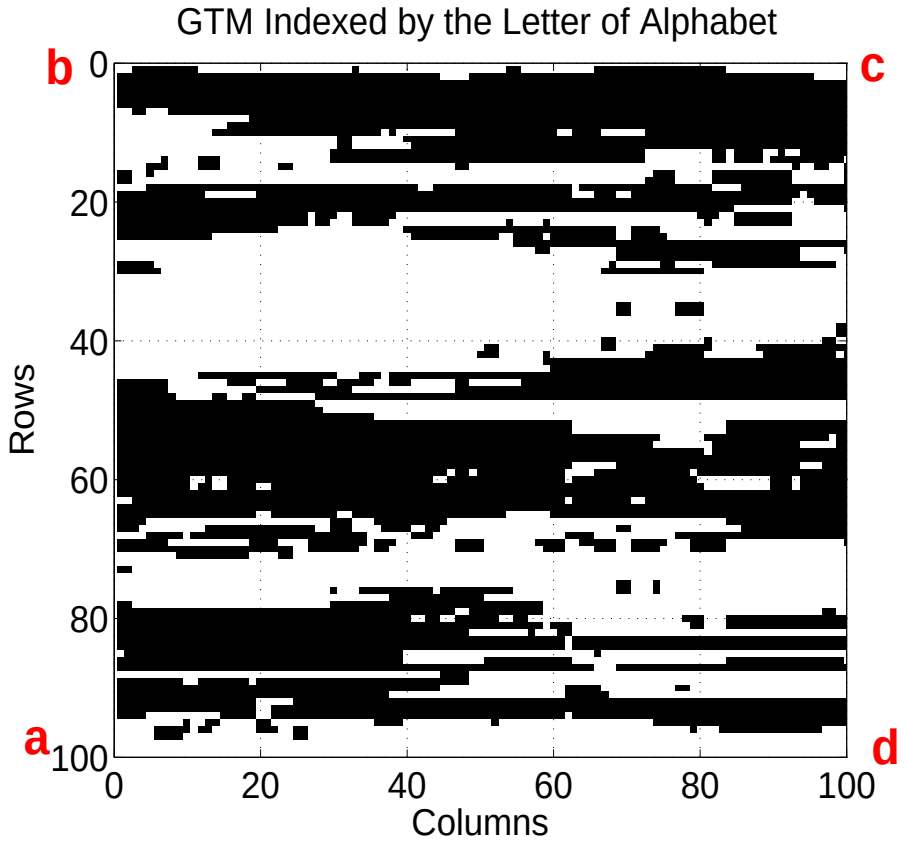

FIGURE 2.2: The hydrofacies pattern [2] for synthetic aquifer. White hydrofacies is Clean Sand and black region denotes Silty Sand. The four corners are indexed by the letter of alphabet for BC research.

In FDM-based forward modeling, the selection of grids plays another prominent role in the quality of simulated results. Since FDM is a discretized solution to a continuous problem, the density of grid cells determines approximate errors, or called discretization errors, which can usually be reduced by using grid refinement. In terms of this problem, the grid cell density was set to 500×500 to ensure relatively low discretization errors. From mass balance checking results (Figure 2.5), the layer-based mass balance is 10^{-7} which indicates the discretization error is reduced to the order of minus seven.

Within the synthetic aquifer, observed hydraulic data were sampled using different strategies. Concerning common hydrofacies patterns in real world, sampling wells were vertically drilled and horizontally distributed (an example based on illustrated by (Figure 2.3)). Hydrofacies categories, hydraulic heads and fluxes were all sampled at each well location. Analogical to a real problem, hydrofacies category data are more than hydraulic head data which are denser than flux data resulting from increasingly demanding technical requirement. The sampled data points are illustrated by (Figure 2.4). Using

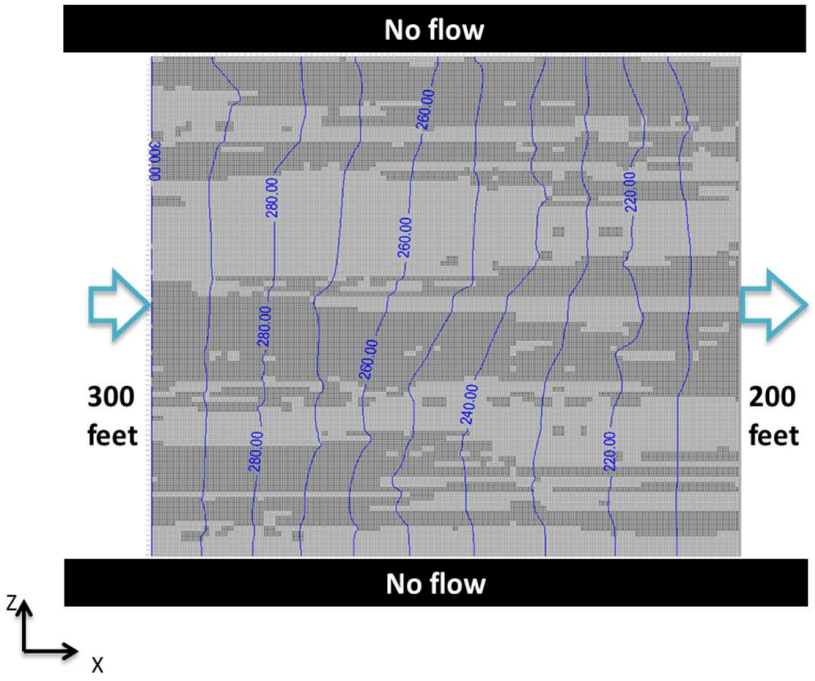

FIGURE 2.3: Synthetic aquifer based on later flow. The hydrofacies pattern, no-flow boundaries, and constant hydraulic heads are specified. The simulation approach is FDM implemented by MODFLOW2000.

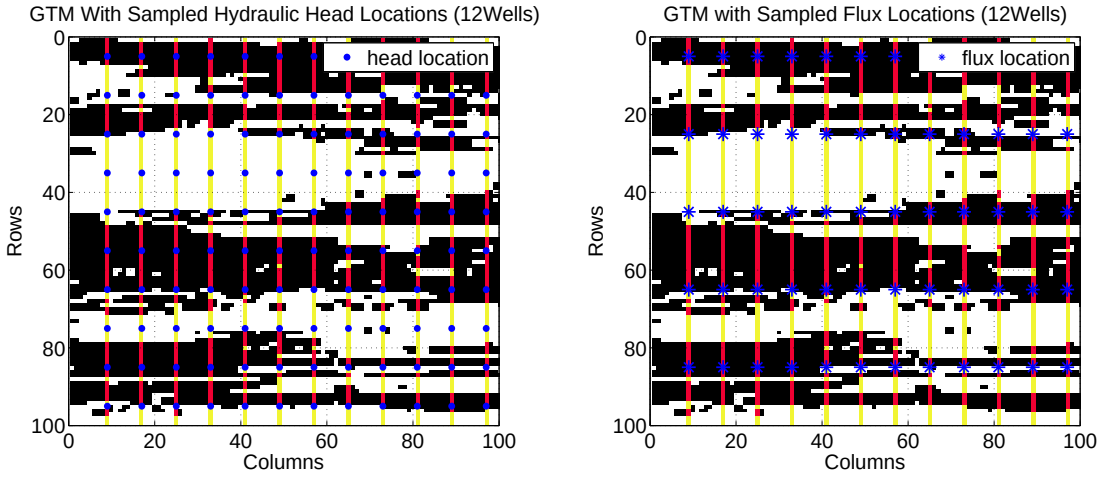

FIGURE 2.4: Sampled Hydraulic Heads and Fluxes. The parallel straight lines denote the drilling wells and dots are sampling locations. Sampled heads are denser than fluxes.

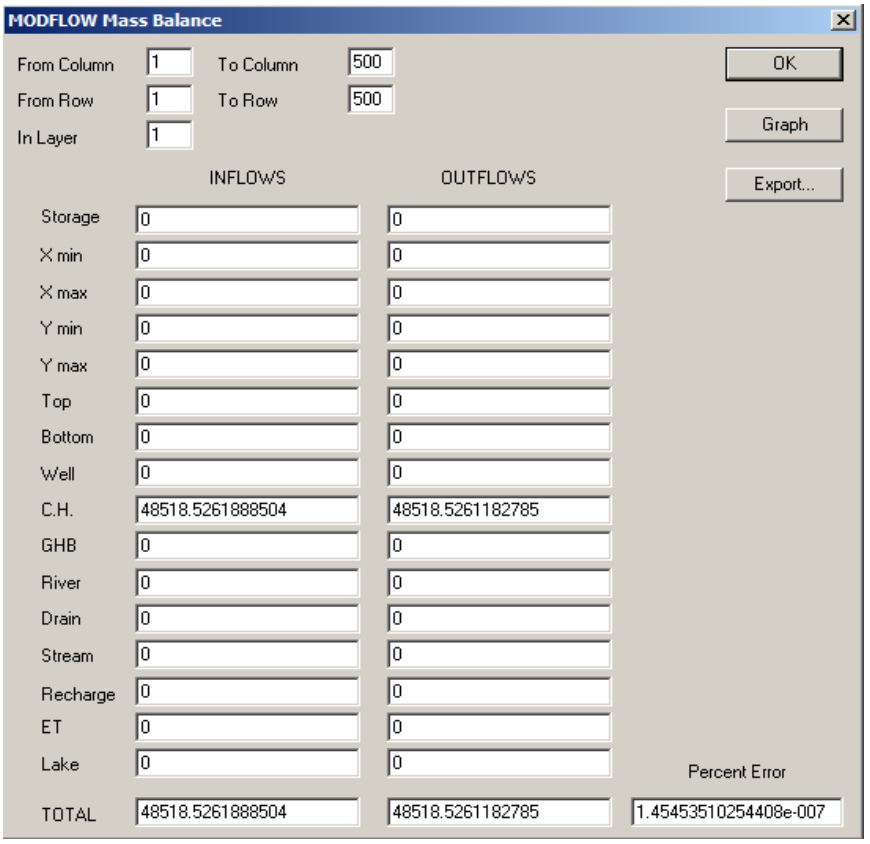

FIGURE 2.5: Model mass balance test. The percent error indicates the model quality. Here, the error is 10^{-7} which indicates the simulated outcomes are reliable. The entire modeling is implemented via GroundwaterVista.

these observation data, different data processing techniques, called data integrations, were conducted to help establish inverse models and parameterize the studied aquifer. This information will be discussed in next chapter.

Chapter 3

Data Integration and Stochastic Inversion

This research adopted data integration and stochastic simulation to address inverse modeling issue. Due to the demand for sufficient observed data, hydrogeological modelers explored many approaches to incorporate more existing data sources. Data integration, as one of the effective methods, is increasingly used for hydrogeological modeling. From the review of papers, this technique has been fully developed and employed to address many inverse problems [48][49][50]. The technique generally incorporates hydrofacies measurements and observed hydraulic data. This research employed this conventional approach and viewed hydrofacies and hydraulic data as static data and dynamic data. Then, stochastic inversion was conducted using static data integration and dynamic data integration.

For stochastic inversion, stochastic simulation is employed in this research. This approach adopts Monte Carlo method to model parametric uncertainties. Owing to lack of the knowledge of true hydrofacies patterns, to understand the uncertainty is taking on an importance. Geostatistics, a branch developed from this field, utilizes spatial correlation information to estimate spatial data distributions. Variogram-based Geostatistics and Multiple Point Statistics dominant Geostatistics modeling sphere.

This chapter will combine these two tactics to resolve inverse problems. With respect to data integration, Variogram-based Geostatistics (VG) is singled out as the approach to incorporate static hydrofacies data while physically-based inverse method [1] is implemented and developed to integrate dynamic hydraulic data.

3.1 Data Integration

Data integration is increasingly widely in use to improve the quality of groundwater modeling. In hydrogeological modeling, data deficiency always affects good model reliability. Many methods are adopted to conquer this obstacle, such as data assimilation [51]. This method effectively break through the bottleneck of limited data sources in that the observed data from different fields, such as lithology and seismology, will be integrated to calibrate a model. The quality of the model is undoubtedly much improved while the expense of data sampling is dramatically cut down.

In this research, two data sources are integrated, including static data and dynamic data. Given the study period, hydrofacies ought to be of no important change, thus facies data are considered as static data; hydraulic heads and fluxes are categorized to dynamic data since they should be changeable in spite of steady-state condition. Corresponding integration strategies are employed to consolidate different data sources.

3.2 Static Data Integration

Static data integration will assimilate hydrofacies data. Usually, most of geophysical sampling data will be taken as static data sources, and here, static data are referred to hydrofacies data. In geological sense, the facies should be changeable due to sedimentary process or metamorphism. In fact, these geological processes commonly involve million year time scale; however, our research period is only focused on the hundred year scale. Therefore, in our researched field, hydrofacies data are able to be taken as constants which do not change with time, and will be integrated as static data sets.

Regarding avenues towards static data integration, hydraulic conductivities were employed to create a bridge between hydrofacies and quantitative modeling. Hydrofacies data are commonly integrated using hydraulic conductivity or permeability. Concerning our fundamental solution developed based on Darcy's law, hydraulic conductivity based integration is more direct and efficient. Different from some conventional methods, this approach viewed hydraulic conductivities as unknowns and estimated these parameters using an inverse model. Accordingly, all hydrofacies categories were identified by indicators and Ks were fully coupled with hydraulic head functions.

Based on the hydrofacies indicators, Variogram-based Geostatistics (VG) is adopted to assess hydrofacies distribution patterns. There are many popular approaches in Geostatistical modeling, such as VG and Multiple Point Statistics (MPS)[52]. MPS usually demands for sufficient data to conduct image training, however, our problem is focused on limited sampled data, and accordingly, VG was adopted as a more effective approach for precise estimation.

VG is variogram based approach and variogram model(VM) is premise. In terms of VM, experimental variogram calculation is required and the method is illustrated by Equation 3.1.

$$\hat{\gamma(h)} = \frac{1}{2N(h)} \sum_{(i,j)\in N(h)} (Z_i - Z_j)^2 \tag{3.1}$$

After experimental variogram calculation, it is necessary to select a representative VM function to fit the variogram scatter points. Primary VM functions include linear model (Equation3.2), Gaussian model(Equation3.3), exponential model(Equation3.4), spherical model(Equation3.5), hole-effect model(Equation3.6), and so forth. Using these models, spatial correlation can be approximated everywhere within the studied aquifer and numerical simulation at each location is feasible.

$$\gamma(h) = C_0 + \frac{h}{A} \tag{3.2}$$

$$\gamma(h) = C_0 + C_1[1 - e^{(-\frac{h}{A})^2}] \tag{3.3}$$

$$\gamma(h) = C_0 + C_1[1 - e^{(-\frac{h}{A})}] \tag{3.4}$$

$$\gamma(h) = \begin{cases} C_0 + C_1[\frac{3}{2}(\frac{h}{A}) - \frac{1}{2}(\frac{h}{A})^3] & \text{if } h < A \\ C_0 + C_1 & \text{if } h \geq A \end{cases} \tag{3.5}$$

$$\gamma(h) = C_0 + C_1[1 - e^{(-\frac{h}{a})} \cdot cos(\frac{h}{b})] \tag{3.6}$$

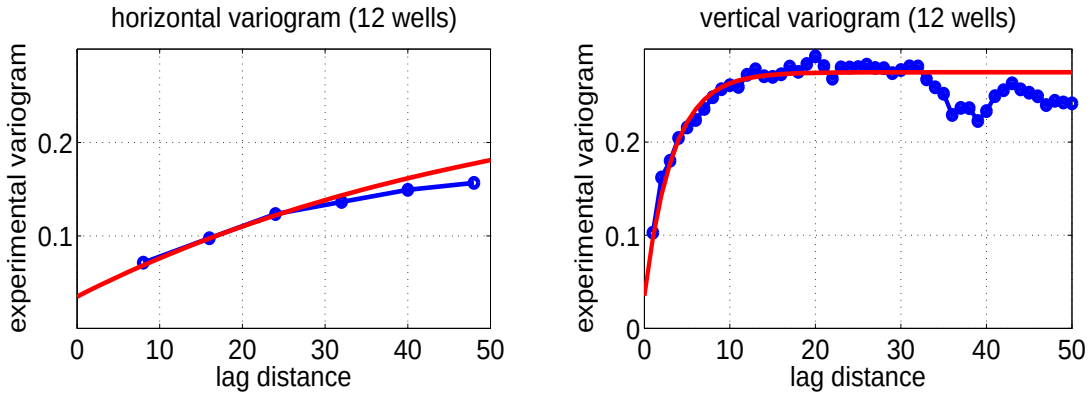

FIGURE 3.1: Variogram model based on 12 wells. The dot lines describe the experimental variograms and the curves are generated from fitting models.

In VG simulation research, Sequential Gaussian Simulation (SGS) and Sequential Indicator Simulation(SIS) are widely in use since both of them are capable of helping understand the reliability of each estimated result. Usually, SGS is adopted when observed variables are continuous; SIS is employed to resolve discrete problems. In this research, hydraulic conductivity categories instead of continuous values and indicator based discrete measurements are exhibited, and thus, SIS is chosen to implement sequential simulation. With respect to SIS, several necessary parameters are required to ensure the reliability of simulation results, including variogram models, indicator histograms, and Kriging data amounts.

A case study is directed using the sampled hydrofacies category data from Chapter 2. First, two hydrofacies were indexed by 1 and 0(white facies denoted by 1 and black facies denoted by 0), and then, indicator based variogram modeling is conducted. An exponential VM is selected to fit the experimental variograms along horizontal direction and vertical direction (Figure 3.1). The VM is yielded illustrated by Equation3.7.

$$\gamma(h) = \begin{cases} 0.035 + 0.24[1 - e^{(-\frac{h}{60})}] & h \leq 48 \text{ along horizonal direction} \\ 0.035 + 0.24[1 - e^{(-\frac{h}{4})}] & h \leq 50 \text{ along vertical direction} \end{cases} \tag{3.7}$$

Next, SIS will be readily implemented using GSLIB [53] open source code. GSLIB is open source code pool developed by Stanford and aims to support spatial modeling research. From this pool, SIS simulation code is obtained; however, some input parameters are still required for its implementation. Variogram model is the first and foremost one. The second important parameter is an experimental indicator histogram. After related

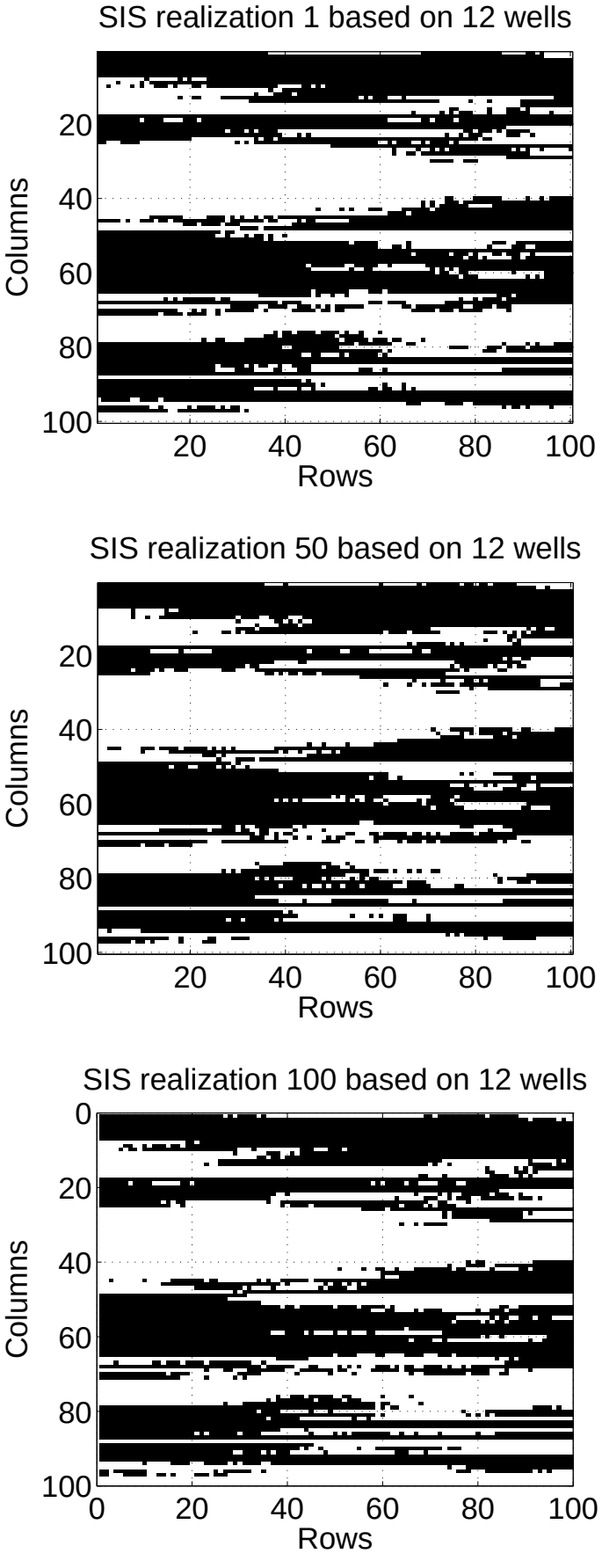

FIGURE 3.2: SIS realization based on 12 wells. Three of the 100 realizations are listed here. Column-row based coordinates are adopted.

calculation, the percentages are 0.504 and 0.496 for hydrofacies category 0 and category 1, respectively. Finally, the amount of Kriging data for each estimated point is also needed. From simulation experiments, the number between 15 and 25 is commonly used to simulate a 100×100 problem, and then, 20 is selected here. Under these conditions, SIS is conducted to simulate 100 realizations as a set of simulation outcomes. Selected realizations are illustrated by Figure 3.2. From the texture of the images, some noisy data are induced at the interface regions due to nugget effect.

3.3 Dynamic Data Integration

This section will discuss dynamic data integration. Concerned dynamic data source includes observed hydraulic heads and fluxes. Although researched problem is a steady state model, hydraulic conditions are usually transient and hydraulic heads and fluxes are dynamically changed in real world. Accordingly, observed hydraulic heads and fluxes, as dynamic data, are integrated using a fundamental solution. Generally, integration solution involves some objective functions from the reviews [54][55]. This research adopted and modified a latest physically based method[1] to assess hydraulic parameters, such as K and h_q. This method is independent from an OF and derived using collocation method. Based on collocation equations and observed data equations, an over-determined linear equation system is developed and solved, and then, hydraulic head parameters and each K are obtained. In particular, some modification on the fundamental solution renders this research solve each K simultaneously without the knowledge of the ratio between them.

The fundamental solution of inversion is derived from steady-state groundwater flow equations using collocation method. The equation describing 2D steady-state groundwater flow without source/sink term is:

$$\begin{aligned} \nabla \cdot (\boldsymbol{q}) &= 0 \\ \boldsymbol{q} &= -K(x,z)\nabla h_q \end{aligned} \tag{3.8}$$

where ∇ is gradient operator, h is hydraulic head, and $\boldsymbol{q}$ is Darcy's flux. According to the primary flow equation, a fundamental solution of inversion is developed based on a quadratic function listed as below:

$$\begin{aligned}\tilde{h}_q(x,z) &= a_0 + a_1 x + a_2 z + a_3 xz + a_4(x^2 - z^2)\\ \tilde{q}_x(x,z) &= -K_x(a_1 + a_3 z + 2a_4 x)\\ \tilde{q}_z(x,z) &= -K_z(a_1 + a_3 x - 2a_4 z)\end{aligned} \tag{3.9}$$

$\tilde{h}_q$ denotes approximate hydraulic head based on flux q. $\tilde{q}_x$ indicates the flux along x axis direction. $\tilde{q}_z$ is the flux along z axis direction. a_i denotes hydraulic head parameters. x and z represent coordinates based on Cartesian Coordinate System. K is a tensor referring to hydraulic conductivity.

According to the quadratic function based fundamental solution, a linear equation system was developed to estimate hydraulic head parameters and hydraulic conductivities. The primary idea is to construct continuity equations and observed data equations. The continuity equations are constructed in following way:

$$\begin{aligned}\delta(p_j - \epsilon)(K_1\tilde{h}_q^{C_m}(x_j,z_j) - K_1\tilde{h}_q^{C_n}(x_j,z_j)) &= 0\\ \delta(p_j - \epsilon)(K_2\tilde{h}_q^{C_m}(x_j,z_j) - K_2\tilde{h}_q^{C_n}(x_j,z_j)) &= 0\\ \delta(p_j - \epsilon)(\tilde{q}_n^{C_m}(x_j,z_j) - \tilde{q}_n^{C_n}(x_j,z_j)) &= 0\\ \delta(p_j - \epsilon)(\tilde{q}_t^{C_m}(x_j,z_j) - \tilde{q}_t^{C_n}(x_j,z_j)) &= 0 \qquad (when\ K^{C_m} = K^{C_n})\end{aligned} \tag{3.10}$$

$\delta(p_j - \epsilon)$ is the Dirac delta weighting function. In spatial science, it is related to the sensitivity of the location. Since this work is still on-going, this value will be set based on equations[1]. K_i denotes the hydraulic conductivity of the ith hydrofacies. $\tilde{q}_n^{C_i}$ is the normal flux at C_i cell and $\tilde{q}_t^{C_i}$ is the tangential flux at C_i cell.

The observed data equations are established using the following method:

$$\begin{aligned}\delta(p_j - \epsilon)(K_i\tilde{h}_q^{C_m}(x_j,z_j) - K_i\tilde{h}_{obs}^{C_m}(x_j,z_j)) &= 0\\ \delta(p_j - \epsilon)(\tilde{q}_n^{C_m}(x_j,z_j) - \tilde{q}_{n(obs)}^{C_m}(x_j,z_j)) &= 0\\ \delta(p_j - \epsilon)(\tilde{q}_t^{C_m}(x_j,z_j) - \tilde{q}_{t(obs)}^{C_m}(x_j,z_j)) &= 0\end{aligned} \tag{3.11}$$

$\delta(p_j - \epsilon)$ is the Dirac delta weighting function. In spatial science, it is related to the sensitivity of the location. Since this work is still on-going, this value will be set based on equations[1]. C_m denotes the cell where observed data are located. K_i denotes the hydraulic conductivity of the hydrofacies within C_m cell. $\tilde{q}_n^{C_m}$ is the normal flux at C_m

cell and $\tilde{q}_t^{C_m}$ is the tangential flux at C_m cell. $\tilde{q}_{n(obs)}^{C_m}$ is the observed normal flux at C_m cell and $\tilde{q}_{t(obs)}^{C_m}$ is the observed tangential flux at C_m cell.

An over-determined linear equation system is developed base on the fundamental solution. Generally, OF based inverse method constrains the solution to satisfy some optimistic conditions, and then, the local optimized solution will be found. Our method also optimized the solutions; however, there is no OF in the inverse model since observed data equations established in the inverse equation system can constrain a series of continuity equations and calibrate inverse solutions. Therefore, this direct method is capable of inverting parameters more efficiently based on the simultaneous equations which can be written as:

$$\boldsymbol{A} \cdot \boldsymbol{x} \approx \boldsymbol{b} \tag{3.12}$$

Here, approximated equal sign was adopted instead of absolute equal sign since an over-determined equation system usually yields a series of approximated solutions rather than a unique solution. According to the approximation property, some numerical techniques were adopted to improve computation performance, and then, uncertainty quantification becomes readily conducted. The related topics will be discussed in the Chapter 4.

Stochastic inversion is readily obtained after two data integrations. The primary scheme is to solve each established equation system using each geostatistics realization (SIS realization), which involves 100 equation systems will be solved, and then, the accessed results will be collected, organized, and interpreted. Since equation systems are developed from continuity equations and data equations, their solutions will be determined by SIS realizations and data sources. SIS realizations refer to heterogeneity resolutions and data source exhibits data quality and data quantity, so the model outcomes depend on data quantity, data quality, and heterogeneity resolution. In respect of these factors, uncertainty analysis was conducted and the work will be discussed by Chapter 6. Here, these three factors are set to 12 wells, no error and 100×100 geostatistics grid (relatively high resoltuion). The correspondent estimated results are presented, including inverted Ks (Figure 3.3)and estimated hydraulic head BCs (Figure 3.4). The reasons why these two results are examined include that K is model calibration criterion which reflects the quality of inverse model, and that the flow pattern within an aquifer is determined and can be evaluated by inverted BC results.

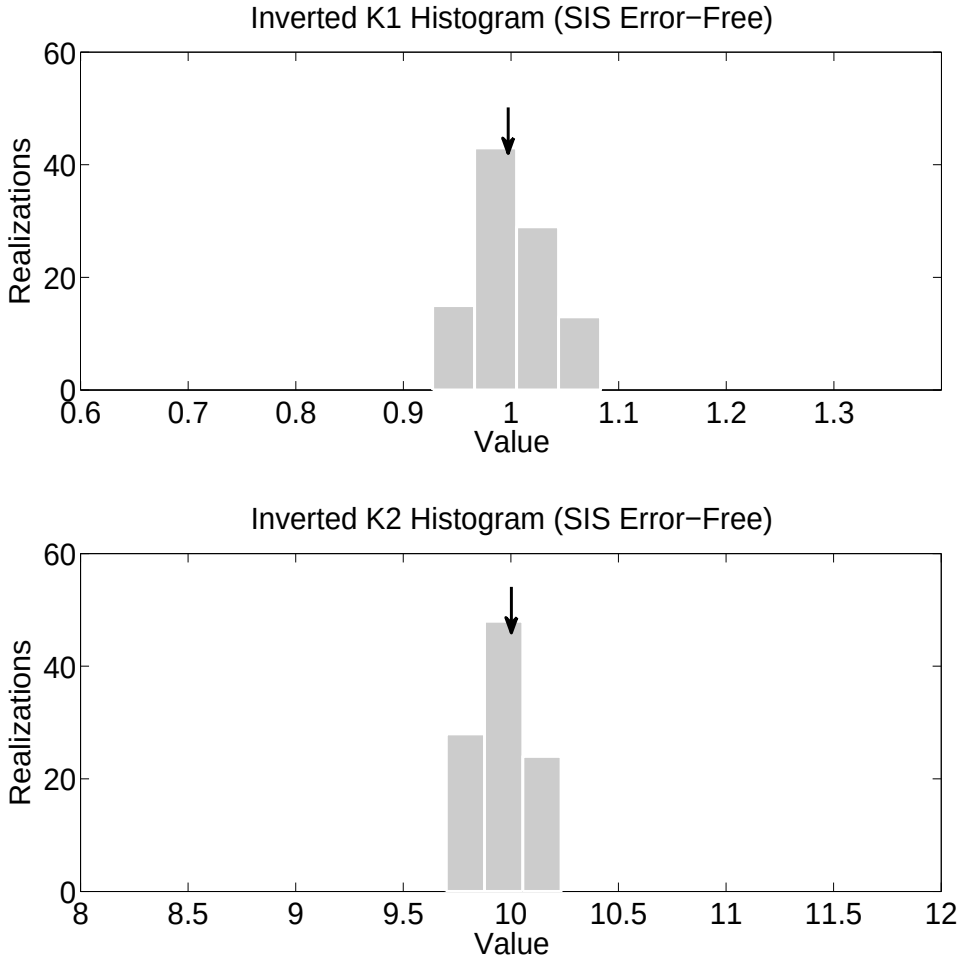

FIGURE 3.3: Estimated Ks using physically based inverse model. The histograms describe inverted results which are centering at the true values.

From the inverted results, Ks are centered at true values. The center of the inverted K_1 distribution lies at 1 ft/yr and the histogram of inverted K_2s is centered at 10 ft/yr. Specifically, more than 80 percent of estimated K_1s spread over the uncertainty region of $\pm 5\%$ of the true value; more than 90 percent of estimated K_2s spread over the uncertainty region of $\pm 2.5\%$ of the true value. Both of them manifest that the accuracy of inverse model is decent and the precision is high. In particular, assessed K_2s exhibit higher precision which indicates high stability to the perturbation of geostatistics grids; compared to K_2, K_1 is more sensitive to the change of heterogeneity resolution resulting from stochastic simulation which implies that the K_1 is more effective to evaluate and calibrate the inverse model.

With respect to BCs, inverted conditions are distributed around the true conditions and lie within the uncertainty region of $\pm 3\%$ total head variation (THV). The recovered BCs

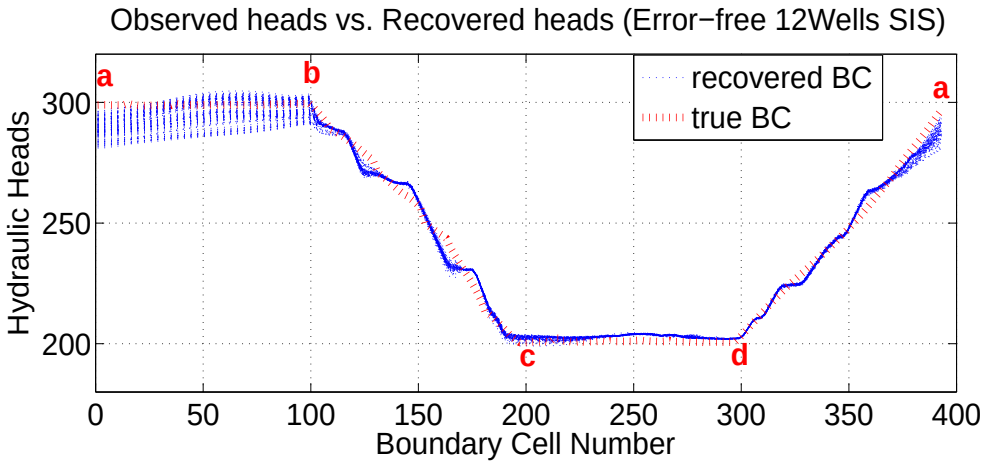

FIGURE 3.4: Assessed BCs using physically based inverse model. The letter of alphabet denotes the boundary corners of studied domain. Estimated BCs are located at the center of a group of resultant BC lines.

are also basically against the true condition. Especially, the Section a-b yields a larger region of uncertainty. This outcome is given rise to by extrapolation which usually exhibits larger uncertainty than interpolation. Also, compared to resultant Ks, BCs exhibit stronger stability to hydrofacies pattern variations and better assessed results.

From the analysis above, both of the resultant distributions are centered at true values with decent uncertainty region. These facts validate the success of the physically based stochastic inversion, including correctly estimating the Ks and the BCs even if some uncertainty exists in the modeling which will be discussed by Chapter 6.

Chapter 4

Computation Optimization

Computation performance bottlenecks the development of hydrogeological modeling research. A practical problem usually require high resolution representation which demands for expensive time cost, so the efficiency of a model is closely linked to its applicability to real problems. Unfortunately, the decent outcomes of hydrological models are usually overshadowed by the deficiency of computation performance. To break through this bottleneck, this research explored some computation strategies to speed up the solver using numerical techniques and parallel computing. First, iterative solver stood out after the comparison study between direct solvers and iterative solvers. Next, iterative solver based serial solver improvement was conducted. CN issue was discussed and some schemes were employed to limit this number, thus accelerating the convergence of the solver and improving its stability to data error. With respect to parallel solver, scalability study was conducted and some partition strategies were explored to implement and develop a highly scalable parallel solver. After the parallelization, the computation time was reduced by order of magnitude.

4.1 Iterative Solver and Direct Solver

Our inverse problem is an over-determinant linear equation system. Generally, two categories of solvers are in use to solve the problem of this kind, including direct solvers and iterative solvers. For a direct solver, inverse operations are conducted directly using the decomposition of a coefficient matrix. Common methods include LU decomposition, Gaussian Elimination (GE), Cholesky Method, QR Factoring Method, and so forth. Iterative solvers start with an initial guess solution and improve the solution each time to

TABLE 4.1: Comparison between iterative solver and direct solver. The time cost denotes the computation CPU time and the solutions are model outcomes of which the true value is 1. The problem size is denoted by the grid size.

	Iterative Solver (LSQR)		Direct Solver (GE)	
Problem Size	solution	time cost(s)	solution	time cost(s)
8×8	0.99991	0.54	0.99991	1.14
16×16	0.99983	4.68	0.99988	135.4
32×32	0.99431	40.31	0.99988	30936

find out the correct answer. The solvers widely used include Jacobi Method, Relaxation Method, Gauss-Seidel Method, SOR Method, and so forth. Generally, direct solvers yield more precise results but consuming computation cost; iterative solvers save much more time but sensitive to the condition of a coefficient matrix which determines the quality of solutions and computation time of a linear equation system. This research also conducted a comparison to reveal the difference between these two solvers in time cost (Table 4.1).

This research adopted an iterative solver to solve our linear equation system. The proposed inverse model exhibits a sparse coefficient matrix and its precision requirement is not demanding due to uncertainty involved in stochastic process, and thus, iterative solvers should be a good option to solve our problems. Meanwhile, iterative solvers are readily parallelized using some strategies, which indicates their potentials for further speed-up. Based on the structure of the developed coefficient matrix, Least Square QR-Factoring (LSQR) iterative solver was selected to solve our inverse equation system due to its high efficiency to sparse matrix problems and a decent stability to ill-conditioned problems. Furthermore, a parallelization on LSQR has been successfully developed by Huang et al.(2012)and implemented on some specific sparse matrix problems [56]. It implies the possibility of the parallelization on the serial solver developed from our inverse equation system. However, decent computation performance of serial iterative solvers is a corner stone for a highly efficient parallel solver, and thus, some serial solver optimizations are required to be explored first.

4.2 Serial Solver Optimization

The condition of a problem plays a prominent role in serial solver optimizations, especially for a linear iterative solver such as LSQR. If a problem is a well-conditioned problem, a solver will reach convergence fast and yield a unique correct solution regardless of

TABLE 4.2: CNs of a problem set. Problem size refers to inverted grid size and heterogeneity pattern is constructed by two lateral hydrofacies layers.

Problem Size	2×2	4×4	8×8	16×16
CN	1.27×10^{17}	3.28×10^{16}	2.05×10^{16}	1.06×10^{16}

corrupted data input; a ill-conditioned problem will result in the slow convergence or even convergence failure of an iterative solver as well as adversely affect the stability of a solver to data errors. As discussed above, evaluating the condition of a problem is critical to a solver speed-up and it is necessary to understand how to define "well-conditioned" or "ill-conditioned" problem . To address these issues, two numerical analysis concepts were explored including condition number (CN) and instability.

4.2.1 Condition Number and Instability

CN is a criterion to evaluate the condition of a linear equation system. If a coefficient matrix exhibits a low CN, the problem should be well-conditioned, or called well-posed, which implies the weak instability to data perturbation. If a coefficient matrix exhibits a high CN, the problem should be ill-conditioned, or called ill-posed, which indicates the strong instability to data perturbation. After the study on our research problem, the CNs of a problem set were listed by Table 4.2. According to tabulated results and CN knowledge, it is readily obtained that our problem is severely ill-posed and some schemes to improve its condition are indispensable. To improve the condition of a problem, it is primary to understand the causes of ill-posedness, including inherent instability and induced instability in general [57].

4.2.2 Inherent Instability

Inherent instability refers to the formulation of a problem. Inherent instability features stem from the proposed method of a problem. A problem is usually proposed by a researcher under some designed structures, such as coordinate systems, equation developments, and fundamental solution. How to design these structures, i.e., the formation of a problem, determines the behavior of proposed problems. Hence, the reformulation of a problem can reduce inherent instability. There are some schemes to change the formulation method for a problem, such as coordinate transform and scaling. Coordinate transform usually modifies some entries of a coefficient matrix and this operation directs the alteration of its norm number, thus changing the condition number. Scaling also

TABLE 4.3: Stretching Experiment (4×4 Problem). Here, sx denotes stretching units along x axis and sy denotes stretching units along y axis.

sx \ sy	1/100	20/100	40/100	60/100	80/100	100/100
1/100	3.42×10^{16}	2.84×10^{17}	1.42×10^{17}	1.23×10^{18}	2.49×10^{17}	3.29×10^{17}
20/100	7.66×10^{16}	1.93×10^{18}	1.99×10^{18}	1.35×10^{18}	5.06×10^{18}	4.08×10^{18}
40/100	1.42×10^{18}	1.35×10^{18}	4.33×10^{18}	8.85×10^{18}	7.88×10^{18}	1.39×10^{19}
60/100	2.47×10^{17}	1.90×10^{18}	5.05×10^{18}	6.40×10^{18}	9.99×10^{18}	1.07×10^{19}
80/100	3.57×10^{17}	6.12×10^{18}	8.13×10^{18}	1.08×10^{19}	2.09×10^{19}	3.13×10^{19}
100/100	4.73×10^{17}	3.51×10^{18}	1.00×10^{19}	7.89×10^{20}	1.35×10^{19}	1.47×10^{19}

induces some adjustments on a coefficient matrix using equivalent equation transform, and then, the coefficient matrix is perturbed resulting in the change of the condition number. The descriptions above imply that coordinate transform and scaling are both focused on some CN adjustment using some modification on coefficient matrix, and this adjustment could be improving or worsening the condition depending on modification strategy. Therefore, based on the two reformulation approaches, numerical experiments were conducted to explore some optimized schemes and weaken inherent instability of the proposed problem.

4.2.2.1 Coordinate Transform

After several numerical experiments, a linear coordinate transform was proposed to relieve the ill-posedness. From the examination on the proposed coefficient matrix, a closely Vandermonde Matrix structure was detected when the grid domain was set from (0, 0) to (100, 100) based on Cartesian coordinate system. Therefore, an experiment was conducted to explore how stretching influences the CN. Take 4×4 for example and the experiment results are listed by the Table 4.4. The tabulated results reveal that the CN reaches a minimum when the stretching ratios along x axis and y axis are both 1/100.

In addition to coordinate stretching, coordinate moving is another important approach for linear coordinate transform. Here, another numerical experiment based on 4×4 problem was conducted to examine the relation between condition number and moving units. The results are listed by the Table 4.3. The tabulated results show that the CN reaches the minimum when the origin point of (0, 0) moves to the origin point of (0, 1).

TABLE 4.4: Moving experiment (4×4 problem). Here, mx is the moving units along x axis and my is the moving units along y axis.

mx \ my	0	+1	+2	+3	+4	+5
0	3.42×10^{16}	1.84×10^{16}	5.03×10^{16}	8.80×10^{16}	5.07×10^{16}	5.54×10^{16}
+1	3.28×10^{16}	3.44×10^{16}	3.65×10^{16}	2.60×10^{17}	6.27×10^{16}	6.26×10^{16}
+2	2.41×10^{16}	6.02×10^{16}	4.73×10^{16}	7.83×10^{16}	7.44×10^{19}	2.00×10^{18}
+3	2.86×10^{16}	1.26×10^{17}	1.50×10^{17}	1.11×10^{17}	1.30×10^{17}	7.61×10^{16}
+4	7.94×10^{16}	8.16×10^{16}	6.89×10^{17}	1.15×10^{17}	1.51×10^{17}	3.85×10^{17}
+5	4.46×10^{16}	3.80×10^{17}	6.67×10^{17}	7.92×10^{16}	1.62×10^{17}	1.53×10^{17}

TABLE 4.5: Equation scaling experiment (4×4 problem). Here, scaling ratio reflects the scaling operation on the coefficients of K related unknowns.

Scaling Ratio	1/100	1/200	1/300	1/400	1/500
CN	1.84×10^{17}	1.84×10^{16}	2.09×10^{16}	2.04×10^{16}	2.92×10^{16}

4.2.2.2 Scaling

Scaling is another useful scheme to reduce inherent instability. The primary idea is to adjust the coefficients of several unknowns using vector unitization. From this description, scaling is able to be taken as a special preconditioning approach which will be discussed by the following section. For our researched problem, scaling is conducted only on the last two column vectors since they refer to observed data equations and the scaling strategy can be simplified. In addition to unitization, several other scaling ratios were tried to modify the coefficient matrix and the results are listed by Table 4.5. From the results, the ratio of 1/200 is an optimum option since the CN reaches minimum.

Some of researchers maintain that model reduction is also an approach to reduce inherent instability. This research views it as a method based on the change of a problem, and thus, it will be discussed in a separated section.

4.2.3 Induced Instability

Induced instability originates from the incorrect selection of a solving strategy. Here, numerical methods will be adopted to modify the solution to an equation system while the formulation of a problem is preserved. Common schemes refer to some operations on coefficient matrices, such as precoditioning. For example, $\boldsymbol{A} \cdot \boldsymbol{x} = \boldsymbol{b}$ exhibits the high condition number of $\boldsymbol{A}$ and the ill-posedness of this problem. If the solution is modified, such as $x_i + h$ instead of x_i, then $\boldsymbol{A}$ will be modified to a new matrix $\boldsymbol{A'}$ of which

condition number is updated. Based on this strategy, some new coefficient matrices will yield much lower CN, thus instability will be much weaken.

4.2.3.1 Preconditioning and Gaussian Noise Perturbation

Preconditioning is a significant approach to address condition number issues. The primary idea of preconditioning is to multiply a precondition matrix at the both sides of an equation system, thus modifying the coefficient matrix and limiting its condition number. Among many preconditioning techniques, perturbation is one of the most effective and inexpensive method, such as Gaussian Noise Perturbation (GNP). This approach is to add a group of random noises to the non-zero entries of the coefficient matrix on which the perturbation will effectively limit the CN increase. Since this operation undoubtedly induces solution errors, the range of noise is usually very narrow, such as $[-10^{-5}, +10^{-5}]$ (Equation 4.1), but the CN will be dramatically reduced while the outcome accuracy is preserved.

$$(\boldsymbol{A} + \boldsymbol{n}) \cdot \boldsymbol{x} \approx \boldsymbol{b} \qquad (\boldsymbol{n} \sim N(0, 10^{-10})) \tag{4.1}$$

For Equation 4.1, $\boldsymbol{n}$ denotes the matrix perturbation noise which follows a normal distribution N centered at 0. The standard deviation of N is 10^{-10} and the expectation is 0.

This research adopted GNP to precondition the developed coefficient matrix and limit the CN. GNP is widely in use to address singular problems, such as signal processing and economic matrix. As a matter fact, there are some similar useful perturbation techniques to improve the condition, such as Tikhonov Perturbation (TP) method (Equation 4.2). Among these approaches, GNP stands out as an inexpensive and effective approach in that white noises are relatively easily generated as well as the perturbation will not severely deteriorate the outcomes. Here, a numerical experiment based on the comparison of TP and GNP was developed to prove this statement (Table 4.6).

$$(\boldsymbol{A} + \lambda \boldsymbol{I}) \cdot \boldsymbol{x} \approx \boldsymbol{b} \qquad (\lambda \text{ is a sufficiently small number.}) \tag{4.2}$$

For Equation 4.2, λ denotes the perturbation constant and $\boldsymbol{I}$ is the unit vector. According to the equation description, the TP perturbs the diagonal entries of a coefficient matrix.

TABLE 4.6: Perturbation technique comparison. λ and n denote the perturbation magnitude. The problem size is denoted by a grid size. True K_1 and K_2 are 1 and 10 respectively. Iteration is the number of the iterations a solver convergence costs.

TP: $\lambda = 10^{-6}$				
Problem	Inverted K_1	Inverted K_2	Iteration	CN
2×2	0.99953	9.9659	327	1.315×10^8
4×4	0.99844	9.7858	12562	7.181×10^7
8×8	0.99319	9.0846	317950	6.0652×10^7
GNP: $n = 10^{-5}$				
Problem	Inverted K_1	Inverted K_2	Iteration	CN
2×2	1.00056	10.0081	328	1.829×10^5
4×4	0.99945	9.9731	2481	6.235×10^4
8×8	0.99804	9.9481	9173	2.823×10^4

4.2.4 Model Reduction

Model reduction is an approach to improve the condition of a problem using some modification on a proposed problem. Since numerical estimation always results in some approximation errors due to truncation or rounding process, to reduce model precision could be a potential approach to trade tiny approximation error for much improvement on the condition of a problem. Meanwhile, tiny approximation error could be reduced by other induced methods, such as grid refinement on mesh-based problems. Therefore, model reduction is widely in use when a proposed problem is large, especially a fine-grid problem. Our problem is 100×100 grid based problem, so model reduction can be adopted to further improve the condition of the problem.

4.2.4.1 Equation Reduction

Our reduction scheme is to modify fundamental solution of the inversion. After the examination on the developed coefficient matrix and several numerical experiments, it was detected that the item of $a_4(x^2 - z^2)$ adversely affect the CN and it is also reducible when the grid is sufficiently refined. Hence, the modified solution after reduction is:

$$\begin{aligned} \tilde{h}_q(x,z) &= a_0 + a_1 x + a_2 z + a_3 xz \\ \tilde{q}_x(x,z) &= -K_x(a_1 + a_3 z) \\ \tilde{q}_z(x,z) &= -K_z(a_1 + a_3 x) \end{aligned} \tag{4.3}$$

TABLE 4.7: Equation reduction timing experiment (hours). The fundamental solution is simplified and Laplace equation is still followed.

	4×4	16×16	64×64	256×256
Original Equation	6.943×10^{-6}	2.883×10^{-3}	2.529×10^{0}	1.387×10^{2}
Reduced Equation	2.222×10^{-6}	4.094×10^{-4}	6.042×10^{-2}	2.596×10^{0}

Based on this approximation function, the CN is further reduced and timing experiment results are listed by Table 4.7. The lower precision is traded for CN reduction; however, this trade-off strategy is profitable. From the numerical experiment, the CN is limited by 5 orders of magnitude while the precision is reduced by 2 digits. This superiority will be more noticeable when the problem size increases since the grid refinement will improve the precision, thus reducing the result deterioration by model reduction. From Table 4.7, the time cost is reduced by 2 orders which implies the solving large problem is feasible. Accordingly, model reduction is a good approach to improve the condition of a high-resolution problem.

4.2.4.2 Resolution Reduction

Resolution also plays a prominent role in computation performance. High resolution must result in high computation cost while calculation results yield high precision and decent accuracy. However, in a practical problem, the precision and accuracy requirements are not demanding since some other factors, such as measurement errors and equipment bias, have contaminated model outcomes. Accordingly, hydrological modelers explored some methods, such as upscaling, to take advantage of uncertainty to trade resolution reduction for high computation efficiency. This research also explored a computation-resolution trade-off strategy. Based on simulated annealing (SA) strategy, heterogeneity resolution is smoothed; coarsening operation renders the resolution further smoothed. The comparison between different resolution grids is illustrated by Figure 4.1. The average computation time is 550s, 450s, and 330s for SIS grid, SA grid, and Coarsening grid. More details on the model uncertainty study will be discussed in Chapter 5.

4.2.5 Improved Results

After these numerical and modification approaches, the condition of the propsed problem was much improved and thus, the performance of LSQR serial solver became decent.

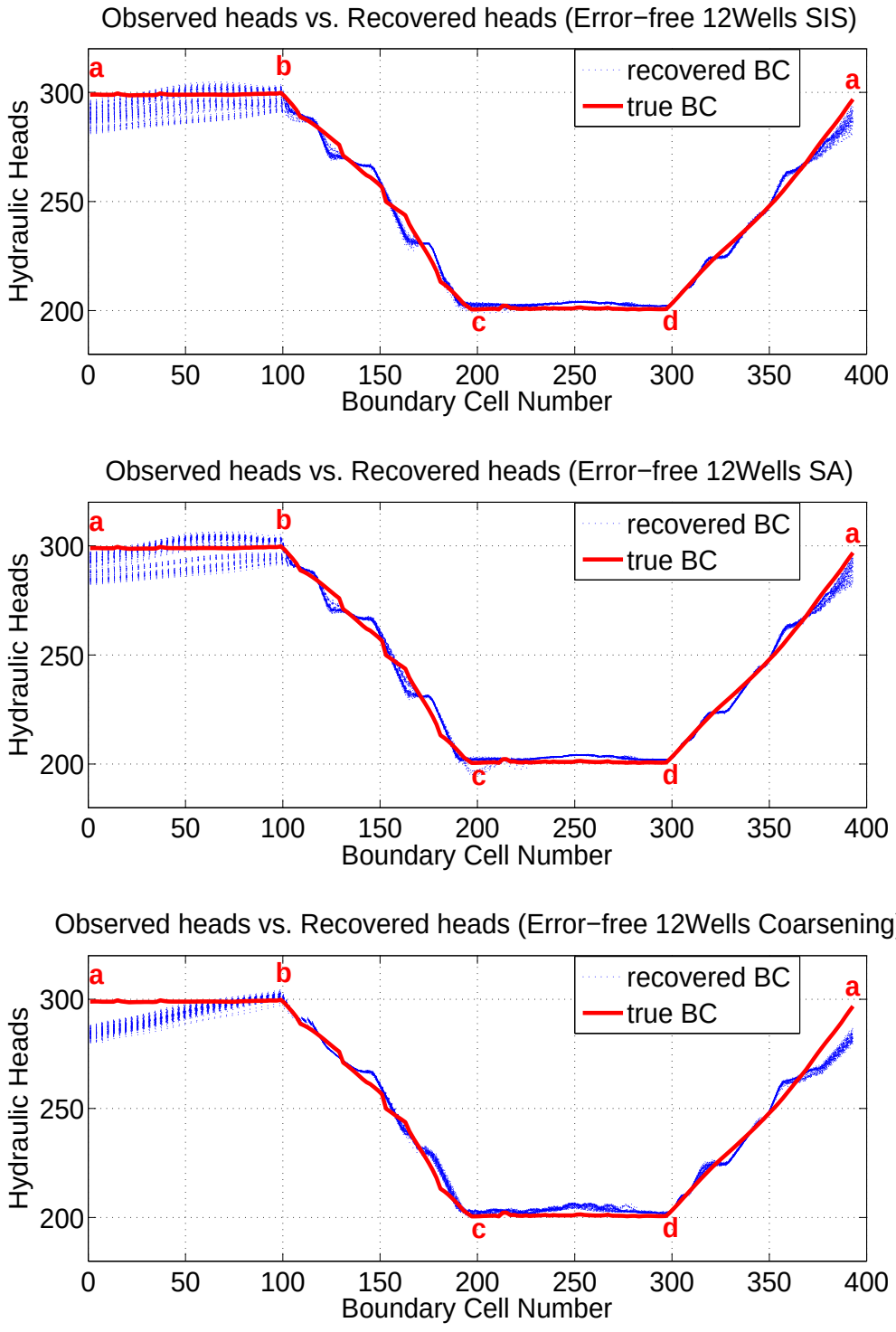

FIGURE 4.1: Resolution reduction experiments. Here are three experiments using different grid resolution including SIS grid, SA grid, and Coarsening grid. The grid size is 100×100 all the time.

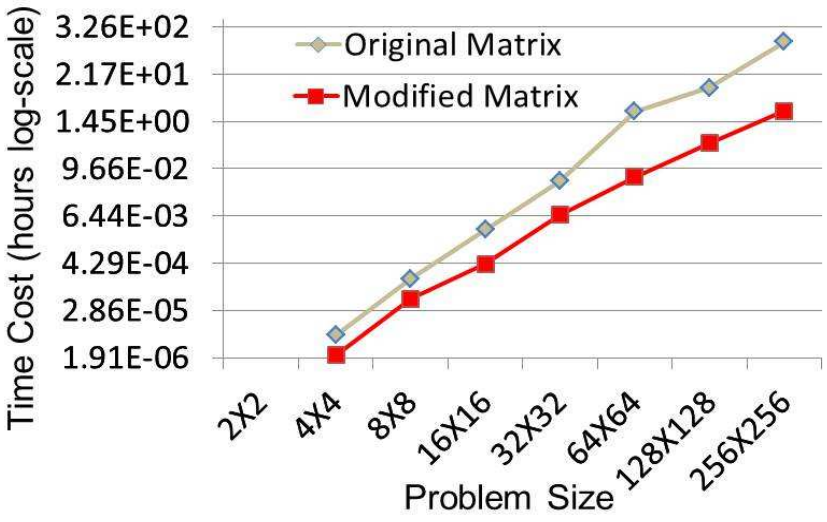

FIGURE 4.2: Serial solver improvement results. Time cost denotes the CPU solving time and problem size represents the grid size. Modified matrix results in computation improvement with order of magnitude.

From the experiment results by Figure 4.2, a 200×200 problem saves approximately 200 times of time after the series of operations. For a stochastic inversion based on 100×100 grid, a family of problems (100 realizations) can be solved in approximately 14 hours instead of 1400 hours.

4.3 Parallel Computing

With increasingly high resolution of aquifer representation, conventional serial solvers are not able to satisfy the demand for computation performance, and parallel solvers are widely in use to model large-scale aquifers, especially for inverse problems. The primary idea for a parallel solver is to partition a large problem into several smaller sub-problems which will be launched at different processors, and then, these problems will be simultaneously solved by different processors. This approach is capable of improving computation efficiency and decent results reply on partition schemes.

Partition strategy research plays a prominent role in parallel solver development. A number of algorithm explorers devote much time to studying different problems and investigating partition tactics to refine the performance of a parallel solver. Why does

partition process govern parallel computing research? The first key answer is related to the communication between different processors. After partitioning, a whole problem is separated into several pieces yielding meaningless solutions, and thus, it is necessary to assemble these fragmental answers into a meaningful solution. This assembly procedure is conducted by communication between different processors, and its time cost is determined by information transmission which relies on information amounts. A poor partition strategy will load much unnecessary information on transmission process, thus adversely affecting computation performance.

The second important factor is loading balance on all processors. Since the assembly procedure ought to be complete after all processors finish their own tasks, some processors must wait for others on pending status although they have accomplished their duties. This waiting time definitely extended the processing, and thus, some optimization on task allocation, i.e., loading balance should be conducted to speed up a parallel solver. The task allocation tactics also depend on partition schemes.

Hence, disparate partition strategies will lead to different parallel solver performance which necessitates a clever partition scheme. Here, three kinds of partition strategies were explored to optimize the computation performance, thus leading to three parallel solvers, including Partially Parallel LSQR (PP-LSQR), Fully Parallel LSQR (FP-LSQR), and Scalable Parallel LSQR (SP-LSQR).

4.3.1 Partial Parallel LSQR (PP-LSQR) Solver

PP-LSQR is implemented based on a partial partition strategy. This partial partition is a basic method to parallelize any solver and generally introduced in computation method courses. Many sophisticated partition algorithms are developed from this primary idea although it is elementary. Its main scheme is to partition the coefficient matrix and the right-hand-side(RHS) vector in an equation system based on rows using linear algebra knowledge. This process is briefly described by the Figure 4.3. From this illustration, the entire equation system is divided into several smaller independent problems which could be simultaneously solved by different processors.

However, there are several issues behind this picture. First, the unknown vector $\boldsymbol{x}$ will prolong the processing time. Due to the failure to partition this vector, it will be processed repeatedly by different processors. This fact implies the task loading is increased, thus costing longer processing time. Secondly, communication time is able to

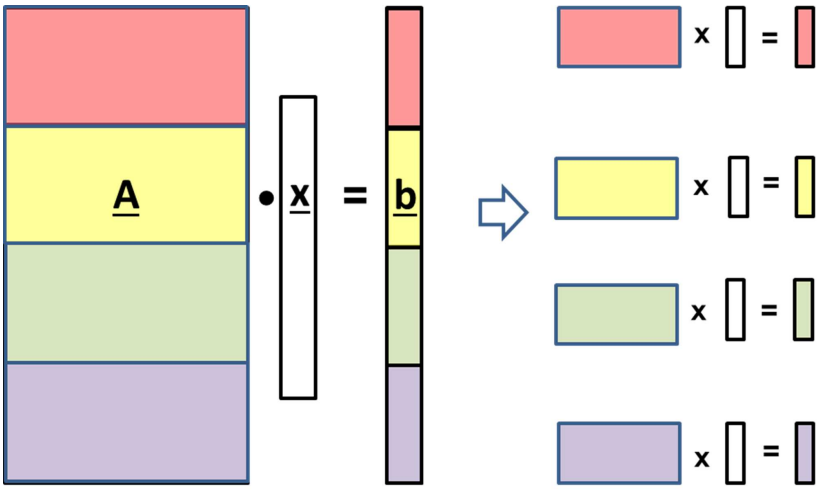

FIGURE 4.3: PP-LSQR Partition Scheme. A denotes co-efficient matrix, b is right-hand-side vector, and x is unknown vector. All of them are partition based on rows using linear algebra knowledge.

overshadow the advantage of parallelization. Iterative solvers require the update on the coefficient matrix and the RHS vector consecutively, and thus, the assembly has to be directed at each iteration and communication efficiency plays a prominent role in solver performance. According to the row-based partition scheme, when a problem is separated into more pieces or a problem size is increased, the overlap between different partitioned blocks will be exponentially longer, which indicates the information transmission takes much more time. Hence, the partition strategy results in poor communication performance.

According to the analysis above, PP-LSQR is able to improve computation efficiency when the size of a problem is small and the number of used processors is limited. In terms of a large real problem, problem size will hinder the attempt to improve computation time, and the demand for large amounts of processors will cause even higher time cost.

4.3.2 Fully Parallel LSQR (FP-LSQR) Solver

FP-LSQR solver is developed to address the issues caused by PP-LSQR. This full parallelization scheme breaks through the task loading issue and relieves communication block problems. The primary idea is to partition the coefficient matrix by columns instead of rows, and then, the unknown vector $\boldsymbol{x}$ is successfully partitioned using linear

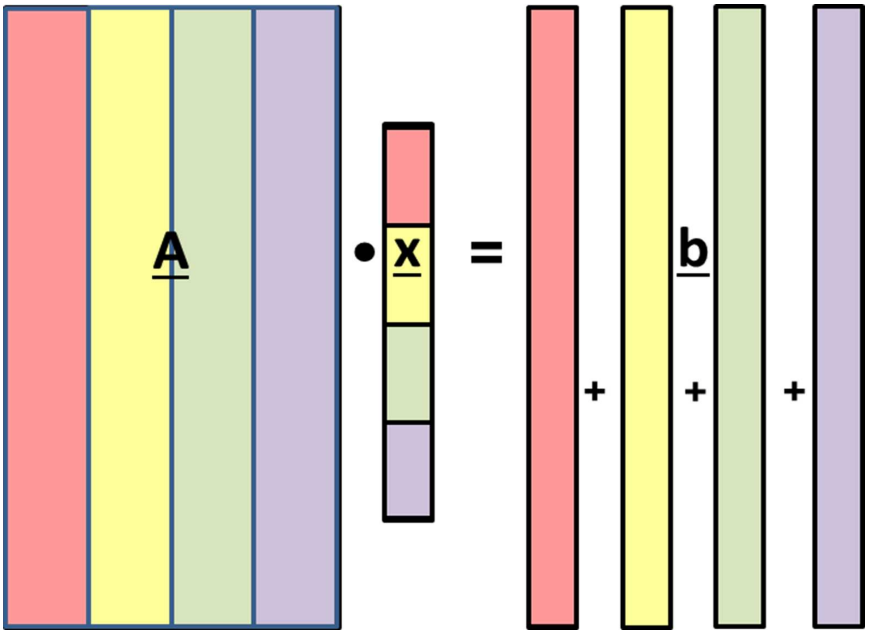

FIGURE 4.4: Fully Parallel LSQR Partition Scheme. A denotes coefficient matrix, b is right-hand-side vector, and x is unknown vector. All of them are partition based on columns using linear algebra knowledge. Here, b is partitioned to a sum of single vectors.

algebra knowledge. This strategy is illustrated by Figure 4.4. Furthermore, loading balance scheme is employed to improve computation performance. Using column based data storage, retrieving entry by columns will be feasible, and then, the total number of the non-zero entries can be obtained. According to the usage of processors, it is possible to balance the task loading on each processor if some efficient retrieval algorithm is designed. As a matter of fact, this bottleneck has been broken through, and based on the developed algorithm [58], the loading on each processor is optimized and closely balanced.

FP-LSQR seems to improve the performance successfully; however, the timing plots shown by Figure 4.5 revealed some computation issues. After limited computation improvement, the time cost of FP-LSQR exhibits increase trend which implies the parallel computing fails to speed up the solver. The reason for the computation performance is the dominant communication time between processors restricts the computation improvement. For parallel computing, communication is indispensable since the pieces of meaningless results calculated by each processor must be united to update residual

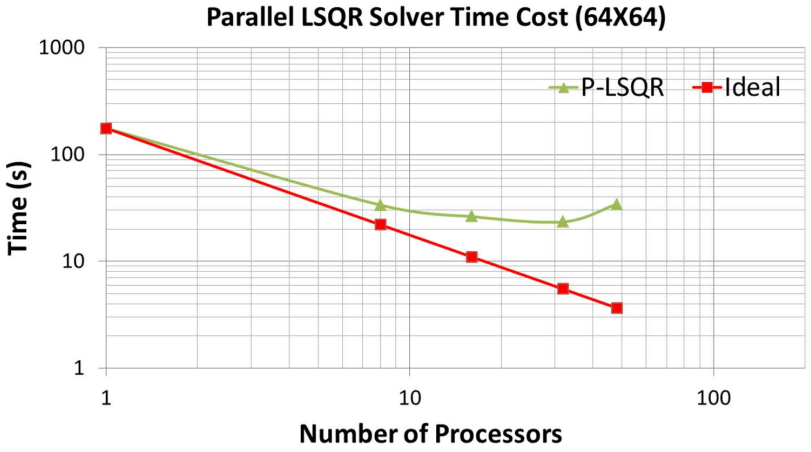

FIGURE 4.5: Fully parallel LSQR timing plots. Time denotes computation CPU time and number of processors is how many processors are used to compute the partitioned problems.

vectors and search final solutions until the convergence is reached. This communication relies on the overlap information between smaller partitioned blocks and its time cost will be longer if the overlap information increases. For FP-LSQR, the overlap information will exponentially grow with the increase of problem size and processors due to its column-based partition strategy. Hence, FP-LSQR will fail to save time cost after communication starts to be dominant. Meanwhile, the column-based partition scheme will induce many zeros during vector calculation and communication and hinder the computation speed-up since our problem exhibits extremely sparse matrix. More details were discussed in the related published work [58]. Due to this issue, a scalable study was conducted to break through this bottle neck.

4.3.3 Scalable Parallel LSQR (SP-LSQR) Solver

Scalable Parallel LSQR solver is developed by dividing a coefficient matrix to a kernel sub-matrix and a damping sub-matrix. Scalable solver yields high scalability which implies decent independency from problem sizes and the number of processors. A good parallel solver usually counts on high scalability, and thus, a number of computer scientists devote much time to exploring scalability study. This SP-LSQR is also developed from the scalability study outcomes [3]. Its scheme tries to divide a coefficient matrix into a dense sub-matrix, i.e., a kernel matrix, and a sparse sub-matrix, i.e., a damping

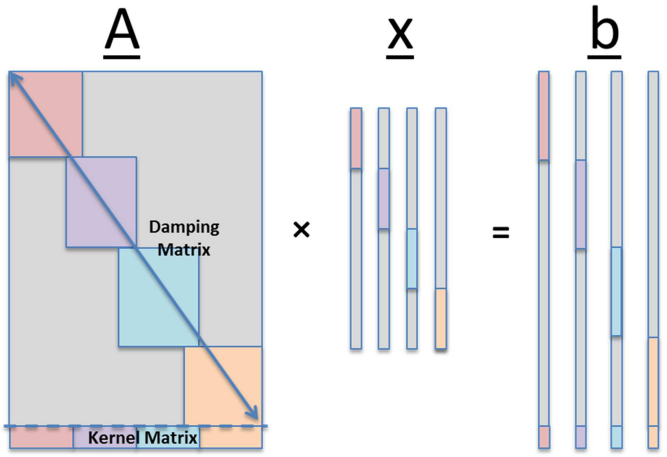

FIGURE 4.6: SP-LSQR partition strategy [3]. A denotes coefficient matrix, b is right-hand-side vector, and x represents unknown vector. In the matrix A, block based region is called damping matrix and column based region is called kernel matrix.

matrix, and employs the distinct features of the damping matrix to partition it based on blocks while the column-based strategy is still adopted on the kernel matrix. The partition process is illustrated by Figure 4.6. This scheme successfully reduced the overlap information on the sparse matrix, decreased total communication time, thus improving solver performance. More details can be searched in the related published paper [3]. It is necessary to point out that larger portion of sparse matrix in a coefficient matrix gives rise to better performance on solver improvement since the optimization is focused on damping matrix. Also, narrower width of the diagonal band yields smaller overlap between blocks and less communication cost.

To take full advantage of SP-LSQR, the structure of the proposed coefficient matrix was further examined. After several permutations, the coefficient matrix can be equivalent to the format listed by Figure 4.7. This structure exhibits a closely diagonal sparse matrix constructed by continuity equations, and a random entry based sparse matrix developed by observed data equations. Although there are both extremely sparse, according to their distinct features, the diagonal sub-matrix is viewed as a damping matrix, and the random entry based matrix is taken as a kernel matrix owing to its lack of noticeable

structure. Moreover, the damping matrix has narrow bandwidth which effectively limited the overlaps between blocks. The bandwidth will be increasingly relatively narrower with the increase of problem size, and thus, scaling performance will be better exhibited by high resolution problems. After this structure study, the developed scalable solver can effectively and efficiently resolve large problems.

The computation performance of SP-LSQR on our problem is listed by Figure 4.8. Unlike FP-LSQR, SP-LSQR yields the experimental timing plots much closer to the ideal situation which reveals the high stability performance of this solver on our problem. Now, a 500×500 problem was solved by only 150s CPU time. For a stochastic inversion based on 100×100 grid, a family of problems (100 realizations) can be solved in approximately less than 1 hours instead of 14 hours when the number of processors is 100.

SP-LSQR makes uncertainty analysis feasible. In general, uncertainty analysis requires a number of experiments to construct data analysis and hundreds of inverse problems have to be solved. Undoubtedly, decent computation efficiency is a prerequisite for uncertainty analysis study. For large problems, high resolution renders this condition more inevitable. Now, the serial solver improvement and SP-LSQR break through this bottleneck, therefore, uncertainty analysis becomes readily conducted and will be discussed by Chapter 5.

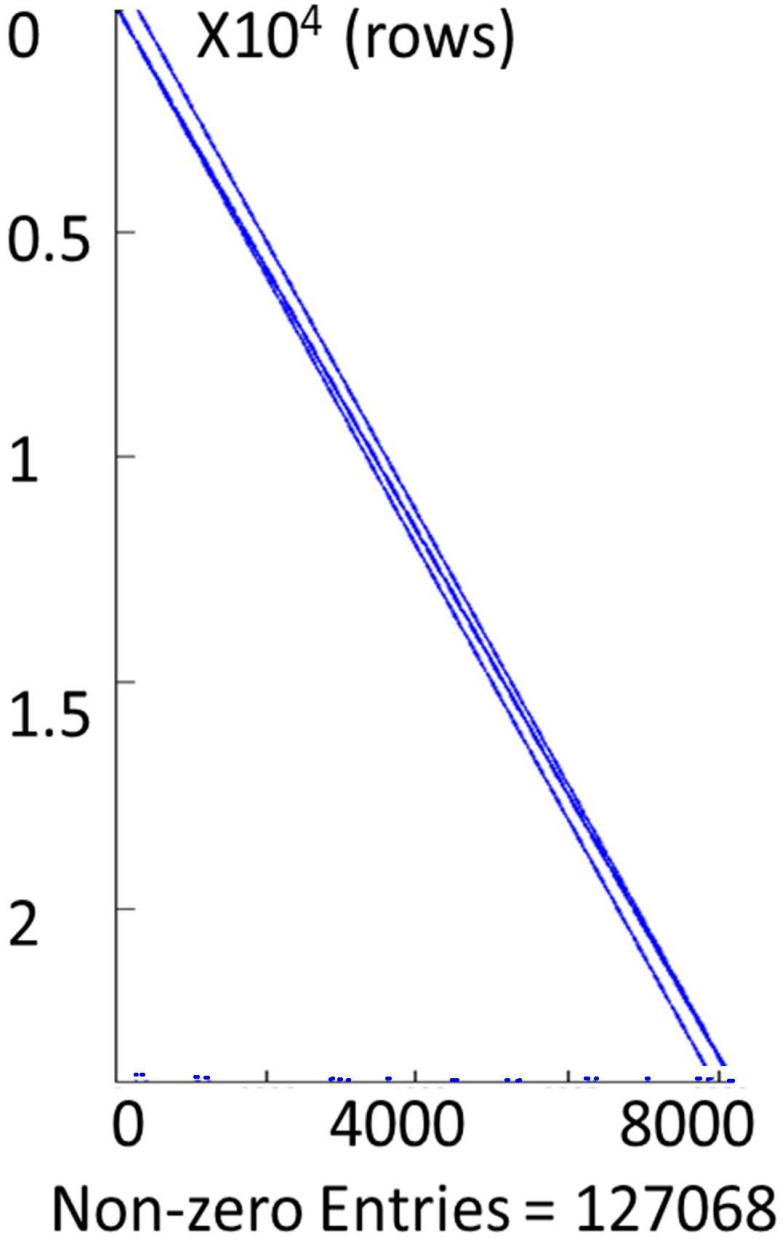

FIGURE 4.7: Spy matrix based on 32×32 problem. The diagonal lines and sparse dots describe the non-zero entries in the coefficient matrix. Other empty space represents zero entry region.

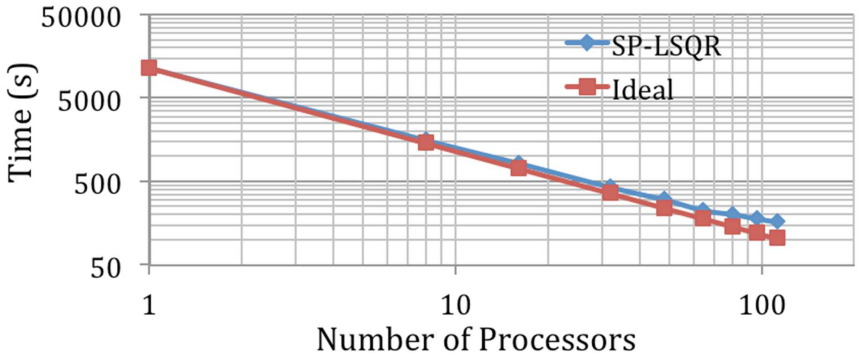

FIGURE 4.8: SP-LSQR time scaling. Time denotes computation cost based on CPU time. Number of processors shows how many processors are used to compute partitioned problems. The time plots of SP-LSQR are close to the ideal time scaling which indicates high scalability of the solver.

Chapter 5

Uncertainty Analysis

Uncertainty is inevitable to hydrogeological modeling and it arises from simulation uncertainty, data measurement, and representation strategy. A quality inverse model is obligated to limit uncertainty and ensure its robustness to data errors, so uncertainty quantification plays a prominent role in the examination on the quality of a model. This research conducted uncertainty analysis to understand the impacts of different factors on the quality of the inverse model. The tested factors include data quantity, data quality, and heterogeneity resolution. In addition, the co-effect from these factors is discussed, which helps understand their roles in inverse modeling better. Here, boundary conditions (BCs) and hydraulic conductivities (Ks) were chosen to assess model quality. Also, model precision and model accuracy were selected as the criteria to evaluate the outcome based on model perturbation.

5.1 Model Accuracy (MA) and Model Precision (MP)

Model calibration always requires proper criteria to rate model quality and hydrogeological modeling is not an exception. To examine a groundwater model, four criteria are commonly in use for model evaluation, including accuracy, precision, uncertainty and reliability[10]. Their definitions are listed below.

Model Accuracy (MA): the quality of being away from the correct value; higher accuracy exhibits the expectation of model outcomes closer to the true value.
Model Precision (MP): the quality of being concentrating on the correct value; higher precision yields a shorter uncertainty region.

Model Uncertainty (MU): the state of being uncertain which is reflected by uncertainty region.
Model Reliability (MR): the state of being reliable which is determined by precision and accuracy; higher reliability implies higher precision and higher accuracy.

Since model accuracy and model precision determine model uncertainty and model reliability, our uncertainty study is focused on model accuracy and model precision instead of four criteria to examine model quality. In terms of examination criteria, BC and K were selected to evaluate model quality in that BC determines the flow pattern which concerns hydrologists, and K is a model calibration criterion which affects modeling results.

5.2 Uncertainty Analysis on Single Factor

This section aims to conduct uncertainty analysis and examine the roles of different factors in inverse modeling from quantitative perspective. Generally speaking, uncertainty analysis examines the outcomes generated by perturbed inputs. Owing to the perturbation on inputs, the model outputs will behave differently and reveal the importance of each factor for an inverse model. This research investigated the impact of data quantity, data quality, heterogeneity resolution on the accuracy and precision of the inverse model, and thus, different perturbation strategies were laid out to design three parallel experiments.

5.2.1 Effects of Data Quantity

In real world, sampled data are always far from sufficient to hydrogeological modeling. Groundwater inverse modeling demands for a number of observed data to calibrate a model, which is hardly reachable since drilling wells is extremely expensive and data sampling requires much labor. Lack of observed data necessitates the uncertainty analysis on data quantity.

5.2.1.1 Experimental Conditions

A parallel experiment was established to examine the role of data quantity played in inverse modeling. Under the condition of same resolution hydrofacies K field and error-free observed data, three different drilling strategies, including 12 wells , 6 wells, and

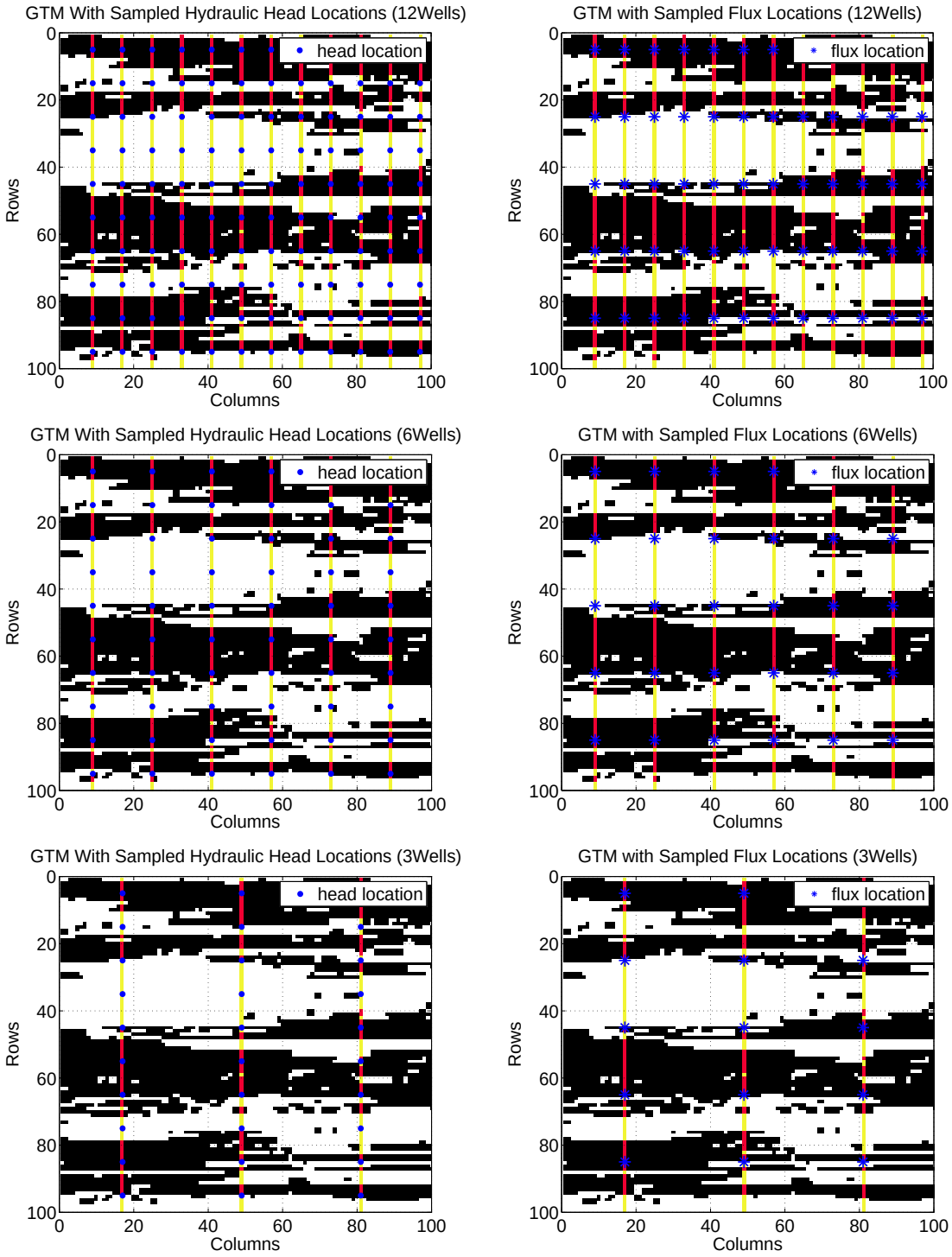

FIGURE 5.1: Data sampling strategies based on 12 wells, 6 wells, and 3 wells. The parallel straight lines denote the drilling wells and dots are sampling locations. Sampled heads are denser than fluxes.

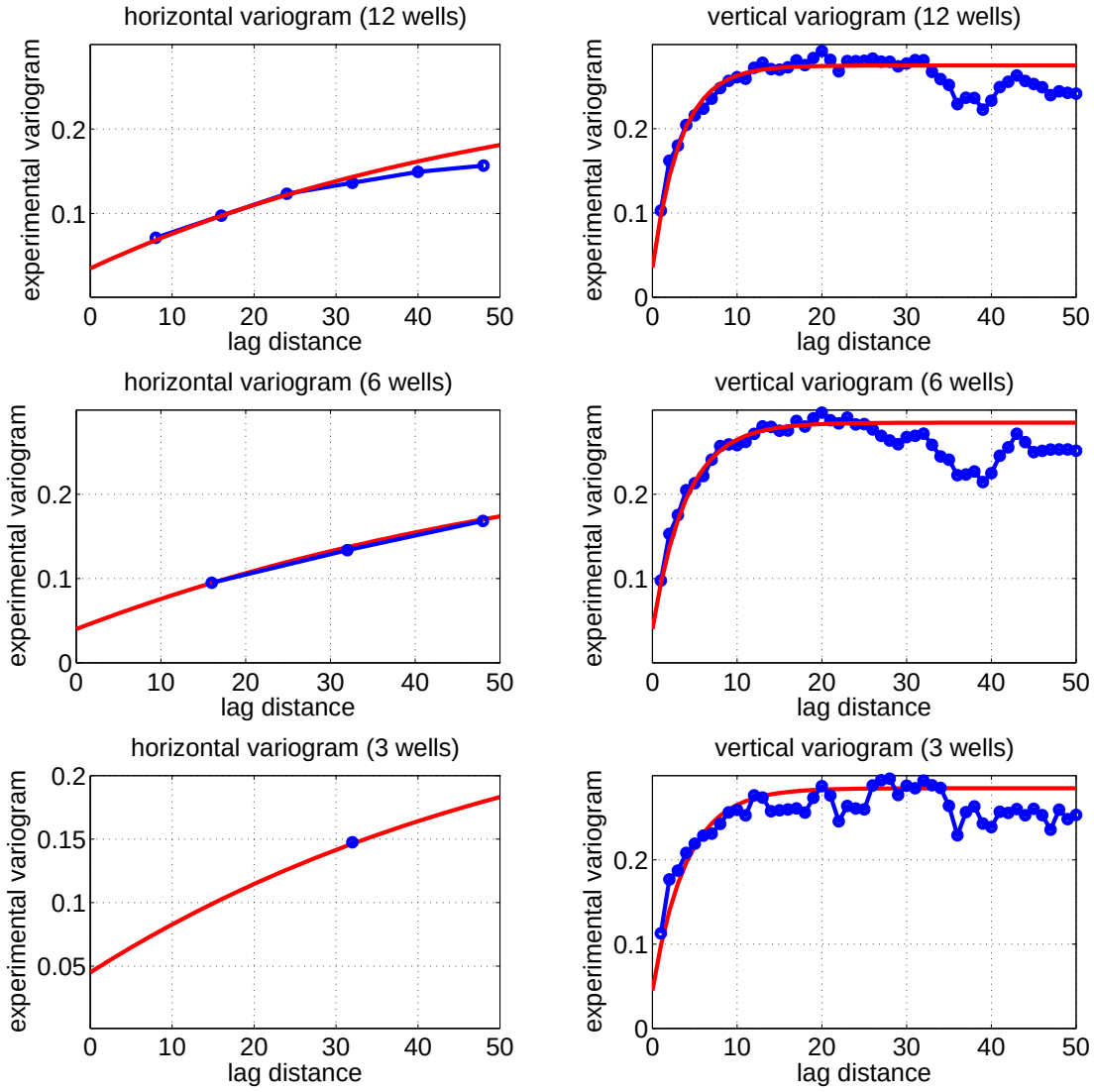

FIGURE 5.2: Variogram model based on 12 wells, 6 wells, and 3 wells. Scatter plots are experimental variogram values and the fitting curve is generated from fitting exponential varigram models.

3 wells (Figure 5.11), were conducted to sample observed data. According to different sampling fields, three observed data sets were constructed and undoubtedly, the total number of each category of data decreases with sampling well reduction when sampling density is same at each well. As regards hydraulic heads and fluxes, both of their data sets were shrunk as well as correspondent observed data equations were reduce, thus model calibration quality would be affected and model outcomes would be affected. Accordingly, a parallel experiment was established to direct the uncertainty analysis on data quantity via physically based stochastic inversions.

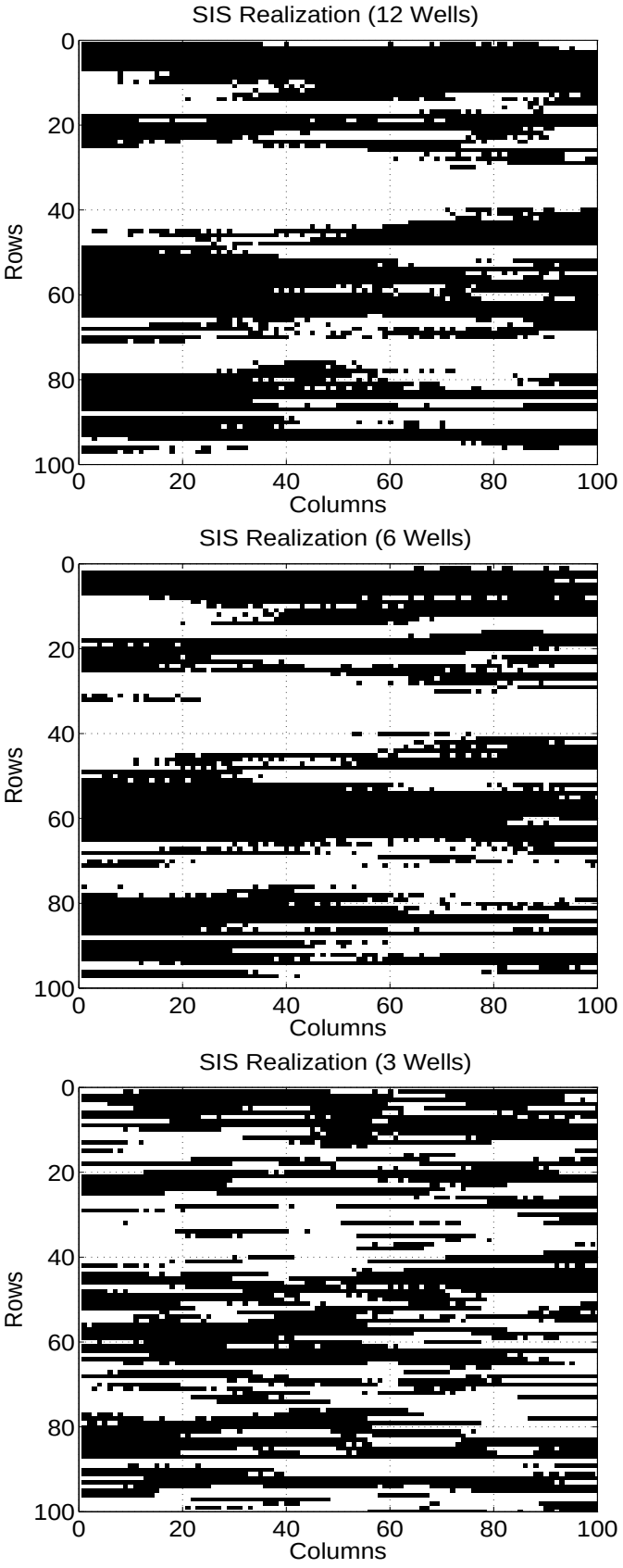

FIGURE 5.3: SIS realizations based on 12 wells, 6 wells, and 3 wells. One of each 100 realization based family is listed here. Column-row based coordinates are adopted.

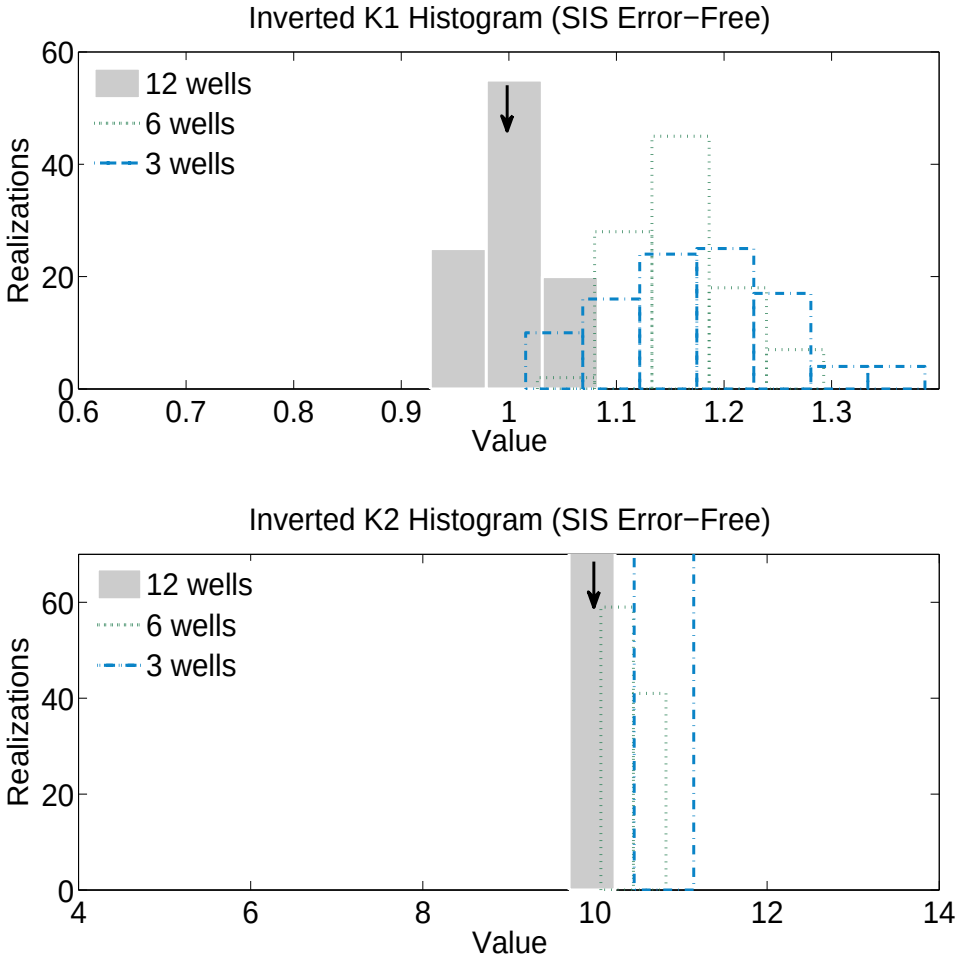

FIGURE 5.4: Ks uncertainty analysis based on data quantity. The arrows point to the true values. The realizations denote the frequency within different value range.

5.2.1.2 K, MA and MP

According to different wells, inverted Ks are obtained and visualized by Figure 5.4. When the number of sampling wells is 12, the center line of the inverted K_1 distribution is located at 1.025 and its uncertainty range is ± 0.08; when the number of sampling wells is 6, the center line is moved to 1.15 and the uncertainty range becomes ± 0.13; when the number of sampling wells is 3, the inverted K_1 distribution is centered at 1.2 with the uncertainty range of ± 0.2.

For inverted K_2s, when the number of sampling wells is 12, the center line is located at 10.1 and its uncertainty range is ± 0.8; when the number of sampling wells is 6, the center line is moved to 10.4 and the uncertainty range becomes ± 0.75; when the number

of sampling wells is 3, the resultant distribution is centered at 10.7 with the uncertainty range of ±0.6.

For K_1, within the ±3% uncertainty region, more than 50% inverted results are distributed when 12 wells are sampled; approximately 45% results are distributed when the inversion is conducted using 6 sampling wells; less than 30% results are distributed when the well number is reduced to 3. For K_2, within the ±3% uncertainty region, more than 80% inverted results are distributed when 12 wells are sampled; approximately 70% results are distributed when the inversion is completed using 6 wells; more than 70% results are distributed when the well number is reduced to 3.

Generally, inverted Ks are sensitive to data quantity; in particular, K_1 is more sensitive than K_2 to data quantity. With respect to MP, basically, the uncertainty region of each inverted K becomes wider with the decrease of drilling wells, which indicates MP becomes lower when data quantity decreases. Taking K_1 for example, its uncertainty range becomes twice when drilling wells are reduced by half. Concerning MA, the center lines of the inverted Ks are both oscillated around the true values when the quantity of drilling wells changes. The result implies the decrease of data quantity does not necessarily result in poorer K accuracy and it is possible to obtain decent inverted Ks using fewer data.

5.2.1.3 BC, MA, and MP

Inverted BCs based on different sampling wells are listed by Figure 5.5. Since the studied aquifer domain has been indexed, to well organize the discussion on model outcomes, the assessed boundary are decomposed into four sections ($\boldsymbol{a}-\boldsymbol{b}$, $\boldsymbol{b}-\boldsymbol{c}$, $\boldsymbol{c}-\boldsymbol{d}$, $\boldsymbol{d}-\boldsymbol{a}$) which are respectively described as follows:

$\boldsymbol{a}-\boldsymbol{b}$: For MP, the uncertainty ranges are basically kept to 20 feet and little influenced by the change of data quantity. In respect of MA, for 12 wells, 6 wells, and 3 wells, the center line of inverted BCs crosses the region between 290 feet and 300 feet, between 290 feet and 295 feet, and between 290 feet and 291 feet, respectively.

$\boldsymbol{b}-\boldsymbol{c}$: Regarding MP, the uncertainty region is shorter than 10 feet and its width increases, i.e., 3 feet, 6 feet, and 12 feet, with the decrease of sampling wells. In terms of MA, all resultant distributions are basically centered against the true BCs.

$\boldsymbol{c}-\boldsymbol{d}$: MP exhibits that the maximum of the width of the uncertainty region increases, i.e., 5 feet, 10 feet, and 20 feet, when the sampling wells decrease. For MA, the inverted

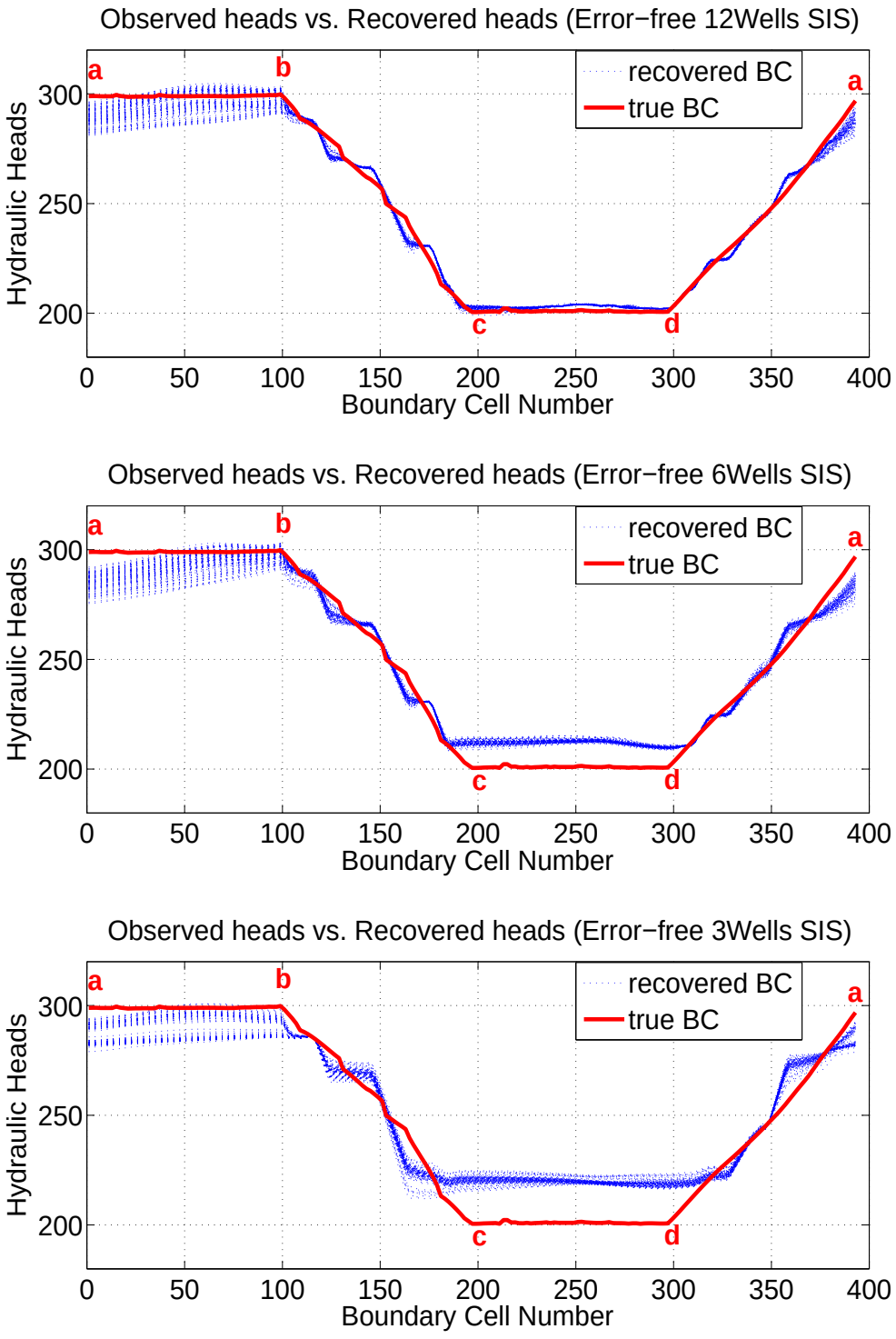

FIGURE 5.5: BCs uncertainty analysis based on data quantity. Here are three experiments based on different numbers of sampling wells. At each sampling well, the sampling density is same. The letters of alphabet denote the boundary locations. Hydraulic heads are recovered conditions and boundary cell number is the index of each boundary cell.

BCs are basically centered at 202 feet, 210 feet, and 220 feet for 12 wells, 6 wells, and 3 wells, which implies that the resultant BCs are increasingly biased towards the true conditions when drilling wells decrease.

$\boldsymbol{d-a}$: Regarding MP, the uncertainty region increases, i.e., 1.5 feet, 3 feet, and 6 feet, with the decrease of drilling wells. For MA, the center lines are all basically against the true conditions.

Generally, inverted BCs are sensitive to data quantity. When sampled wells are decreased by half, the uncertainty region will been basically twice widen. With respect to MP, the uncertainty region becomes wider with the decrease of sampling wells, which indicates MP becomes lower when data quantity decreases. As regards MA, the center line is increasingly away from the true BCs when data quantity is reduced, which indicates the decrease of data quantity will worsen MA. In particular, the section $\boldsymbol{c-d}$ is most sensitive to data quantity; the section $\boldsymbol{a-b}$ exhibits largest uncertainty regions constantly; both $\boldsymbol{b-c}$ and $\boldsymbol{d-a}$ show the increase of uncertainty region when data sets are shrunk despite the center lines against the true BCs.

5.2.1.4 Discussion on Data Quantity Strategy

In terms of data quantity, we were informed of some knowledge and sampling strategies by the inverted results above, especially inverted K_1s. For MP, the experiment using 6 wells exhibits half lower precision than 12 wells; 3 wells shows 1.5 times lower precision than 6 wells. Also, 6 wells are capable of generating decent model outcomes with good precision and acceptable accuracy with relatively fewer observed data.

5.2.2 Effects of Data Quality

Another parallel experiment was directed to investigate the impact of data errors on the inverse model. In real world, measurement errors are inevitable due to unpredictable physical conditions and limited equipment precision. Hence, it is vital to understand the relation between data errors and inverse model outcomes. If a model outcome is relatively instable when a certain data error is involved, this model is usually reckoned among weak applicability to practical problems. Therefore, in general, hydrogeology modelers expect proposed models can be robust to data errors, thus ensuring its ability to solve real problems. To achieve the similar goal, this research also conducted the

experiment based on data corruption and understand the robustness of our proposed inverse model to measurement errors.

5.2.2.1 Experimental Conditions

The parallel experiment was designed based on observed hydraulic heads corrupted by white noise. White noise based data corruption is widely in use to detect the model robustness to data error [49]. The primary idea of the approach is to generate a group of noise following a normal distribution centered at 0. The uncertainty region of the distribution is determined by the magnitude of the noise. From statistical knowledge, this uncertainty range refers to the standard deviation (SD) of the noise in terms of a normal distribution. Hence, modelers commonly set different SDs instead of uncertainty ranges to describe noise magnitudes. Here, observed hydraulic heads were corrupted by the white noise with increasing standard deviation (SD), i.e., error-free, ±1%, ±2%, ±5%, and ±10%. All of these corruptions are derived from total head variation (THV). Using different observed data sets, four sets of physically based stochastic inversions were directed and inverted results were discussed.

5.2.2.2 K, Model Precision, and Model Accuracy

According to different SDs of the white noise based on THV, inverted Ks are listed by Figure 5.6. For inverted K_1, when the observed heads are corrupted by the noise with ±1% magnitude, the center line of the resultant distribution is located at 0.97 and its uncertainty range is ±0.085% of the true value; when the data are corrupted by the noise with ±2% magnitude, the inverted K_1 distribution is centered at 0.93 within the uncertainty region of ±0.095% of the true value; when the observed heads are corrupted by the noise with ±5% magnitude, the center of the resultant distribution is moved to 0.71 and the uncertainty range is slightly increased to ±0.13% of the true value; when the observed heads are further corrupted by the noise with ±10% magnitude, the inverted results are centered at 0.24 and distributed within the uncertainty region of ±0.195% of the true value.

Concerning inverted K_2, when the observed heads were corrupted by the noise with ±1% magnitude, the inverted results are centered at 9.87 and the uncertainty range is ±0.29% of the true value; when the data corruption magnitude is increased to ±2%, the center line of the inverted K_2 distribution is located at 9.71 and its uncertainty range

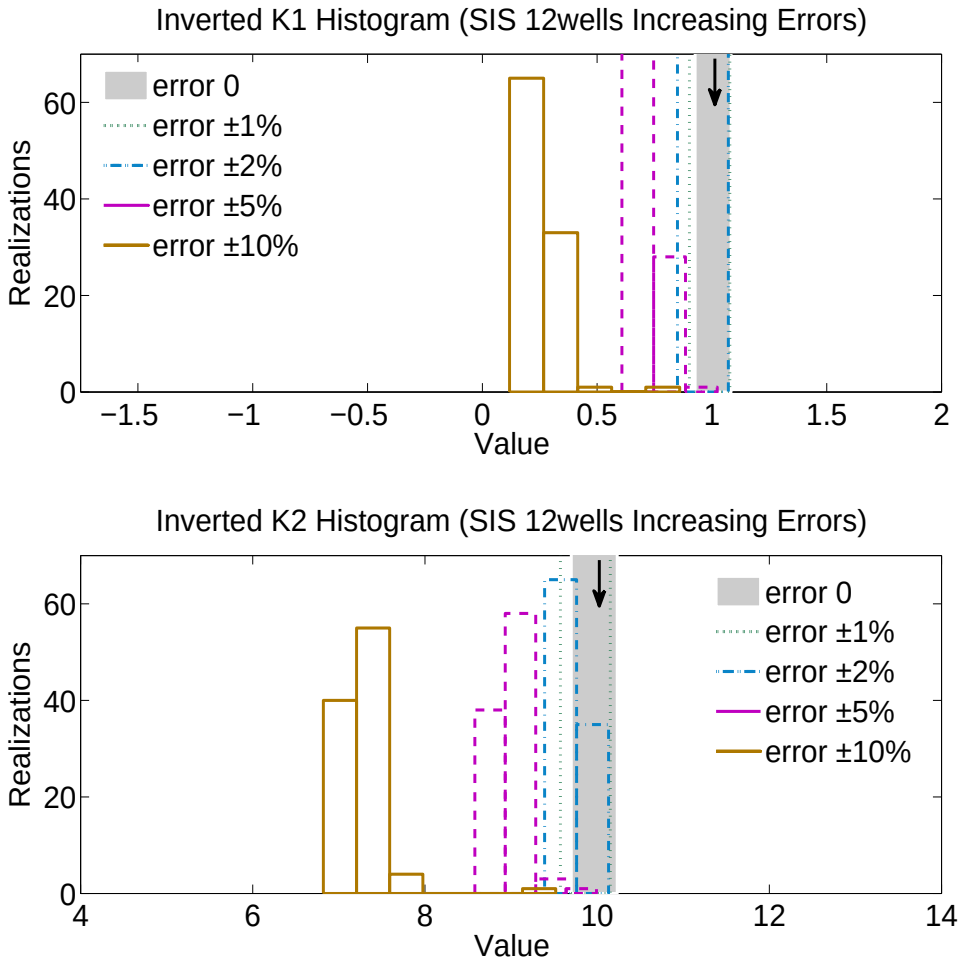

FIGURE 5.6: Ks uncertainty analysis based on data quality.The arrows point to the true values. The realizations denote the frequency within different value range.

is slightly increased to ±0.305%; when the corruption magnitude is increased to ±5%, the center of the resultant distribution is moved to 8.97 and the uncertainty range is slightly widen to ±0.445%; when the observed data are further corrupted by the noise with ±10% magnitude, the inverted results are centered at 7.26 and distributed with the uncertainty region of ±0.49% of the true value.

According to the inverted Ks above, for K_1, within the uncertainty region of ±3% of the true value, more than 70% inverted results are distributed when sampled data are corrupted by the errors based on ±1% of THV; approximately 70% results lie when the data errors are increased to ±2% of THV; approximately 60% results are spread when data errors are increased to ±5% of THV; less than 60% results are distributed when data corruption magnitude is increased to ±10% of THV.

For K_2, within the uncertainty region of ±3% of the true value, more than 70% inverted results are distributed when sampled hydraulic heads are corrupted by the errors based on ±1% of THV; approximately 60% results lie when the data errors are increased to ±2% of THV; less than 60% results are spread when data errors are further increased to ±5% of THV; less than 60% results are distributed when data corruption magnitude is increased to ±10% of THV.

In general, inverted Ks are sensitive to data errors; in particular, K_1 is more sensitive than K_2 to data quality. With respect to MP, the uncertainty region becomes wider with the SD increase of data errors, which indicates MP becomes lower when data quality is worse. Specifically, when the corruption magnitude is more than ±5% of THV, the deterioration of MP is more rapid. As regards MA, the center line is increasingly away from the true value when the data error SD becomes larger, which implies that the deterioration of data quality causes poorer K accuracy. Since the deterioration trend is stable, it is possible to predict MA status from observed model behaviors.

5.2.2.3 BC, MA and MP

The inverted BCs from the data with different corruption magnitudes are listed by Figure 5.7. The related discussion is still organized based on sections as follows:

$\boldsymbol{a-b}$: For MP, the maximum of the uncertainty range is basically kept to 20 feet when the corruption magnitude is within ±5% of THV. When the corruption magnitude is increased to ±10% of THV, the uncertainty range is dramatically increased to 35 feet. In terms of MA, the center line of inverted BCs lies within the region between 290 feet and 300 feet when the corruption magnitude is not more than ±5% of THV; the center line is closer to 300 feet when the data corruption magnitude is increased to ±10% of THV.

$\boldsymbol{b-c}$: With respect to MP, it exhibits the similar features to the section $\boldsymbol{a-b}$. The width of the uncertainty region is relatively steady and kept to 20 feet when data corruption magnitude is smaller than ±5% of THV. When the magnitude is increased to ±10% of THV, the width of the uncertainty region is widen to 36 feet. Concerning MA, $\boldsymbol{b-c}$ shows a more decent model behavior than the section $\boldsymbol{a-b}$. The inverted BCs are basically against the true conditions and the bias is not more than 2.5 feet. Meanwhile, it is necessary to point out that the inverted BC center line yields increasing underestimation on the true conditions even if the magnitude of the change is not large.

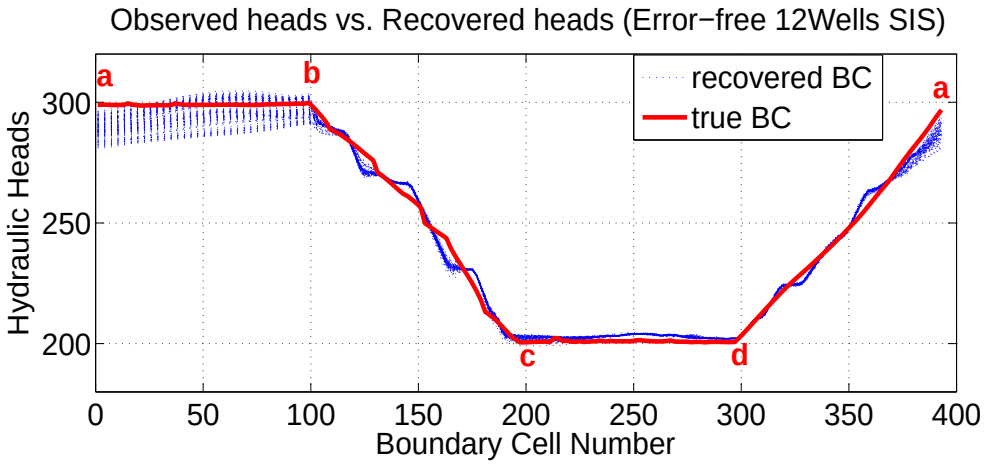
Observed heads vs. Recovered heads (Error−free 12Wells SIS)
recovered BC
true BC
a
b
c
d
a
Hydraulic Heads
300
250
200
0
50
100
150
200
250
300
350
400
Boundary Cell Number

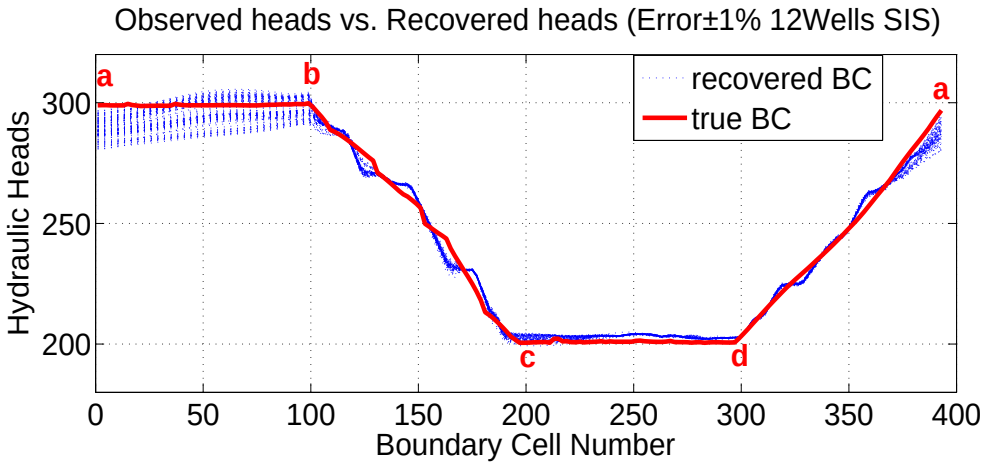
Observed heads vs. Recovered heads (Error±1% 12Wells SIS)
recovered BC
true BC
a
b
c
d
a
Hydraulic Heads
300
250
200
0
50
100
150
200
250
300
350
400
Boundary Cell Number

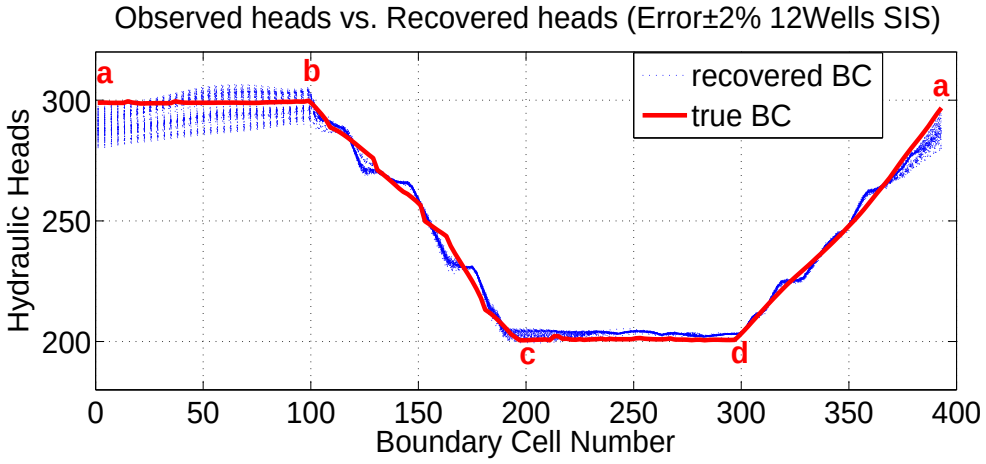
Observed heads vs. Recovered heads (Error±2% 12Wells SIS)
recovered BC
true BC
a
b
c
d
a
Hydraulic Heads
300
250
200
0
50
100
150
200
250
300
350
400
Boundary Cell Number

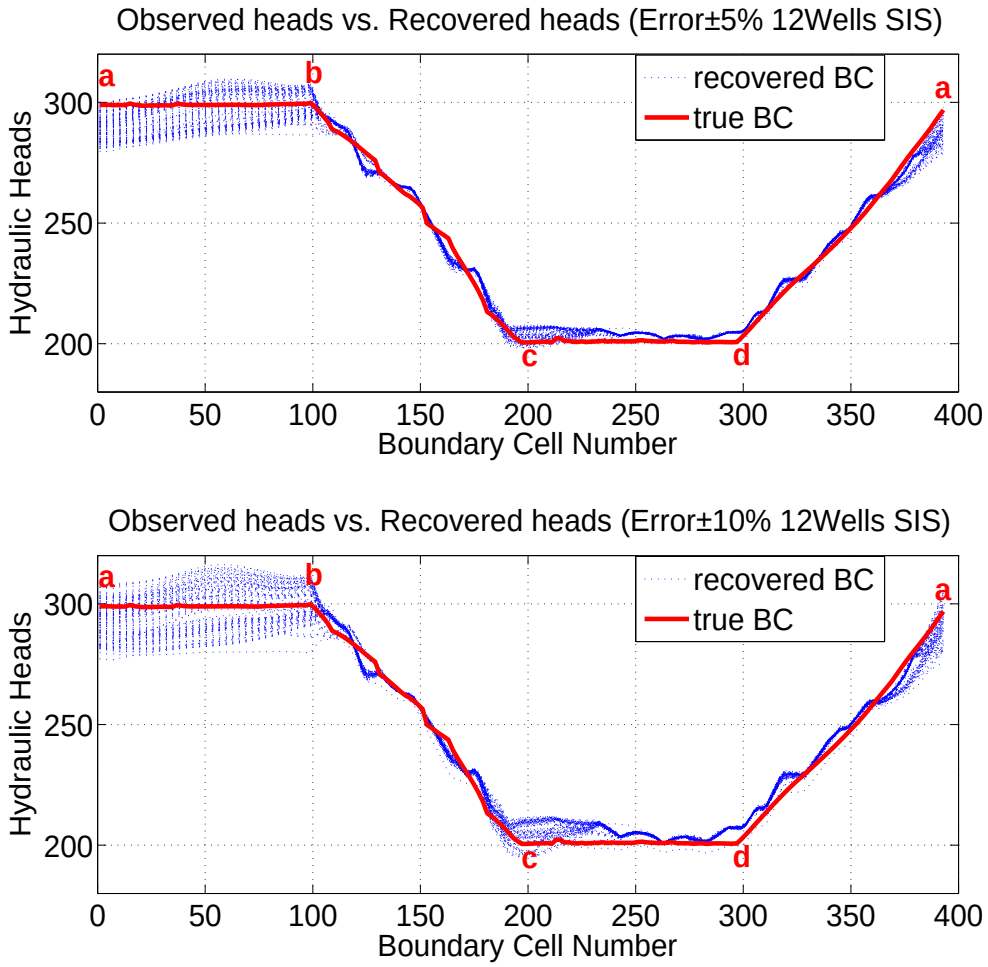

FIGURE 5.7: BCs uncertainty analysis based on data quality. The letters of alphabet denote the boundary locations. Hydraulic heads are recovered conditions and boundary cell number is the index of each boundary cell.

$\boldsymbol{c-d}$: For MP, with the increase of data corruption, the maximum of the width of the uncertainty region increases, i.e., 10 feet for $\pm 1\%$, 12 feet for $\pm 2\%$, 16 feet for $\pm 5\%$, and 25 feet for $\pm 10\%$. MA exhibits higher stability and the bias less than 1 foot, which implies the good robustness to data errors.

$\boldsymbol{d-a}$: In respect of MP, the highest stability is reflect by the narrowest uncertainty region and the mildest change in its width. The width of the uncertainty region is less than 10 feet and its change is kept to less than 2 feet when the corruption magnitude is less than $\pm 5\%$ of THV. For MA, the underestimation is better exhibited while the maximum of the center line bias is kept to less than 0.5 foot for the corruption less than $\pm 5\%$ of THV, which also reveals the good robustness to data errors.

According to the inverted BC results, the section $\boldsymbol{a-b}$ is most sensitive to the change

of data quality. The section $\boldsymbol{b}-\boldsymbol{c}$ yields the similar uncertainty region increase to the section $\boldsymbol{a}-\boldsymbol{b}$ with increased data errors; however, its MA behavior is much better than the section $\boldsymbol{a}-\boldsymbol{b}$. The section $\boldsymbol{c}-\boldsymbol{d}$ has a best MA behavior reflected by the minimum of the bias and the mildest change. The section $\boldsymbol{d}-\boldsymbol{a}$ shows best MP performance because of the narrowest uncertainty region.

Generally, inverted BCs are not sensitive to data quality of observed hydraulic heads. With respect to MP, the uncertainty region becomes a little wider and MP becomes lower when data quality is mildly deteriorated, such as less than $\pm 5\%$ of THV. As regards MA, the inverted BCs are increasingly biased generally as well as exhibits aggravated underestimation; the deterioration is mild, though. In sum, the model is robust to data errors and the increase of data errors will only mildly worsen MP and MA in terms of recovered BCs.

5.2.2.4 Discussion on Data Quality Strategy

Considering the analysis above, some sampling strategies on data quality are revealed to help conduct inverse modeling more efficiently. When 12 wells are sampled and heterogeneity resolution is a SIS based grid, MP based on $\pm 5\%$ corruption magnitude is as less than twice low as $\pm 1\%$ corruption magnitude; the precision from $\pm 10\%$ corruption magnitude is as more than twice low as $\pm 5\%$ corruption magnitude. Hence, $\pm 5\%$ should be largest magnitude for data corruption if it is hoped that the impact of data corruption is controlled to closely linear influence.

5.2.3 Effects of Heterogeneity Resolution

This section will explore the role of heterogeneity resolution (HR) in inverse model with another a parallel experiment. Hydrogeological model commonly yields high HR, thus resulting in high time cost. However, such high resolution is not indispensable to understand the general features of an aquifer sometimes. Accordingly, some compromise strategies between HR and computation efficiency are explored to trade lower resolution for faster computation. Thus, HR is also an important factor worth examining by uncertainty analysis.

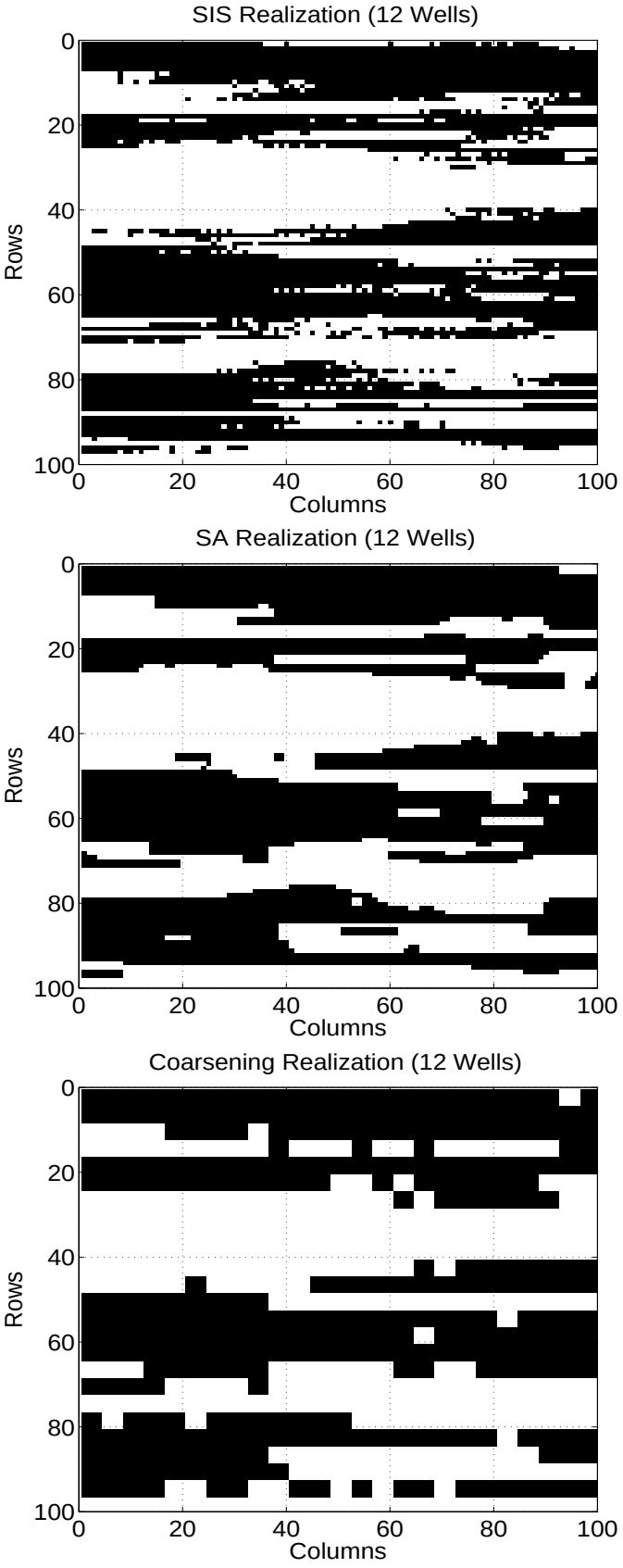

FIGURE 5.8: Realizations based on SIS grid, SA grid, and Coarsening grid. One of each 100 realization based family is listed here. Column-row based coordinates are adopted.

5.2.3.1 Experimental Conditions

A parallel experiment was also constructed based on three different resolution grids to investigate how HR influences the inverse model. Usually, model outcomes by SIS exhibit high resolution and undoubtedly precise heterogeneity patterns while some noise generated in stochastic process will render modeling involve a great deal of computation time. The time consuming performance limits the grid refinement on large problems. To address this issue, some Geostatistics modelers implemented and developed Simulated Annealing (SA) algorithm to remedy these SIS realizations and generated noises will be cleaned. However, the SA operation will somewhat modify the shape of simulated hydrofacies and induce some bias depending on annealing schemes. Sometimes, to trade for much higher computation efficiency, coarsening strategy is employed to approximate the SIS grid, which refers to upscaling research topic. Undoubtedly, more bias will be induced by the similar approach even if coarsening scheme is clever. To understand how much bias is induced by each modification on grid, this research designed three different sets of grids, including SIS grids, SA grids and Coarsening grids, as hydrofacies K fields. All of the grids were inverted based on 100×100 grid and only heterogeneity details are different: SIS grid exhibits most details, SA grid is smoother, and Coarsening grid possesses lowest details on interfaces. Regarding dynamic data, hydraulic heads and fluxes were still sampled from the original synthetic aquifer, and thus, all data sets were same for different grids. Using the same hydraulic head and flux data sets, three sets of physically based stochastic inversions based on different resolution grids were directed and inverted results were discussed.

5.2.3.2 K, MA, and MP

According to different resolutions, inverted Ks are listed by Figure 5.9. When an SIS grid is selected as inverse resolution, the center line of the inverted K_1s is located at 1.00 and its uncertainty range is ± 0.075; when the resolution is reduced to SA grid, the center line is slightly moved to 1.03 and the uncertainty range is widen to ± 0.12; when lowest resolution, i.e., coarsening grid, is chosen, the inverted K_1s are centered at 0.94 and distributed within the uncertainty region of ± 0.15.

With respect to K_2, when the SIS grid is selected as inverse resolution, the center line of the inverted K_2s is located at 9.97 and its uncertainty range is ± 0.23; when the resolution is reduced to SA grid, the center line is moved to 9.8 and the uncertainty

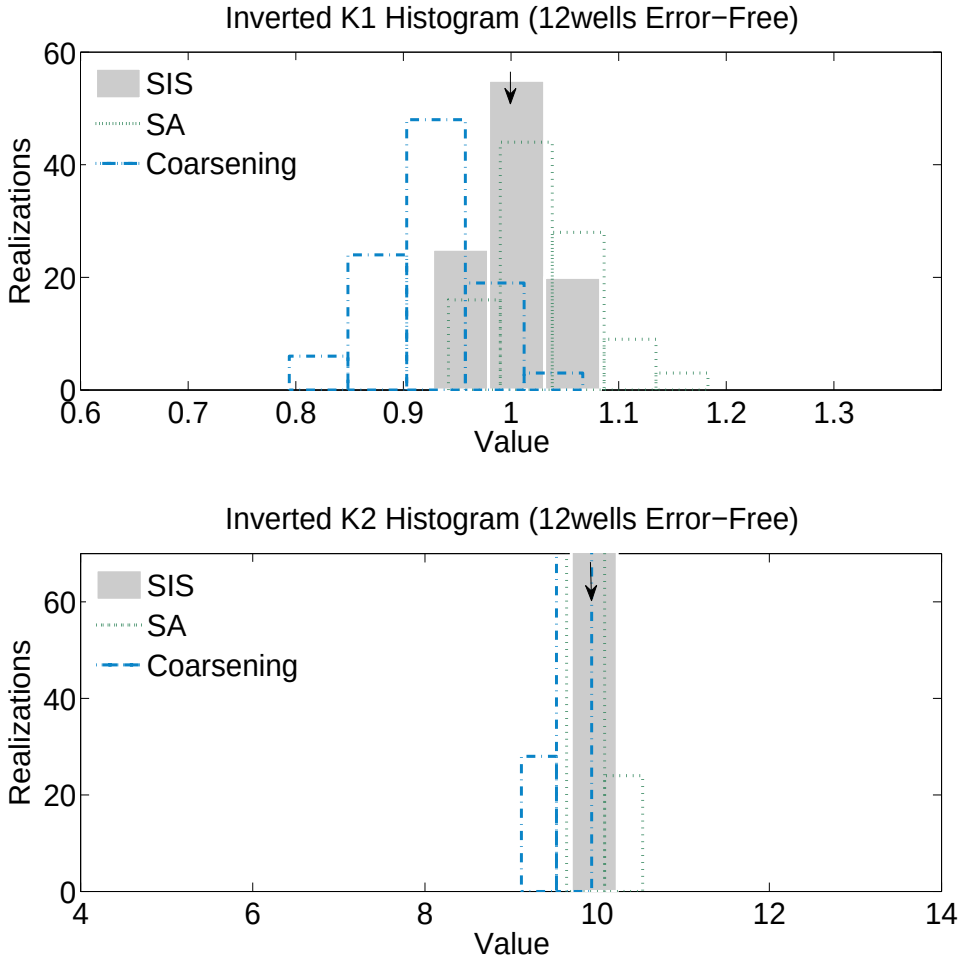

FIGURE 5.9: Ks uncertainty analysis based on heterogeneity resolution.The arrows point to the true values. The realizations denote the frequency within different value range.

range is increased to ± 0.33; when lowest resolution, i.e., coarsening grid, is chosen, the inverted K_2s are centered at 9.5 and distributed within the uncertainty region of ± 0.42.

In general, inverted Ks are insensitive to resolution change from the results of this experiment while K_1 is relatively more sensitive than K_2 to grid resolution. Concerning MP, the uncertainty region becomes wider with lower grid resolution, which indicates MP becomes lower with smoother grids. Compared to MP, MA exhibits more noticeable change when resolution information is reduced. With less resolution information, the center of the resultant distribution is increasingly deviated from the true value. All of the facts imply that grid smoothing causes poorer K accuracy but model deterioration is not severe.

5.2.3.3 BC, MA, and MP

According to different grid resolutions, inverted BCs are listed by Figure 5.10. Similar to pervious two experiments, the discussion on BCs is organized based on sections as follows:

$\boldsymbol{a-b}$: For MP, the maximum of the uncertainty range changes with different grids are chosen, i.e., 18.0 feet for SIS grids, 19.2 feet for SA grids, and 9.7 feet for Coarsening grids. Coarsening operation exhibits noticeable improvement on MP. In terms of MA, the bias of the center line from the true conditions is 6.5 feet, 4.9 feet, and 10.2 feet for SIS grids, SA grids, and Coarsening grids, respectively. From the Figure 5.10, he region where is closer to point a exhibits more noticeable deviation from the true conditions.

$\boldsymbol{b-c}$: For MP, the widths of the uncertainty regions show 18.2 feet for SIS grids, 19.5 feet for SA grids, and 9.5 feet for Coarsening grids, which are similar to the results from the section $\boldsymbol{a-b}$. However, in respect of MA, the center line of the resultant distribution exhibits much less bias, i.e., 2.3 feet for SIS grids, 0.2 foot for SA grids, and 0.88 foot for Coarsening grids. The results imply that MA is robust to the change of HR on the section $\boldsymbol{b-c}$.

$\boldsymbol{c-d}$: With respect to MP, the width of the uncertainty region is 8.9 feet, 9.2 feet, and 5.7 feet for SIS grids, SA grids, and Coarsening grids, respectively. The resultant data indicate higher precision and better MP behavior. In addition, the MP alteration due to grid resolution change becomes milder on this section. For MA, relatively lower bias of the center line is shown, i.e., 0.7 foot for SIS grids, 0.3 foot for SA grids, and -1.2 foot for Coarsening grids. Here, good robustness to HR change is exhibited although aggravated underestimation is shown.

$\boldsymbol{d-a}$: For MP, the inverted BCs are distributed within the region with the width of 7.8 feet for SIS grids, 8.7 feet for SA grids, and 6.7 feet for Coarsening grids. Decent robustness to HR change is exhibited although Coarsening operation still improves MP slightly. In terms of MA, the center line is increasingly deviated from the true conditions and the biases are 0.1 foot for SIS grids, -0.5 foot for SA grids, and -1.9 feet for Coarsening grids. MA also behaves robustly even if the region closer to a shows relatively larger bias.

According to the description on the inverted BC results, the region close to a is most sensitive to the change of grid resolution; the region close to b also exhibits somewhat result improvement in uncertainty region with lower resolution; for other sections, the

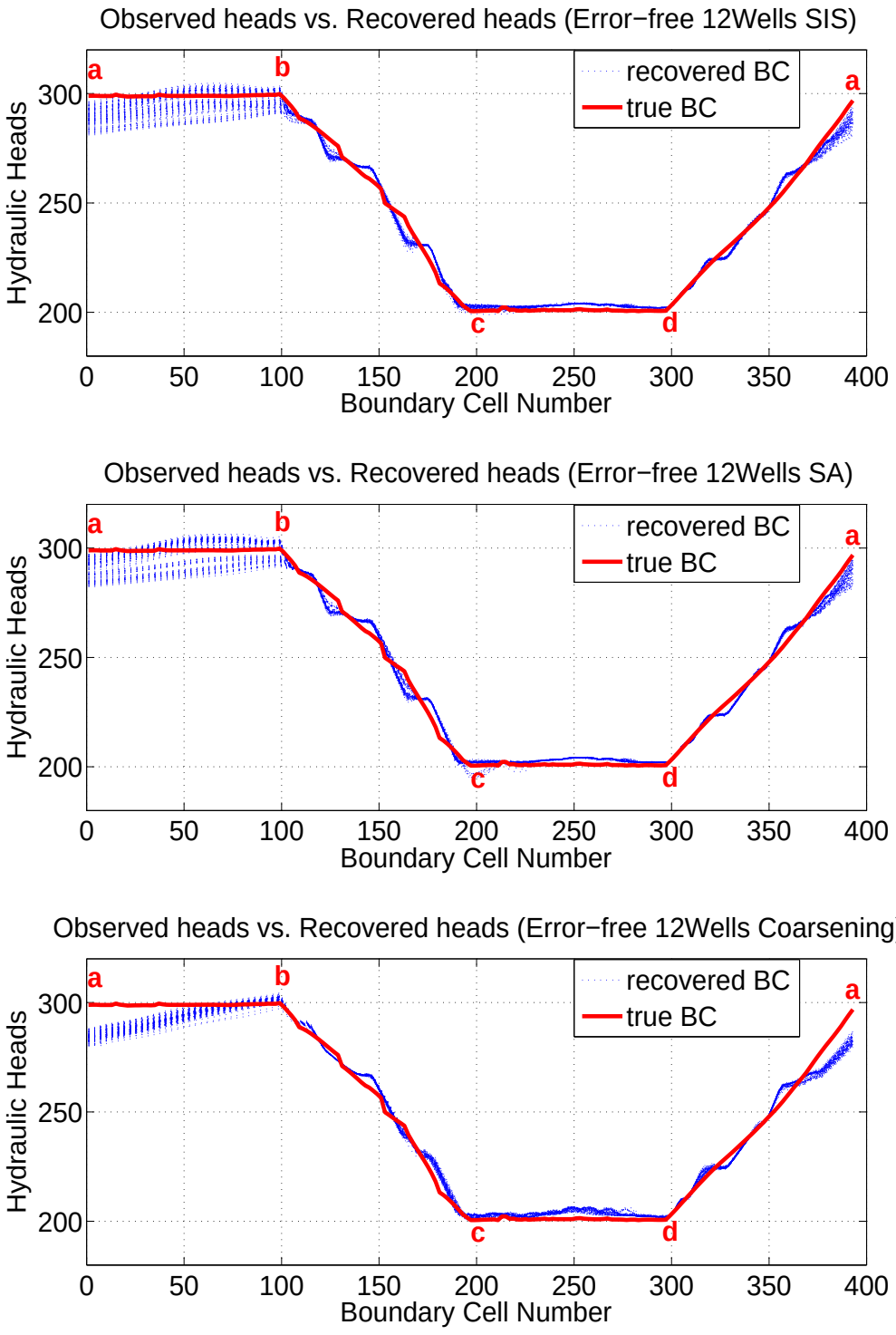

FIGURE 5.10: BCs uncertainty analysis based on heterogeneity resolution. Here are three experiments using different grid resolution including SIS grid, SA grid, and Coarsening grid. The grid size is 100×100 all the time. The letters of alphabet denote the boundary locations. Hydraulic heads are recovered conditions and boundary cell number is the index of each boundary cell.

center line and uncertainty region show little difference when grid resolution is changed. Specifically, the sections of $\boldsymbol{c}-\boldsymbol{d}$ and $\boldsymbol{d}-\boldsymbol{a}$ have robust MP and MA behavior to HR change.

Generally, inverted BCs are not sensitive to grid resolution of hydrofacies K fields. With respect to MP, the uncertainty region is always narrowest when Coarsening grids are inverted, which indicates MP can be improved by grid resolution reduction. As regards MA, the center line of inverted BCs is increasingly away from the true conditions when chosen grids possess lower resolution and the distance changes relatively much. It implies that lower grid resolution can worsen the accuracy of recovered BCs while the precision is improved, so resolution reduction has less influence on model reliability owing to accuracy-precision balance.

5.2.3.4 Discussion on Heterogeneity Resolution Strategy

We are informed of some grid representation strategies by the inverted results, especially inverted K_1 and inverted BCs along the region close to a. Lower resolution can improve the model precision while MA is affected by the bias carried with gird smoothing. However, the impact of the bias on inverse model is mild and acceptable under sufficient data support. Meanwhile, smoothed grids can perform high computation speed and render stochastic inversion more efficient. Therefore, model reliability is basically preserved when grid resolution is lower and upscaling is advisable to improve computation performance.

5.3 Co-effect of Different Factors

This section will try to briefly discuss co-effect of different factors, including data quantity, data quality, and heterogeneity resolution, on modeling outcomes and provide some primary results from the correspondent two-dimensional uncertainty experiments. In last section, uncertainty analysis results reveal the role of each factor in the inverse modeling. As a matter of fact, they are not independent and have co-effects on the inverse results. Any perturbation on two factors will yield different model outcomes revealing the different priority of each factor on inverse model. To understand the combined effect of multiple factors, design of experiment (DoE) is a common approach and widely in use to evaluate correlation between different factors and their impact levels on the model. For DoE, the number of factors is usually high and then, a complex

response surface (RS) will be generated using interpolation on experiment results. Here, our research is focused on only three factors, so a complex DoE will not be conducted and RS will not be described by interpolation. We just developed three two-dimensional experiments to detect the primary relation between different factors. Accordingly, another three groups of experiments are developed to investigate the significance rank of different factor via co-effect analysis results.

5.3.1 Data Quantity and Heterogeneity Resolution

5.3.1.1 Experiment Conditions

The first parallel experiment for co-effect research is to examine the co-effect of data quantity and heterogeneity resolution on the inverted Ks and BCs. The basic conditions of this experiment include decreased sampling wells, i.e., 12 wells, 6 wells, and 3 wells, and increasing lower resolution, i.e., SIS grid, SA grid, and Coarsening grid. For each well sampling strategy, three different heterogeneity resolutions are employed to conduct three sets of stochastic inversions. When well sampling strategy is set, the dynamic data are determined and not changed with heterogeneity resolution. All of these studies are directed on the premise of error-free observed data. Under these conditions, several experiments are conducted and experimental results are discussed as followed.

5.3.1.2 K, MA, MP

Each K exhibits different inverted distribution patterns under different experiment conditions. The inverted distributions are listed by Figure 5.12 and Figure 5.13. From these resultant data, some primary features of inverse model are detected based on inverted Ks.

First of all, the two-dimensional experimental design obtained some similar outcomes to each single factor experiment. For each data sampling strategy, lower resolution leads to lower accuracy and lower precision generally. Basically, fewer wells cause lower accuracy and lower precision under same resolution. Meanwhile, K_1 and K_2 yield similar changes in distribution patterns when different factors are perturbed. Still, K_2 exhibits milder change than K_1 when the conditions are perturbed. Therefore, the uncertainty research on Ks will adopt the inverted K_1 to explore the co-effect. The specific characteristics for each distribution patterns are quantified and tabulated by Table 5.1 and Table 5.2.

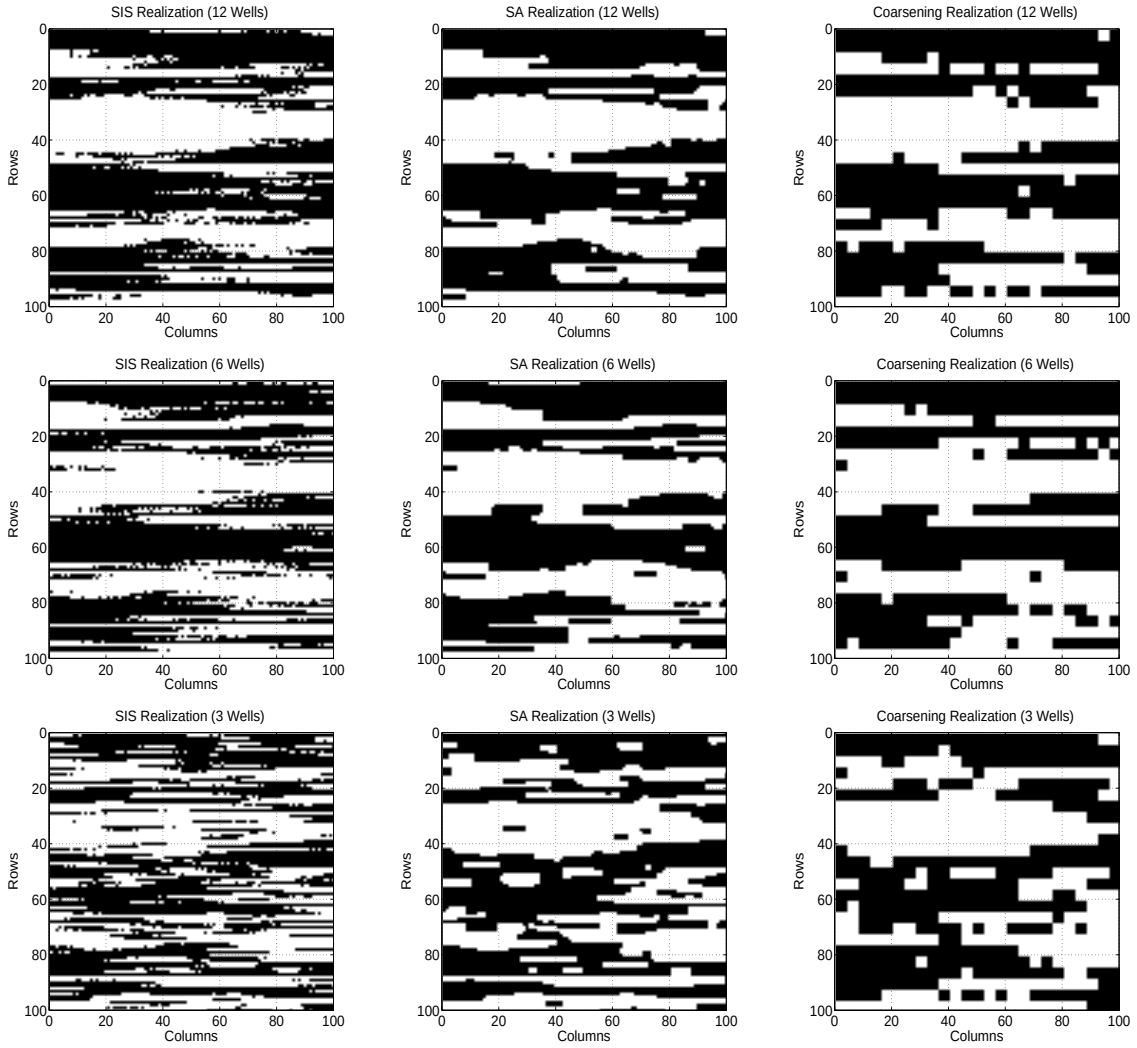

FIGURE 5.11: SIS, SA, Coarsening realizations based on 12 wells, 6 wells, and 3 wells. Each realization is one of 100 realizations based family. Column-row based coordinates are adopted.

TABLE 5.1: MA analysis from inverted K_1 based on two-dimensional experiment. Here, the two dimensions are data quantity (columns) and heterogeneity resolution (rows). HR denotes heterogeneity resolution and DQn denotes data quantity. Listed inverted Ks are the center values of resulting distributions.

HR \ DQn	12 wells	6 wells	3 wells
SIS	1	1.15	1.18
SA	1.03	1.27	0.94
Coarsening	0.94	0.97	1.34

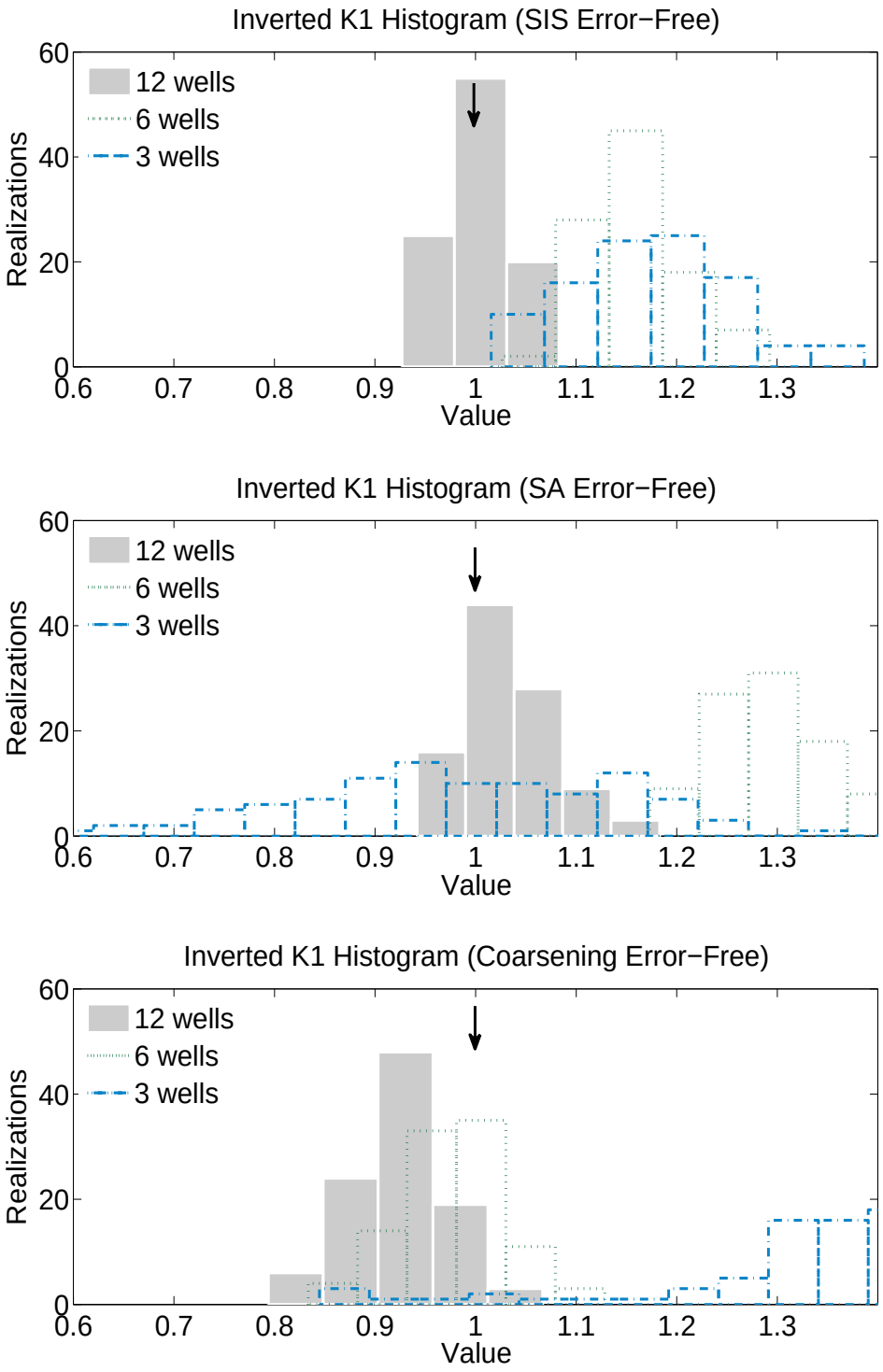

FIGURE 5.12: K_1 uncertainty analysis based on data quantity and heterogeneity resolution. The arrows point to the true values. The realizations denote the frequency within different value range.

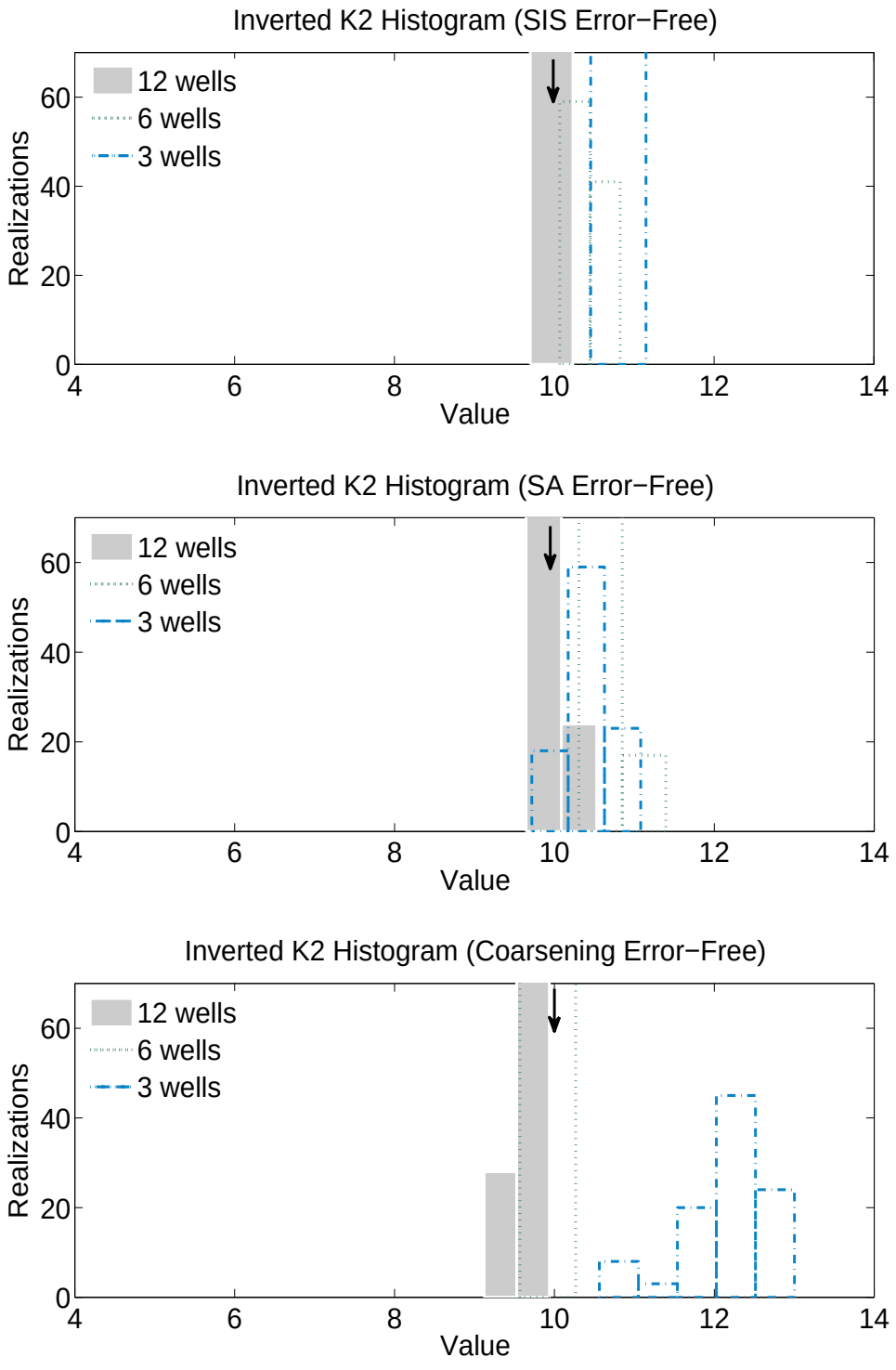

FIGURE 5.13: K_2 uncertainty analysis based on data quantity and heterogeneity resolution. The arrows point to the true values. The realizations denote the frequency within different value range.

TABLE 5.2: MP analysis from inverted K_1 based on two-dimensional experiment. Here, the two dimensions are data quantity (columns) and heterogeneity resolution (rows). HR denotes heterogeneity resolution and DQn denotes data quantity. Listed inverted Ks are the maximum deviations of resulting distributions.

HR \ DQn	12 wells	6 wells	3 wells
SIS	0.15	0.28	0.41
SA	0.23	0.35	0.84
Coarsening	0.30	0.32	0.83

TABLE 5.3: MA analysis from inverted K_2 based on two-dimensional experiment. Here, the two dimensions are data quantity (columns) and heterogeneity resolution (rows). HR denotes heterogeneity resolution and DQn denotes data quantity. Listed inverted Ks are the center values of resulting distributions.

HR \ DQn	12 wells	6 wells	3 wells
SIS	9.97	10.42	10.83
SA	9.98	10.69	10.42
Coarsening	9.61	9.94	12.16

TABLE 5.4: MP analysis from inverted K_2 based on two-dimensional experiment. Here, the two dimensions are data quantity (columns) and heterogeneity resolution (rows). HR denotes heterogeneity resolution and DQn denotes data quantity. Listed inverted Ks are the maximum deviations of resulting distributions.

HR \ DQn	12 wells	6 wells	3 wells
SIS	0.46	0.75	0.69
SA	0.66	1.09	1.38
Coarsening	0.83	0.69	2.3

In particular, some important co-effect features are revealed by this experiment. For MA, the center line exhibits bigger oscillation around the true value when either sampling wells are reduced or resolution is lower. The oscillation magnitude of MA for inverted K_1 is 0.09, 0.30, 0.40 ,and for inverted K_2, is 0.37, 0.75, 1.74, for 12 wells, 6 wells, and 3 wells, respectively. In terms of heterogeneity resolution, MA uncertainty yields 0.18, 0.33, 0.40 for K_1, and 0.86, 0.71, 2.55 for K_2, for SIS grids, SA grids, and Coarsening grids, respectively. It indicates that the decrease of data quantity can exaggerate the deterioration caused by heterogeneity resolution. Also, the change of heterogeneity resolution results in some mild change (K_1) or even fluctuation of MA uncertainty (K_2), so on the MA stability, data quantity has stronger impact than heterogeneity resolution.

Secondly, for precision, data quantity leads to different change trends between different

resolution grid. MP analysis shows that the difference in MP uncertainty range is 0.26, 0.61, and 0.53 for K_1 and 0.23, 0.72, 1.61 for K_2 by rows, and 0.15, 0.07, 0.43 for K_1 and 0.37, 0.40, 1.61 for K_2 by columns. Here, mild change or fluctuation in uncertainty is shown by the data based on columns. It implies that heterogeneity resolution is more influential to the MP uncertainty than data quantity. In addition, 3 wells always result in model deterioration leap, so observed data have to be fed on more than 3 wells for decent MP stability.

In terms of different sampling wells, with decrease of drilling wells, the difference in precision is increasingly smaller. Take inverted K_1s for example. The difference in uncertainty range is 0.15, 0.07, and 0.43 for 12 wells, 6 wells, 3 wells, respectively. The facts reveal that fewer sampled data will definitely aggravate the bias between original SIS grids and other grids, but between modified grids, the variation caused by further modification will be increasingly smaller if data quantity decreases.

Finally, for inverted Ks, different parameters are reckoned among the priority in different model criteria. With respect to MA, the largest variation of center lines is 0.09, 0.3, and 0.4 for 12 wells, 6 wells, and 3 wells; the same quantity is 0.18, 0.24, 0.4 for SIS grids, SA grids, and Coarsening grids. With respect to MA, the maximum variation of different uncertainty region lengths is 0.15, 0.07, 0.42 for 12 wells, 6 wells, and 3 wells; the same quantity is 0.26, 0.59, and 0.53 for SIS grids, SA grids, and Coarsening grids. From these quantifications, data quantity will influence MA more than heterogeneity resolution; MP is more affected by heterogeneity resolution than data quantity.

5.3.1.3 BC, MA, and MP

To understand the information from inverted BCs better, the discussion is still organized by four sections, including $\boldsymbol{a}-\boldsymbol{b}$, $\boldsymbol{b}-\boldsymbol{c}$, $\boldsymbol{c}-\boldsymbol{d}$, and $\boldsymbol{d}-\boldsymbol{a}$.

$\boldsymbol{a}-\boldsymbol{b}$: The MA and MP analysis results reveal some distinct features of inverse model. Generally, with the decrease of data quantity and heterogeneity resolution, MA and MP will be both worsen. MA analysis results show 6.51, 10.59, 40.90 along the diagonal of the Table 5.5; MP analysis results show 18.02, 24.56, 37.80 along the diagonal of the Table 5.6. The model precision relies on the impact of data quantity; the model accuracy will be more influenced by upscaling strategy.

Meanwhile, MA and MP uncertainties depend on heterogeneity resolution. MA analysis results show the uncertainty of 4.43, 8.34, 30.83 by rows; MA analysis results show the

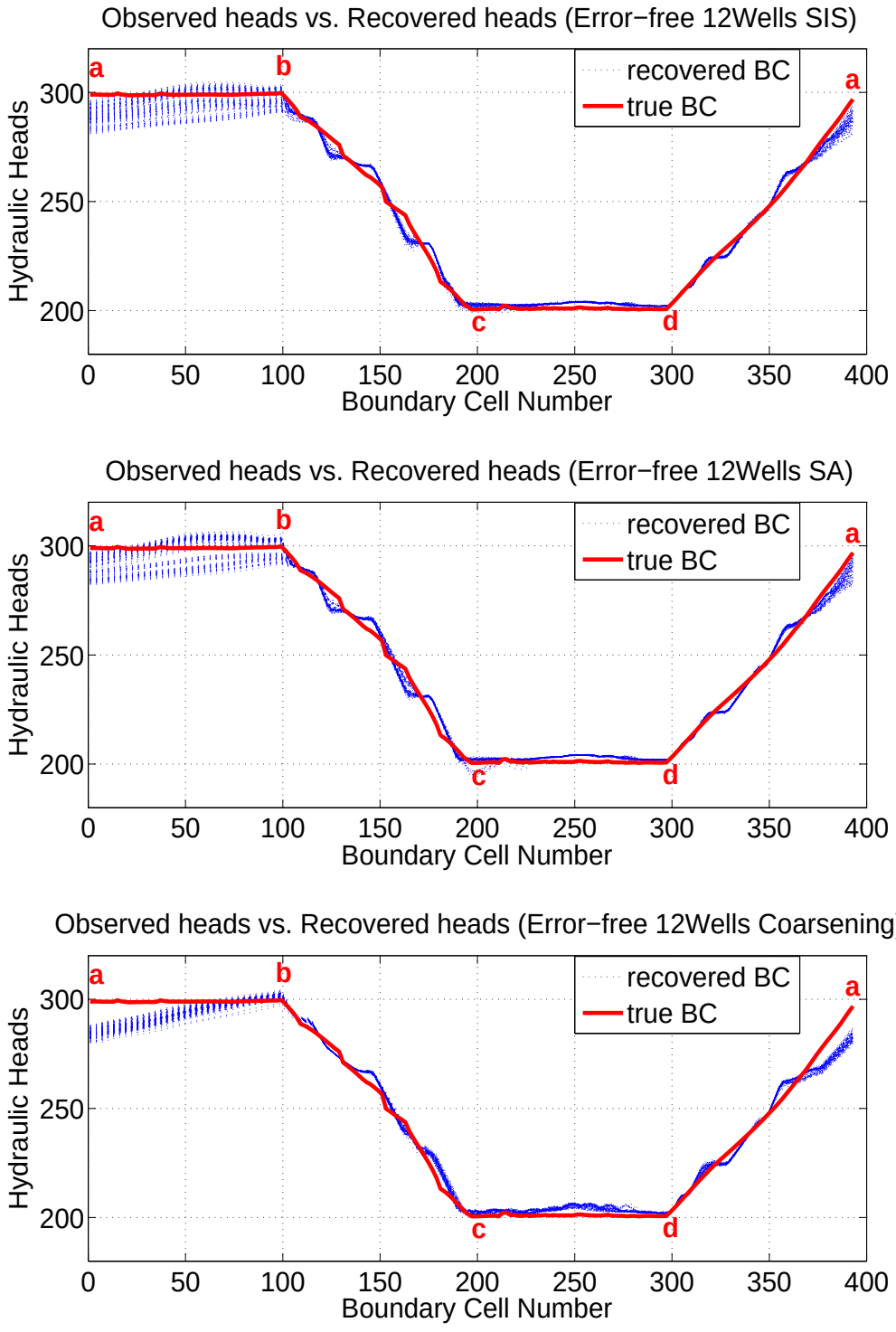

FIGURE 5.14: BCs uncertainty analysis based on 12 wells and different heterogeneity resolution. The letters of alphabet denote the boundary locations. Hydraulic heads are recovered conditions and boundary cell number is the index of each boundary cell.

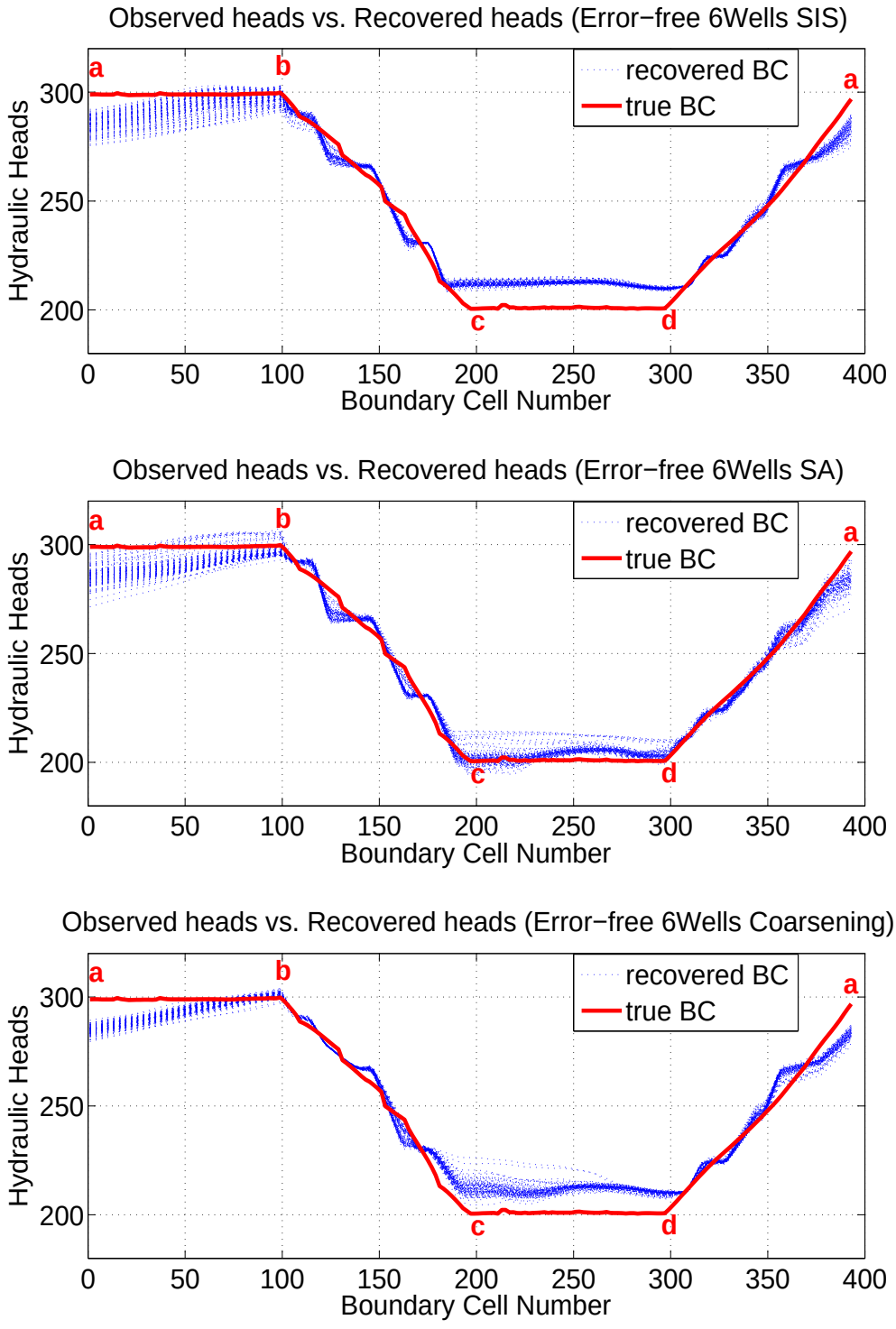

FIGURE 5.15: BCs uncertainty analysis based on 6 wells and different heterogeneity resolution. The letters of alphabet denote the boundary locations. Hydraulic heads are recovered conditions and boundary cell number is the index of each boundary cell.

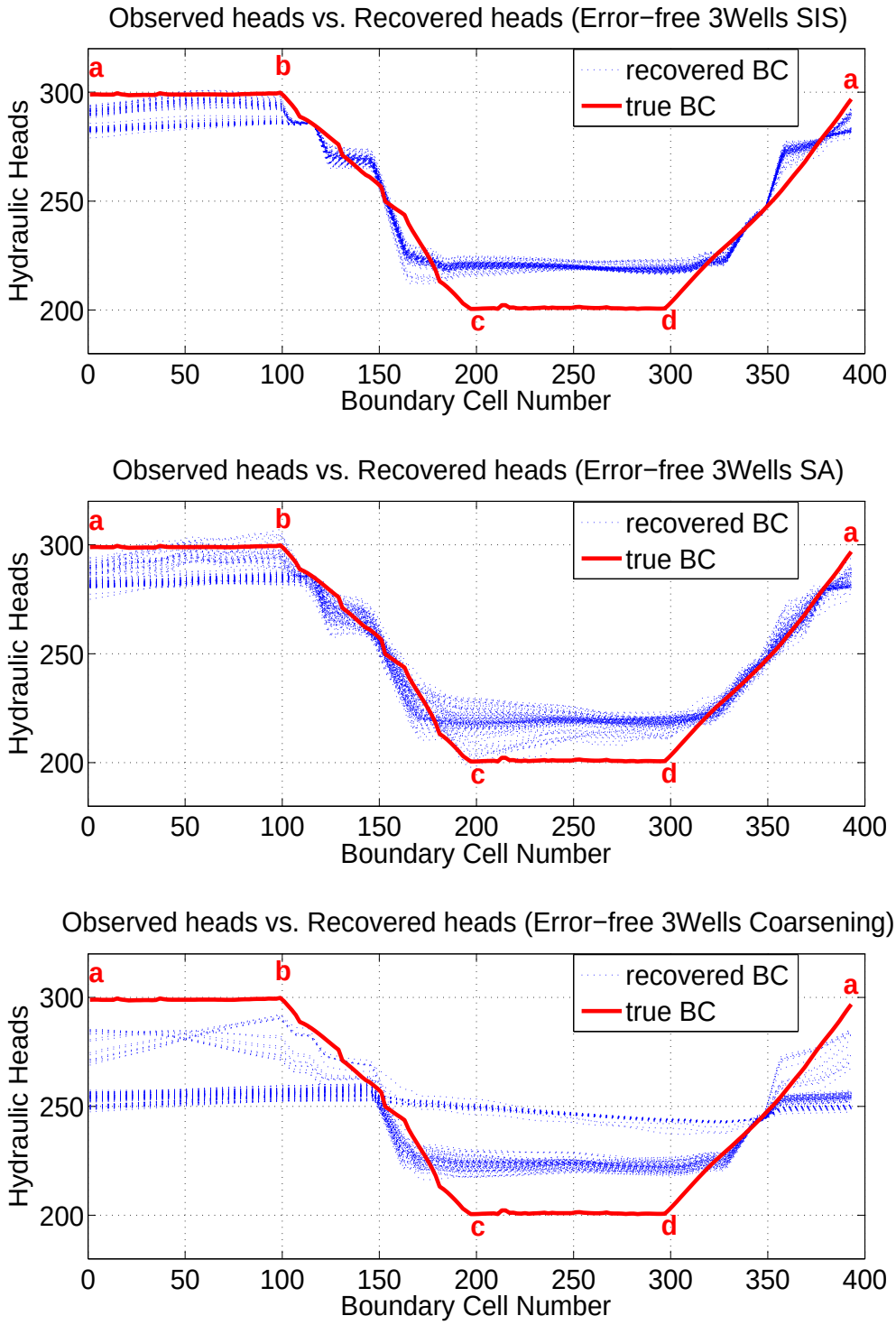

FIGURE 5.16: BCs uncertainty analysis based on 3 wells and different heterogeneity resolution. The letters of alphabet denote the boundary locations. Hydraulic heads are recovered conditions and boundary cell number is the index of each boundary cell.

TABLE 5.5: MA analysis from inverted BCs based on two-dimensional experiment. Here, the two dimensions are data quantity (columns) and heterogeneity resolution (rows). Tabulated inverted results are the deviations of resulting distributions from the true conditions at different sections of the entire boundary.

section ***ab***			
	12 wells	6 wells	3 wells
SIS	6.51	10.35	10.94
SA	4.88	10.59	13.22
Coarsening	10.17	10.07	40.90
section ***bc***			
	12 wells	6 wells	3 wells
SIS	2.31	3.49	9.23
SA	0.21	4.10	10.85
Coarsening	0.88	1.33	39.62
section ***cd***			
	12 wells	6 wells	3 wells
SIS	0.67	1.13	1.71
SA	0.33	0.63	3.39
Coarsening	-1.20	-1.19	19.35
section ***da***			
	12 wells	6 wells	3 wells
SIS	0.11	-1.84	-1.81
SA	-0.45	-0.02	-2.86
Coarsening	-1.93	-4.05	-9.67

uncertainty of 5.29, 0.52, 29.96 by columns. The results imply that lower heterogeneity resolution will exaggerate the variation of MA which states that the robustness of the model is weaken; fewer data do not cause poorer MA all the time unless data quantity is far from sufficient. MP analysis results show the uncertainty of 1.15, 5.37, 28.09 by rows; MP analysis results show the uncertainty of 9.48, 14.77, 20.26 by columns. The results imply that lower heterogeneity resolution can result in the larger variation of MP which states that the robustness of the model is weaken; fewer data will also cause lower MP but its influence is a little weaker than the impact of heterogeneity resolution.

Furthermore, the results provide some information on data sampling strategy. When the table is further examined, it is obtained that 3 wells always cause severely bad model outcomes regardless of MA or MP. This deterioration indicates that 3 sampling wells fail to supply sufficient input data for a good model result, which determines poorer model performance. When the results from 3 wells are taken out, it is detected that Coarsening grid improves the uncertainty of MA and MP, which implies that upscaling

TABLE 5.6: MP analysis from inverted BCs based on two-dimensional experiment. Here, the two dimensions denote data quantity (columns) and heterogeneity resolution (rows). Tabulated inverted results are the maximum fluctuation range of resulting distributions at different sections of the entire boundary.

section ***ab***			
	12 wells	6 wells	3 wells
SIS	18.02	19.09	17.54
SA	19.19	24.56	21.61
Coarsening	9.71	9.79	37.80
section ***bc***			
	12 wells	6 wells	3 wells
SIS	18.21	19.06	17.59
SA	19.48	20.26	25.44
Coarsening	9.50	9.10	39.87
section ***cd***			
	12 wells	6 wells	3 wells
SIS	8.91	10.10	10.43
SA	9.16	11.94	22.17
Coarsening	5.67	5.58	37.98
section ***da***			
	12 wells	6 wells	3 wells
SIS	7.72	7.94	17.96
SA	8.74	20.94	31.77
Coarsening	6.69	21.72	38.31

can improve the robustness of MR. In particular, Coarsening grid yields the model with much higher precision, and thus, the improvement on MP can be offered by upscaling.

$\boldsymbol{b-c}$: Within this inverted section, MA and MP provide some different features. Generally, with the decrease of data quantity and heterogeneity resolution, MA and MP are both worsen. MA analysis results show 2.31, 4.10, 39.62 along the diagonal of the Table 5.5; MP analysis results show 18.21, 20.26, 39.87 along the diagonal of the Table 5.6. Both exhibit a non-linear trend of result deterioration which implies that upscaling and shrunk data pool can result in worse inverted results on this region. Especially, excessive upscaling or over shrunk data sets can faster the deterioration speed.

Meanwhile, MA and MP uncertainties depend on the heterogeneity resolution. MA analysis results show the uncertainty of 6.92, 10.64, 38.74 by rows; MA analysis results show the uncertainty of 2.1, 2.77, 30.39 by columns. The results imply that lower heterogeneity resolution or fewer data will exaggerate the variation of MA, which states that the robustness of the model is weaken. MP analysis results show the uncertainty

of 1.47, 5.96, 30.77 by rows; MP analysis results show the uncertainty of 9.98, 11.16, 22.28 by columns. The results imply that lower heterogeneity resolution can result in the larger variation of MP, which states that the robustness of the model is weaken; fewer data will also cause lower MP but the non-linear feature is not as discernable as the trend of heterogeneity resolution.

Furthermore, some factors will play a more important role in modeling this section, especially data quantity. If the Table 5.5 and Table 5.6 are further examined, it can be obtained that 3 wells adversely affect MA and MP, and especially, MA exhibits some dramatic feature when sampling wells are reduced from 6 wells to 3 wells. This deterioration indicates that the data from 3 wells cannot satisfy the need of model, especially MA, from which worse model performance occurs.

Similar to the section $\boldsymbol{a} - \boldsymbol{b}$, Coarsening grid improves the uncertainty of MA and MP if the results of 3 wells are removed, which implies that upscaling can improve the robustness of MR. In particular, Coarsening grid yields the model with much higher precision, and thus, the improvement on MP can be offered by upscaling.

$\boldsymbol{c} - \boldsymbol{d}$: Within this inverted section, MA and MP provide some similar features to the results from the section $\boldsymbol{b} - \boldsymbol{c}$. Generally, with decrease of data quantity and heterogeneity resolution, MA and MP are both worsen. MA analysis results show 0.67, 0.63, 19.35 along the diagonal of the Table 5.5table; MP analysis results show 8.91, 11.94, 37.98 along the diagonal of the Table 5.6. Both exhibit non-linear trends of result deterioration which implies that excessive upscaling or over shrunk data sets can faster the deterioration speed. For MA, within a certain range, simultaneous reduction on resolution and data can provide stable model outcomes.

Meanwhile, MA uncertainty and MP uncertainty both depend on heterogeneity resolution. MA analysis results show the uncertainty of 1.04, 3.06, 20.55 by rows; MA analysis results show the uncertainty of 1.87, 2.32, 17.64 by columns. The results imply that lower heterogeneity resolution or fewer data can worsen the variation of MA, which states that the robustness of the model is weaken. Within some region, this impact is relatively slighter. Also, from both of these trends, these two factors have closely equal impact on the uncertainty of MA. MP analysis results show the uncertainty of 1.52, 13.01, 32.40 by rows; MP analysis results show the uncertainty of 3.49, 6.36, 27.55 by columns. These facts reveal larger variation than the results from MA analysis. Lower heterogeneity

resolution can result in the larger variation of MP, which states that the model robustness is weaken; fewer data can also cause lower MP, and here, the non-linear feature is stronger than the trend exhibited by heterogeneity resolution.

Furthermore, data sufficiency issue is also noticeable in this section. If Table 5.5 and Table 5.6 are further examined, it will be obtained that 3 wells adversely affect MA and MP, and especially, the uncertainty of MP shows a leap between 6 wells and 3 wells. This deterioration indicates that the data demand for decent model precision is much larger than the data feed from 3 sampling wells, which gives rise to the worse model outcomes. Similar to the section $\boldsymbol{b}-\boldsymbol{c}$, Coarsening grid improves the uncertainty of MA and MP if the results of 3 wells are removed, which implies that upscaling can improve the robustness of MR. In particular, Coarsening grid yields the model with much higher precision, and thus, the improvement on the model precision can be offered by upscaling.

$\boldsymbol{d}-\boldsymbol{a}$: Within this inverted section, MA and MP provide similar general characteristics although there are some slightly different features to the results from other sections. With decrease of data quantity and heterogeneity resolution, MA and MP are both worsen. MA analysis results show 0.11, -0.02, -9.67 along the diagonal of the Table 5.5; MP analysis results show 7.72, 20.94, 38.31 along the diagonal of the Table 5.6. Both exhibit non-linear trends of result deterioration which implies that excessive upscaling or over shrunk data sets can faster the deterioration speed. For MA, within a certain range, simultaneous reduction on resolution and data can provide stable model outcomes.

Meanwhile, MA uncertainty and MP uncertainty both depend on the heterogeneity resolution. MA analysis results show the uncertainty of 1.95, 2.84, 7.74 by rows; MA analysis results show the uncertainty of 2.04, 4.03, 7.86 by columns. The results imply that lower heterogeneity resolution or fewer data can worsen the variation of model accuracy, which states that the robustness of the model is weaken. This section shows much slighter variation results than other sections, which indicates data quantity and heterogeneity resolution have less impact on this section. Also, from both of these trends, these two factors have closely equal impact on the uncertainty of MA. MP analysis results show the uncertainty of 10.24, 23.03, 31.62 by rows; MP analysis results show the uncertainty of 2.05, 13.78, 20.35 by columns. These facts reveal larger variation than the results from MA analysis. The decrease of data quantity can result in the larger variation of model precision, which states that the robustness of the model is weaken; fewer data will also cause lower MP, and here, the linear feature is stronger than the trend of heterogeneity resolution.

Data sufficiency issue becomes more noticeable in this section. If Table 5.5 and Table 5.6 are further examined, it can be obtained that the adverse effect on the MA and MP starts at 6 wells, and especially, the uncertainty of MP shows a leap between 12 wells and 6 wells. This deterioration indicates that decent modeling on this section requires more data than the sampled data from 6 wells. Slightly different from other sections, the precision improvement from Coarsening grid is overshadowed by the deficiency of data quantity in this section. Even if the improvement is still exhibited by 12 wells, the improvement is very limited. This fact indicates that sufficient data quantity plays a prominent role in precision improvement.

5.3.1.4 Discussion on Data Quantity and Heterogeneity Resolution

From the uncertainty analysis above, data quantity and heterogeneity resolution take different roles in inverse model. Generally, fewer data will exaggerate the deterioration of MA and MP caused by heterogeneity resolution decrease; data quantity has a larger influence on MU than heterogeneity resolution. In particular, when drilling wells ared decreased to 3 wells, the difference in inverted results based on different heterogeneities becomes dramatically larger, which indicates MRs of different resolutions have to been ensured by sufficient observed data.

For inverted BCs, each section exhibits differen features. The section $\boldsymbol{a}-\boldsymbol{b}$ has strong stability to the change of data quantity or heterogeneity resolution. The section $\boldsymbol{b}-\boldsymbol{c}$ and the section $\boldsymbol{c}-\boldsymbol{d}$ have some similar MU behavior. However, the section $\boldsymbol{c}-\boldsymbol{d}$ is more robust to condition change, and thus, the section $\boldsymbol{b}-\boldsymbol{c}$ is more influenced by data quantity and heterogeneity resolution. Moreover, the section $\boldsymbol{d}-\boldsymbol{a}$ is most robust to any change from data quantity and heterogeneity resolution when data quantity is sufficient. According to the resultant data, the number of sampled wells have to be more than 6 to ensure the data feeding for the section $\boldsymbol{d}-\boldsymbol{a}$. Generally speaking, extrapolation regions exhibit weak instability to the change of data quantity; with the decrease of heterogeneity resolution, MP is improved while MA becomes poorer. More than 3 sampled wells are capable of supporting sufficient data input for all sections but the section $\boldsymbol{d}-\boldsymbol{a}$. Also, the uncertainty of MA and MP makes it possible to predict model behavior based on current model status.

TABLE 5.7: MA analysis from inverted K_1 based on two-dimensional experiment. The two dimensions are data quantity (rows) and data quality(columns). The value in each cell denotes the center line of different resultant distributions generated under the correspondent condition.

DQn \ DQl	0	±1%	±2%	±5%	±10%
12 wells	1	0.97	0.93	0.71	0.24
6 wells	1.15	1.13	1.04	0.58	-0.02
3 wells	1.18	1.17	1.12	0.58	-0.56

5.3.2 Data Quantity and Data Quality

5.3.2.1 Experimental Conditions

The second experiment is to examine the co-effect of data quantity and data quality on the inverted Ks and BCs. The condition of this experiment is set as decreased drilling wells, i.e., 12 wells, 6 wells, and 3 wells, and the increasing data errors, i.e., ±1%, ±2%, ±5%, and ±10%, base on the THV. Here, the heterogeneity resolution is set to SIS grid. Due to the decrease of sampling wells, observed K sets are shrunk and SIS simulation results exhibit increasingly lower accuracy. Observed data errors are still added to hydraulic head data, and corruption levels refer to the SD of the data based on the THV. Under these conditions, several experiments are conducted and the experiment provides the different results of Ks and BCs as illustrated by Figure 5.17, Figure 5.18, Figure 5.19, Figure 5.20, Figure 5.21, Figure 5.22, and Figure 5.23.

5.3.2.2 K, MA, and MP

For inverted Ks, the general features reflected by relevant single factor analysis are also preserved in the co-effect uncertainty analysis. For each drilling well strategy, fewer data are lead to lower accuracy and lower precision generally. Basically, data errors corrupt model quality under the condition of same data quantity. Moreover, K_1 and K_2 yield similar distribution pattern changes when different factors are perturbed. Still, K_2 exhibits milder change than K_1 when the conditions are perturbed. Therefore, the uncertainty research on Ks adopts the inverted K_1s to explore the co-effect. The specific characteristics for each distribution patterns are tabulated by Table 5.7, Table 5.8, Table 5.9, and Table 5.10.

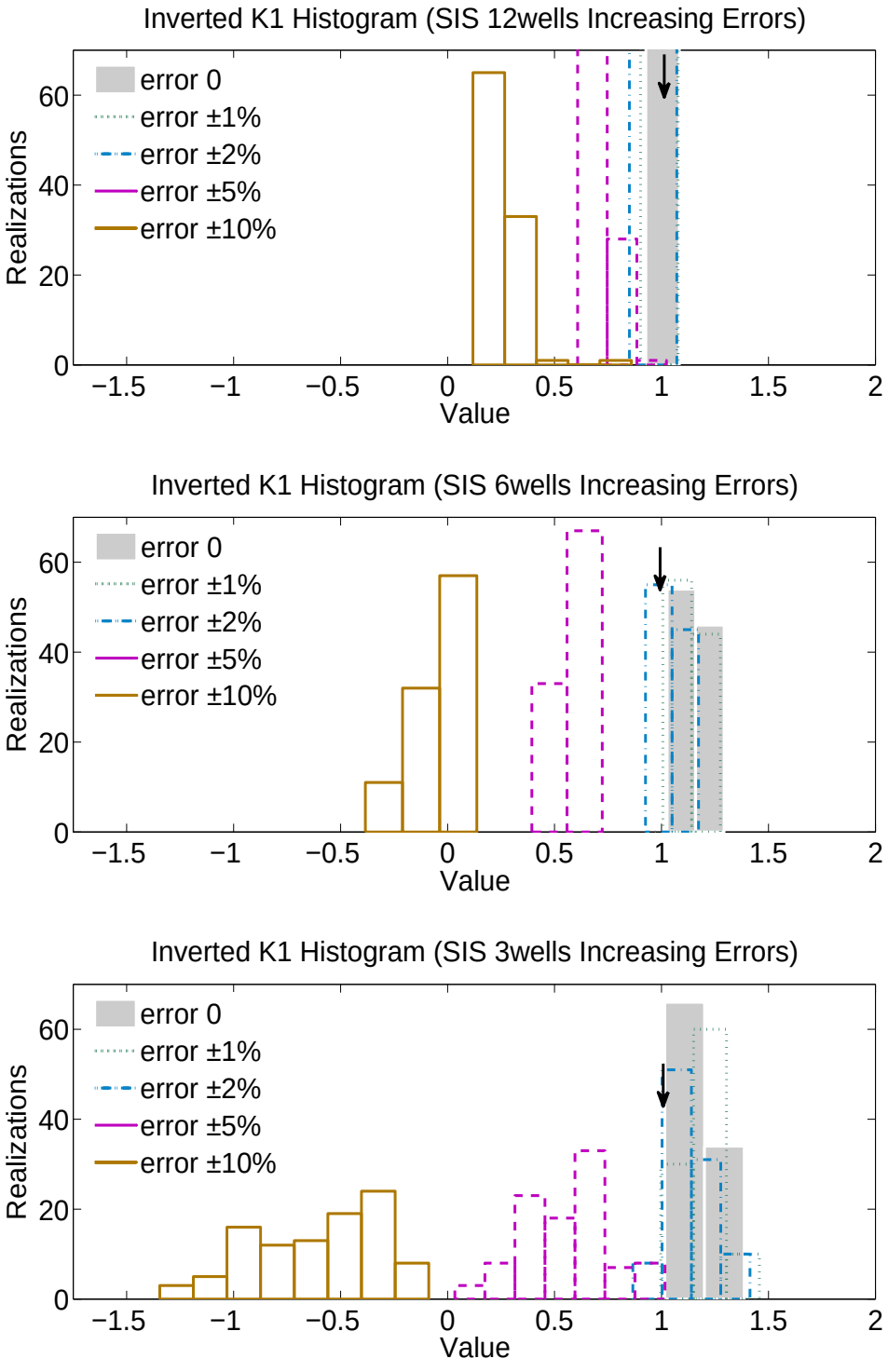

FIGURE 5.17: K_1 uncertainty analysis based on data quantity and data quality. The arrows point to the true values. The realizations denote the frequency within different value range which reflects uncertainty regions.

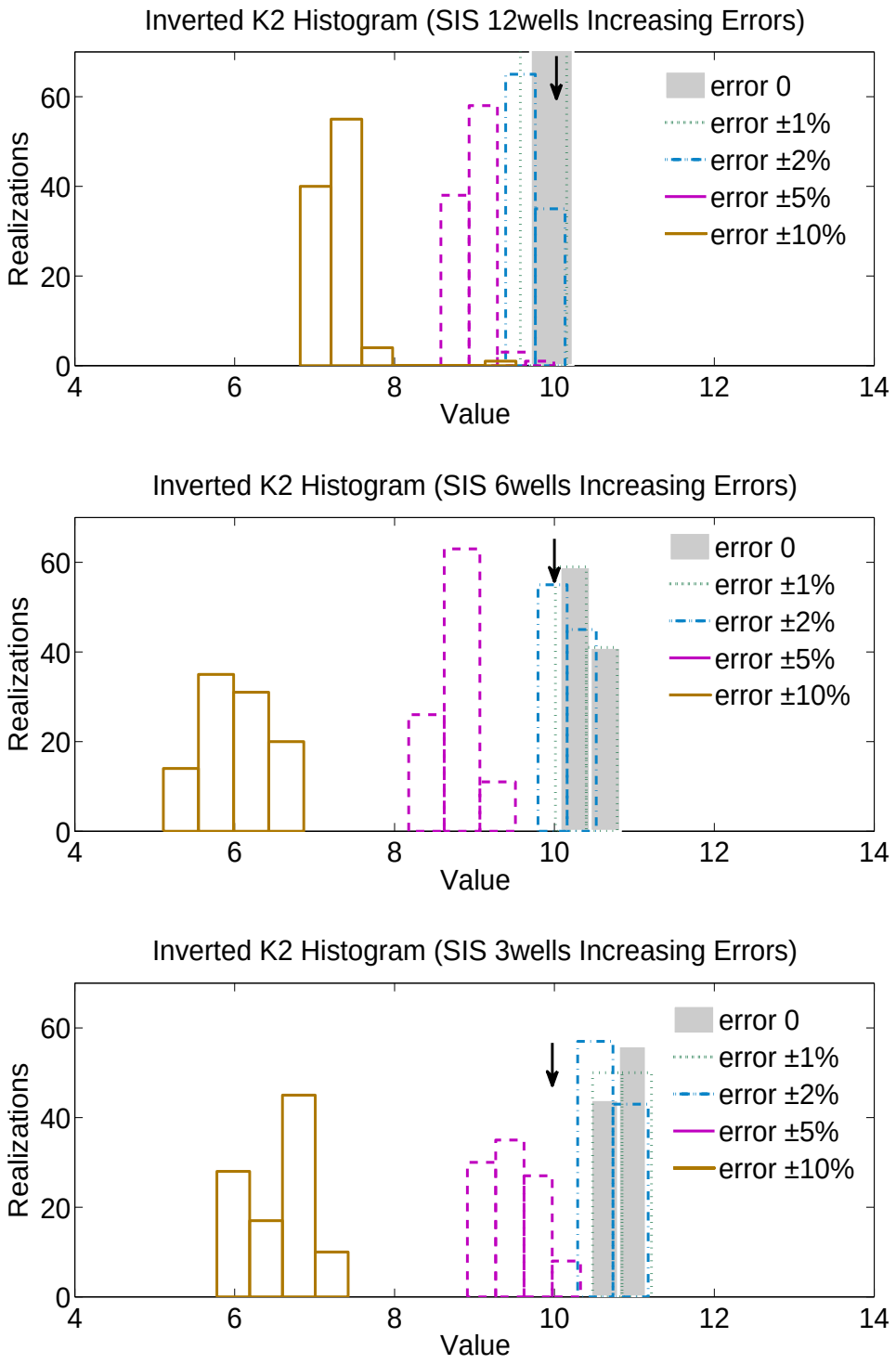

FIGURE 5.18: K_2 uncertainty analysis based on data quantity and data quality.The arrows point to the true values. The realizations denote the frequency within different value range which reflects uncertainty regions.

TABLE 5.8: MP analysis from inverted K_1 based on two-dimensional experiment. The two dimensions are data quantity (rows) and data quality(columns). The value in each cell denotes the length of the resultant uncertainty region generated under the correspondent condition.

DQn \ DQl	0	±1%	±2%	±5%	±10%
12 wells	0.15	0.17	0.19	0.26	0.29
6 wells	0.22	0.23	0.25	0.33	0.54
3 wells	0.37	0.46	0.55	0.98	1.26

TABLE 5.9: MA analysis from inverted K_2 based on two-dimensional experiment. The two dimensions are data quantity (rows) and data quality(columns). The value in each cell denotes the center line of different resultant distributions generated under the correspondent condition.

DQn \ DQl	0	±1%	±2%	±5%	±10%
12 wells	9.97	9.87	9.71	8.97	7.26
6 wells	10.42	10.36	10.16	8.79	6.00
3 wells	10.83	10.84	10.71	9.53	6.63

TABLE 5.10: MP analysis from inverted K_2 based on two-dimensional experiment. The two dimensions are data quantity (rows) and data quality(columns). The value in each cell denotes the length of the resultant uncertainty region generated under the correspondent condition.

DQn \ DQl	0	±1%	±2%	±5%	±10%
12 wells	0.46	0.58	0.61	0.89	0.98
6 wells	0.75	0.78	0.73	1.34	1.76
3 wells	0.69	0.74	0.88	1.42	1.64

MA results show 1, 1.13, 1.12; 0.97, 1.04, 0.58; 0.93, 0.58, -0.56 for K_1 along the diagonal of the Table 5.7 and 9.97, 10.36, 10.71; 9.87, 10.16, 9.53; 9.71, 8.79, 6.63 for K_2 along the diagonal of the Table 5.9. In general, MA is deteriorated by worse data conditions regardless of underestimation or overestimation. K_1 exhibits faster deterioration speed, especially when the data errors are larger than ±5% of THV. MP results show 0.15, 0.23, 0.55; 0.17, 0.25, 0.98; 0.19, 0.33, 1.26 for K_1 along the diagonal of the Table 5.8 and 0.46, 0.78, 0.88; 0.58, 0.73, 1.42; 0.61, 1.34, 1.64 for K_2 along the diagonal of the Table 5.10. Both of the inverted K exhibit increasingly lower precision when either data condition is worse. Also, K_1 shows weak robustness to data condition change. Especially, the precision change trends have leaps when 6 wells are reduced to 3 wells, which implies that 3 wells presumably fail to satisfy the basic data demand of inverse model.

MA analysis results show the uncertainty of 0.76, 1.17, 1.64 for K_1 and 2.71, 4.42, 4.21 for K_2 by rows; MA analysis results show the uncertainty of 0.18, 0.20, 0.19, 0.23, 0.80 for K_1 and 0.86, 0.97, 1, 0.74, 1.26 for K_2 by columns. The MA uncertainty is deteriorated when data quantity is reduced. Data errors, compared to data quantity, exhibits much weaker impact on the model outcome in terms of accuracy uncertainty. This feature is better shown when data error is less than ±5% of THV. Therefore, MA is robust to data corruption when the error is not extremely high.

MP analysis results show the uncertainty of 0.14, 0.32, 0.89 for K_1 and 0.52, 1.03, 0.95 for K_2 by rows; MP analysis results show the uncertainty of 0.22, 0.39, 0.36, 0.72, 0.97 for K_1 and 0.29, 0.20, 0.27, 0.53, 0.78 for K_2 by columns. The MP uncertainty basically becomes wider when data conditions are worse. Similar to accuracy uncertainty, precision uncertainty is more sensitive to data quantity change; however, data error has more influence on precision uncertainty than accuracy uncertainty.

From the analysis above, some primary conditions for good inverse model outcomes are revealed. First, sufficient data are primary for quality inverted Ks. Taking inverted K_1 for example, Table 5.7 and Table 5.8 show the larger model disturbance by the decrease of sampling wells. Next, data error can affect the stability of MP uncertainty while MA uncertainty is stable if the data error is not extremely high. The stability of MA uncertainty implies the possibility of model behavior prediction.

5.3.2.3 BC, MA, and MP

Here, the analysis on recovered BCs is still organized by four sections including $\boldsymbol{a}-\boldsymbol{b}$, $\boldsymbol{b}-\boldsymbol{c}$, $\boldsymbol{c}-\boldsymbol{d}$, and $\boldsymbol{d}-\boldsymbol{a}$.

$\boldsymbol{a}-\boldsymbol{b}$: The MA and MP analysis results reveal some distinct features different from DQn-HR analysis. Generally, with deteriorated conditions, MA exhibits fluctuation and MP shows increasing lower trend. MA analysis results show 6.51, 8.37, 12.17; 6.56, 6.12, 12.12; 6.55, -2.12, 7.15 along the diagonals of the Table 5.11. From these facts, when the data error magnitude is within ±2%, the model deterioration is shown; when the data error is more than ±2% of THV, the fluctuation is obtained and the MA deterioration is uncertain. MP analysis results show 18.02, 18.84, 17.52; 18.81, 21.52, 23.06; 19.58, 29.31, 43.18 along the diagonal of the Table 5.12. Compared to MA, the MP deterioration is relatively clearer, especially when the result based on both ±2% error and 3 wells is taken out. The precision is increasingly lower when data quality is worse or data quantity is fewer.

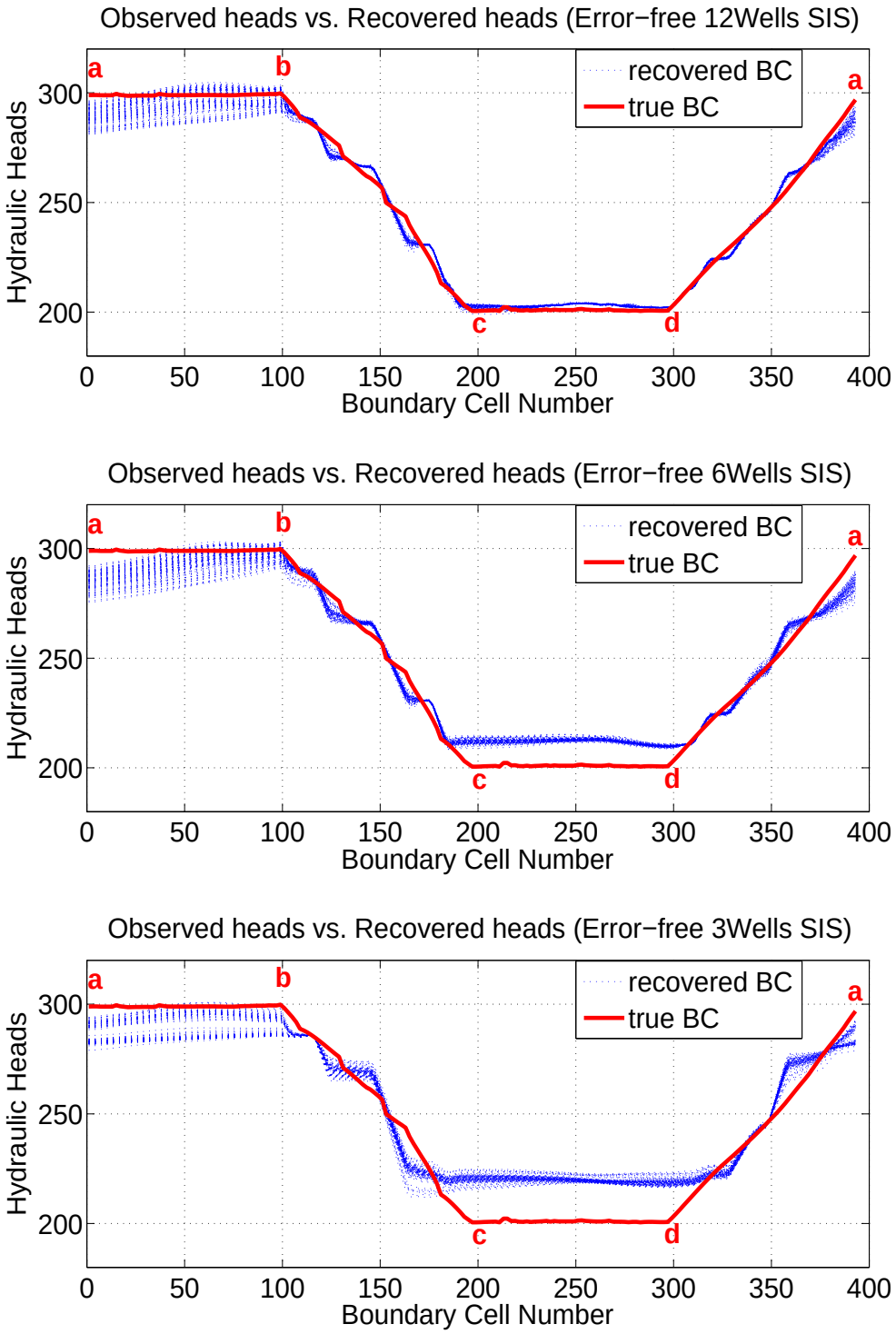

FIGURE 5.19: *BCs* uncertainty analysis based on different wells and error-free data. The letters of alphabet denote the boundary locations. Hydraulic heads are recovered conditions and boundary cell number is the index of each boundary cell.

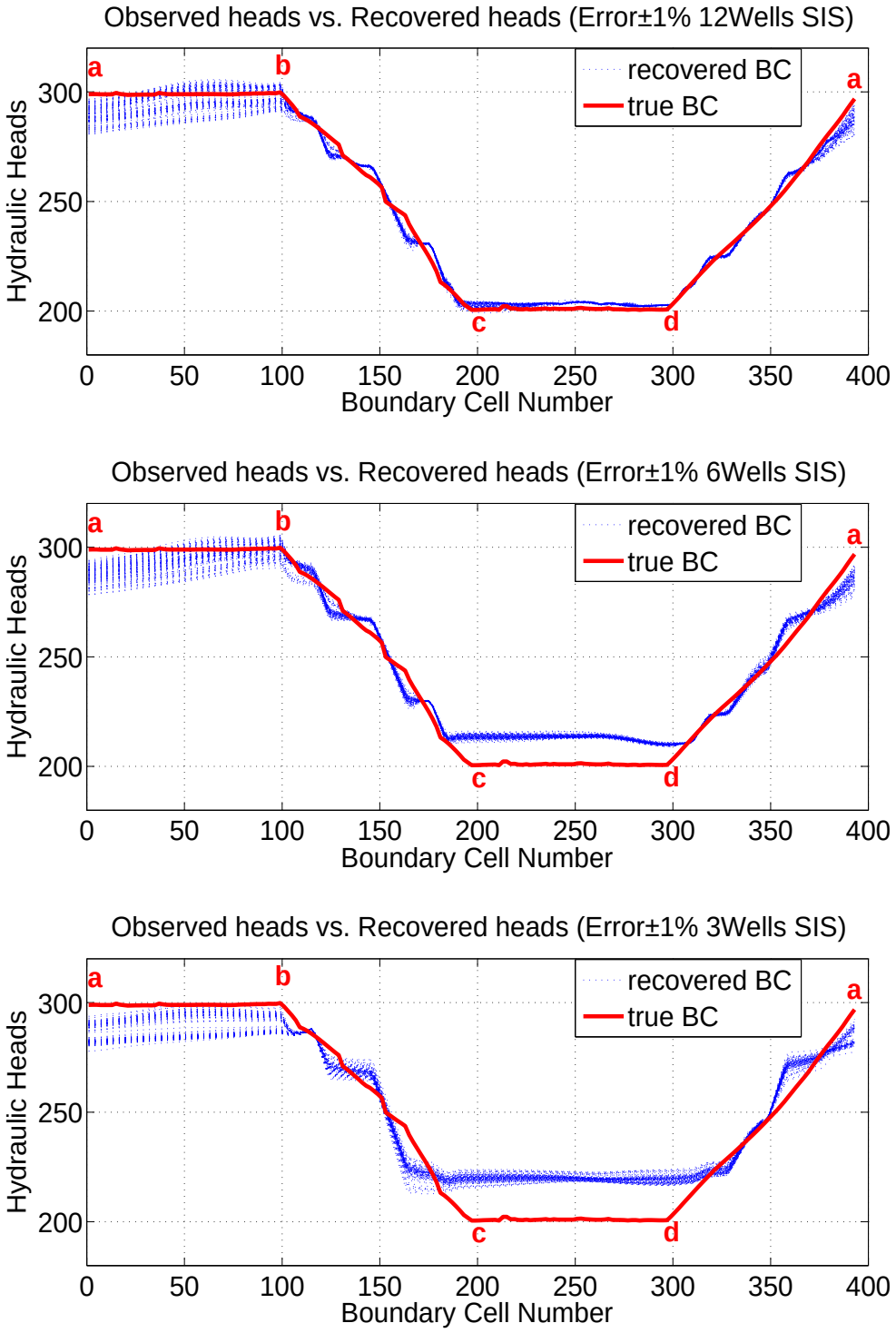

FIGURE 5.20: *BCs* uncertainty analysis based on different wells and observed hydraulic head with error±1% of THV. The letters of alphabet denote the boundary locations. Hydraulic heads are recovered conditions and boundary cell number is the index of each boundary cell.

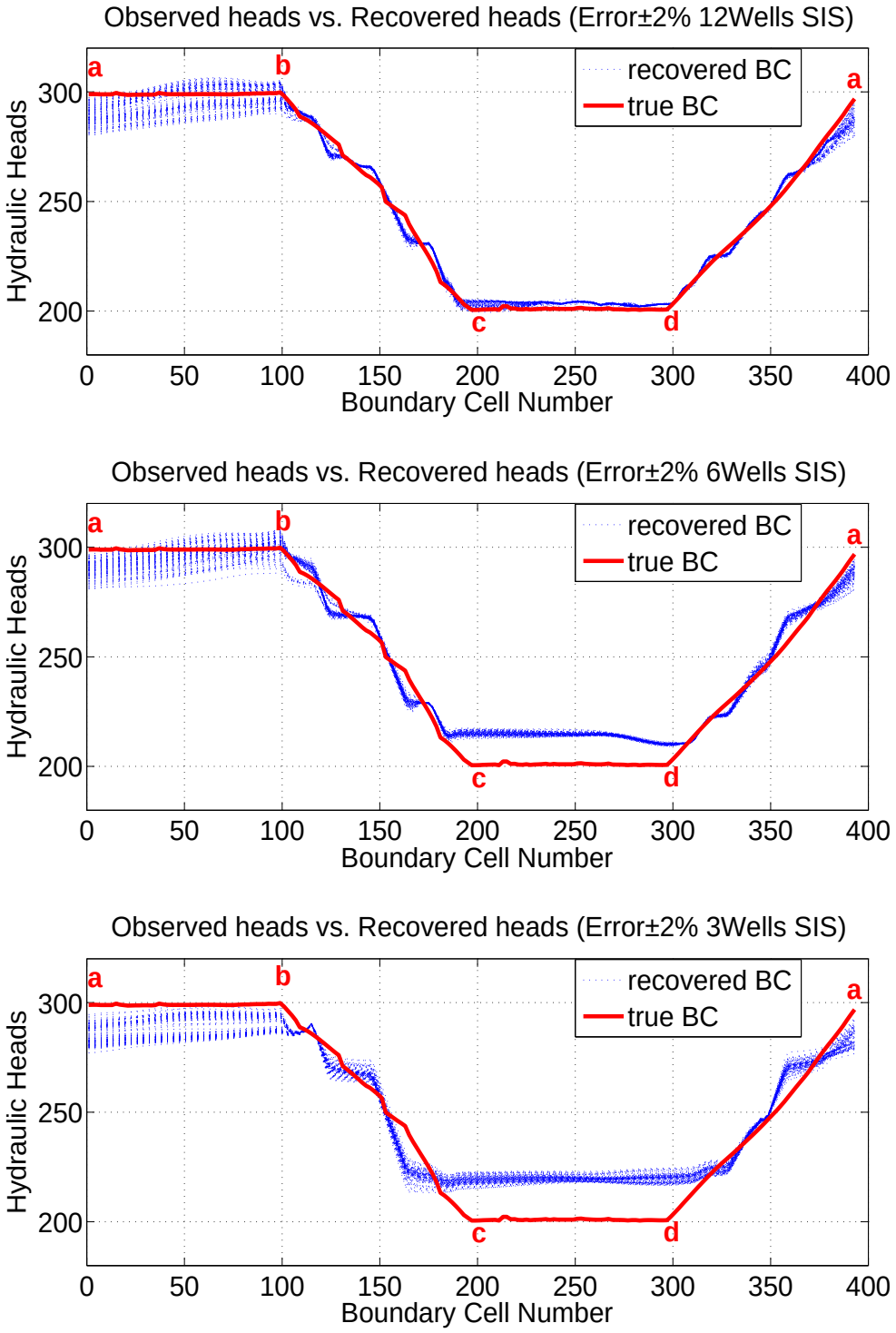

FIGURE 5.21: *BCs* uncertainty analysis based on different wells and observed hydraulic head with error±2% of THV. The letters of alphabet denote the boundary locations. Hydraulic heads are recovered conditions and boundary cell number is the index of each boundary cell.

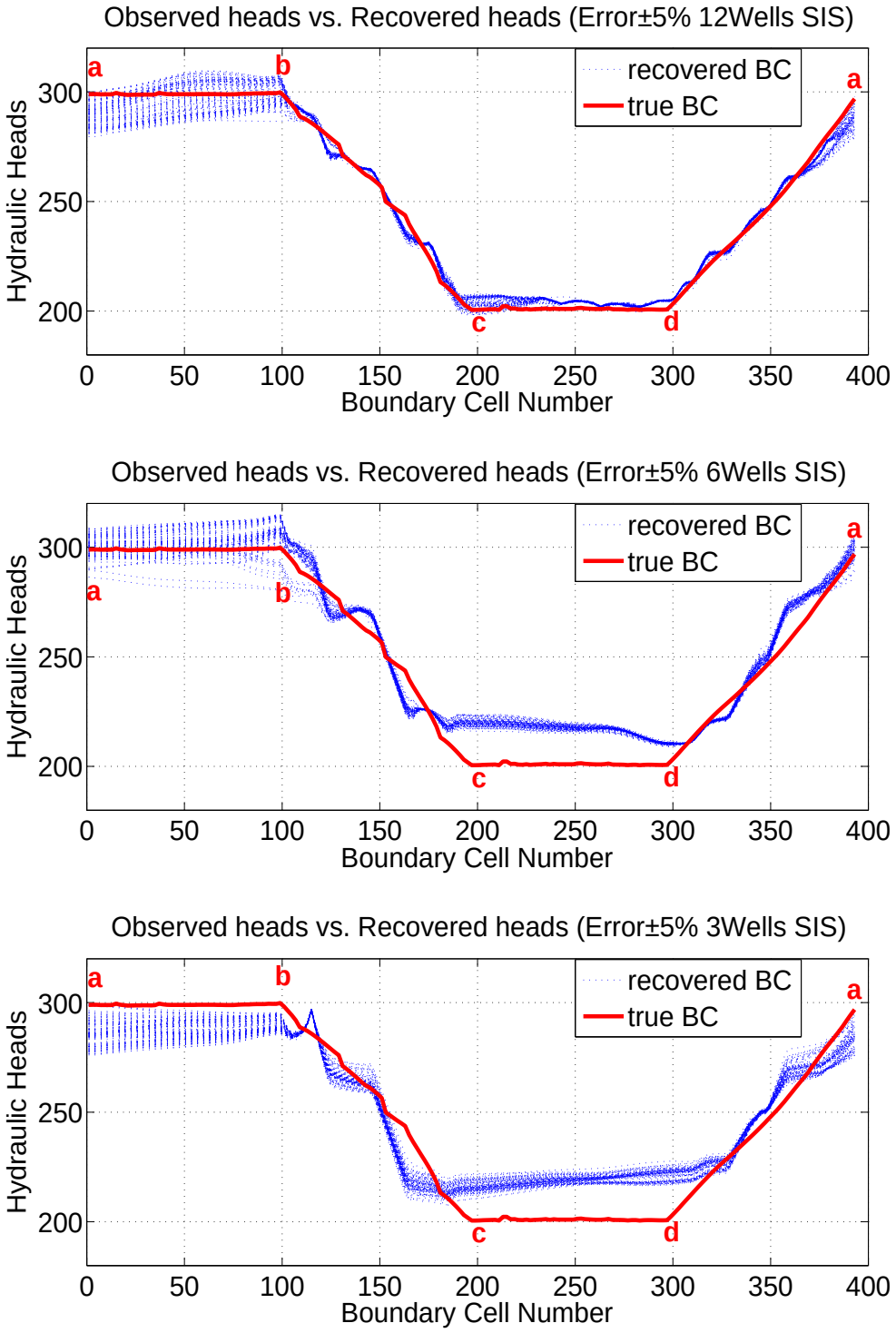

FIGURE 5.22: *BCs* uncertainty analysis based on different wells and observed hydraulic head with error±5% of THV. The letters of alphabet denote the boundary locations. Hydraulic heads are recovered conditions and boundary cell number is the index of each boundary cell.

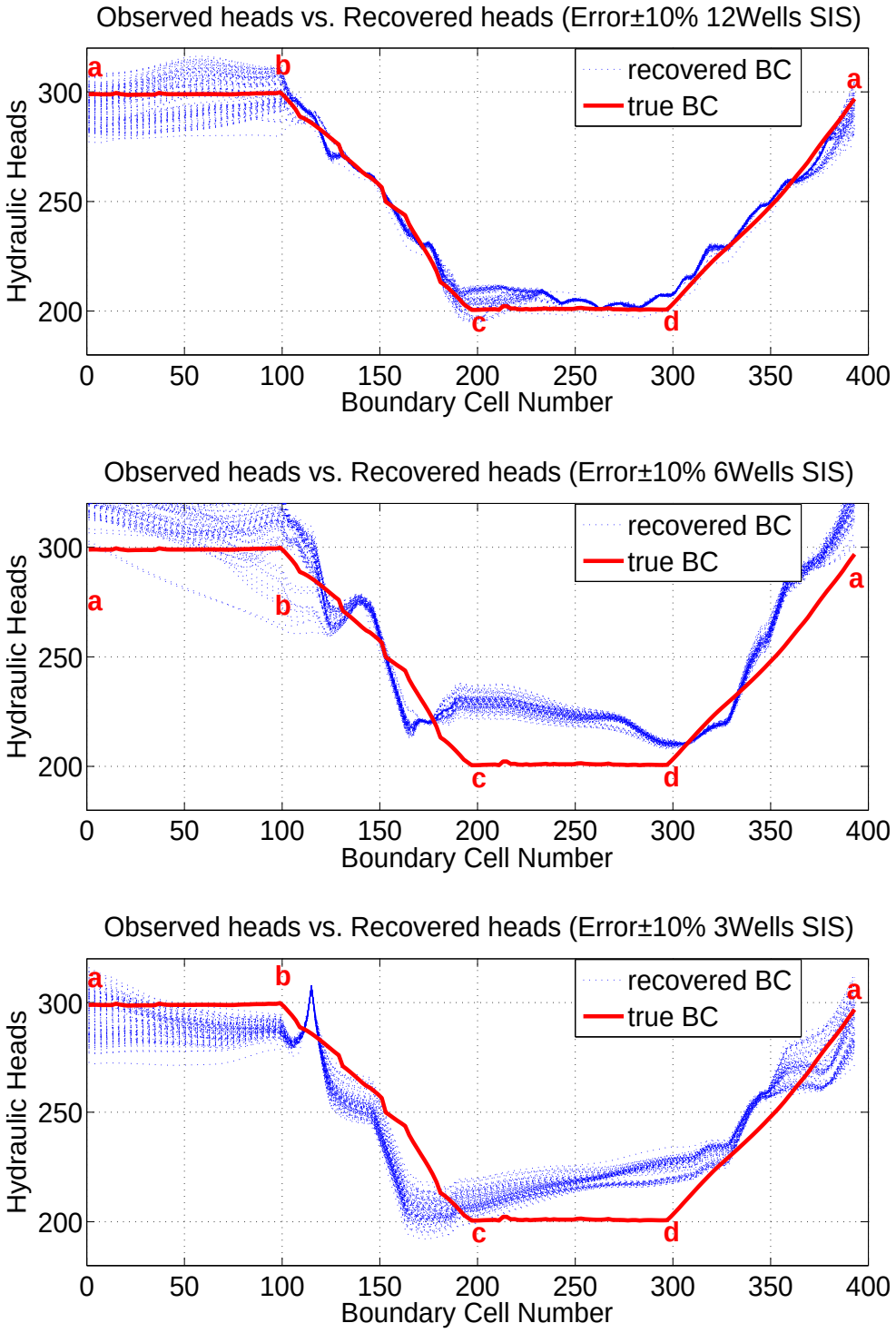

FIGURE 5.23: *BCs* uncertainty analysis based on different wells and observed hydraulic head with error±10% of THV. The letters of alphabet denote the boundary locations. Hydraulic heads are recovered conditions and boundary cell number is the index of each boundary cell.

TABLE 5.11: MA analysis from inverted BCs based on two-dimensional experiment. Here, the two dimensions are data quality (columns) and data quantity (rows). Tabulated inverted results are the deviations of resulting distributions from the true conditions at different sections of the entire boundary.

section ***ab***					
	0	±1%	±2%	±5%	±10%
12 wells	6.51	6.56	6.55	6.06	3.82
6 wells	10.35	8.37	6.12	-2.12	-20.37
3 wells	10.94	11.68	12.17	12.12	7.15
section ***bc***					
	0	±1%	±2%	±5%	±10%
12 wells	2.31	1.98	1.65	0.65	-1.03
6 wells	3.49	2.00	0.50	-4.05	-11.85
3 wells	9.23	9.57	9.89	10.68	11.50
section ***cd***					
	0	±1%	±2%	±5%	±10%
12 wells	0.67	0.52	0.39	0.11	0.04
6 wells	1.13	0.24	-0.57	-2.54	-4.60
3 wells	1.71	1.70	1.85	3.27	8.59
section ***da***					
	0	±1%	±2%	±5%	±10%
12 wells	0.11	-0.02	-0.15	-0.52	-1.13
6 wells	-1.84	-1.98	-2.11	-2.44	-2.96
3 wells	-1.81	-1.00	-0.01	4.00	13.79

MA analysis results show the uncertainty of 2.69, 30.72, 3.79 by rows; MA analysis results show the uncertainty of 4.43, 5.12, 6.05, 14.24, 27.52 by columns. The results based on rows reveal some fluctuation features, and a clearer increasing deviation results from column based uncertainty analysis. The results imply that lower data quantity has a chance to provide stable MA; data errors can worsen the MA uncertainty. Therefore, data quality will influence the stability of MA while data quantity is not directly correlated to MA uncertainty.

MP analysis results show the uncertainty of 17.48, 35.47, 26.01 by rows; MP analysis results show the uncertainty of 1.55, 1.67, 4, 6.64, 18.81 by columns. The resultant data shows some fluctuation on rows and increasing wider trend on columns. The results also imply that data quantity is not directly correlated to MP uncertainty although fewer data take more risk for poorer MP. From the columns, data quality influences MP even if the effect is relatively weaker. These results also reveal that within ±2% data corruption, the model exhibits a good robustness to data errors.

TABLE 5.12: MP analysis from inverted BCs based on two-dimensional experiment. Here, the two dimensions denote data quality (columns) and data quantity (rows). Tabulated inverted results are the maximum fluctuation range of resulting distributions at different sections of the entire boundary.

section ***ab***					
	0	±1%	±2%	±5%	±10%
12 wells	18.02	18.81	19.58	22.67	35.50
6 wells	19.09	18.84	21.52	29.31	54.31
3 wells	17.54	17.17	17.52	23.06	43.18
section ***bc***					
	0	±1%	±2%	±5%	±10%
12 wells	18.21	19.01	19.80	22.95	36.27
6 wells	19.06	18.91	21.64	34.70	66.89
3 wells	17.59	17.16	16.75	16.66	27.82
section ***cd***					
	0	±1%	±2%	±5%	±10%
12 wells	8.91	10.40	11.90	16.51	24.89
6 wells	10.10	11.53	16.15	31.07	60.93
3 wells	10.43	10.40	10.92	13.63	22.72
section ***da***					
	0	±1%	±2%	±5%	±10%
12 wells	7.72	7.33	7.21	9.73	16.48
6 wells	7.94	8.34	8.68	9.48	15.88
3 wells	17.96	16.42	15.89	17.97	28.63

Furthermore, the results provide some information on data quantity and data errors. First, good sampling strategy can support inverse model using limited data. Compared to 6 wells, the row for 3 wells exhibits milder fluctuation of the accuracy value, which implies that a sampling method plays an important role in inverse modeling. For MA, when the data error magnitude is increased to ±10%, the 3 well drilling strategy can offer more decent results; for MP, the results from 3 wells always are better than the model outcome by 6 wells. Both of these facts imply that the decrease of data quantity can strengthen the robustness of the model to data errors.

$\boldsymbol{b-c}$: Some distinct features are revealed by MA and MP analysis results. Generally, with deteriorated conditions, MA exhibits fluctuation and MP shows increasing lower trend. MA analysis results show 2.31, 2.00, 9.89; 1.98, 0.50, 10.68; 1.65, -4.05, 11.50 along the diagonals of the Table 5.11. From these facts, when the data quantity is less than 3 wells and data error is within ±5% of THV, the model exhibits little deterioration when conditions are worse, which indicates the model is robust to the condition change within this region. If data sets are reduced to 3 wells, MA is worse when the perturbation

on model is larger. When data error is increased to ±10% of THV, the fluctuation is exhibited by resultant data. MP analysis results show 18.21, 18.91, 16.75; 19.01, 18.91, 17.16; 19.80, 34.70, 27.82 along the diagonal of the Table 5.12. Here, the deterioration is not noticeable until the data error is sufficiently large, such as more than ±5% of THV. The 3-well based sampling strategy may provide a little better MP.

MA analysis results show the uncertainty of 3.34, 15.34, 2.27 by rows; MA analysis results show the uncertainty 6.92, 7.59, 9.39, 14.73, 23.35 by columns. The results based on rows reveal some fluctuation features, and a clearer increasing deviation results from column based uncertainty analysis. The results imply that lower data quantity will have a chance to provide stable model accuracy; the data error will worsen the model accuracy uncertainty. Therefore, data quality will influence the stability of model accuracy while data quantity is not directly correlated to model accuracy uncertainty.

MP analysis results show the uncertainty of 18.06, 47.98, 11.16 by rows; MP analysis results show the uncertainty of 1.47, 1.85, 4.89, 18.04, 39.07 by columns. The resultant data show relatively strong fluctuation on rows and increasing wider trend on columns. Here, the results indicate the uncertain effect of data quantity on inverting this section, which implies that it is possible to obtain decent inversion outcomes with fewer data. Also, MP is influenced by the data quality; larger data error can increase the width of uncertainty region, and especially, this effect is stronger when the corruption magnitude is larger than ±1%. Compared to the section $\boldsymbol{a}-\boldsymbol{b}$, the robustness of the inverse model is weaker on this section.

Furthermore, the results provide some extra information on data quantity and data errors. When the number of sampling wells is reduced to 3, the accuracy exhibit good robustness to the data corruption while the precision is not high, which is similar to the conclusion from the section $\boldsymbol{a}-\boldsymbol{b}$. For the precision, the robustness is more noticeable due to very narrow uncertainty region, especially when the worst result from ±10% error is removed. Both of these facts imply that the decrease of data quantity can strengthen the robustness of the model to data errors.

$\boldsymbol{c}-\boldsymbol{d}$: This section also has some distinctive features from MA and MP analysis results. Generally, with deteriorated conditions, MA shows fluctuation and MP exhibits increasing lower trend. MA analysis results show 0.67, 0.24, 1.85; 0.52, -0.57, 3.27; 0.39, -2.54, 8.59 along the diagonals of the Table 5.11. From the resultant data, MA exhibits larger oscillation which is better reflected by alternative signs. Accordingly, in general, worse conditions, such as fewer data and larger data error, can deteriorate MA but the trend is

fluctuated. Meanwhile, when the data error is less than ±5% of THV, the uncertainty of MA is very low, and the model is little disturbed by the condition perturbation, regardless of data quantity or data error. Hence, it is obtained that when the error magnitude is less than ±5%, the model behavior is robust to condition change. MP analysis results show 8.91, 11.53, 10.92; 10.40, 16.15, 13.63; 11.90, 31.07, 22.72 along the diagonal of the Table 5.12. The model precision here shows larger fluctuation than on the section $\boldsymbol{a}-\boldsymbol{b}$ or $\boldsymbol{b}-\boldsymbol{c}$. Deterioration still exists although it is a little concealed by some fluctuation trend. In addition, this fluctuation exhibits similar features to other model behaviors reflecting the information on sampled wells, and thus, the MP of inverting this section is possibly related to data quantity, especially data sampling strategy.

MA analysis results show the uncertainty of 0.63, 5.73, 6.88 by rows; MA analysis results show the uncertainty 1.04, 1.46, 2.42, 5.81, 13.19 by columns. Both of them show the clean increase of uncertainty which indicates the uncertainty of MA in this section behaves relatively stably. In addition, when the number of sampling wells is reduced to 6, the uncertainty region exhibits an increase leap, which implies that the data from more 6 wells can provide relatively robust MA behavior. Similarly, a robust behavior is performed when the data error magnitude is less than ±5%. MP analysis results show the uncertainty of 15.98, 50.83, 12.32 by rows; MP analysis results show the uncertainty of 1.52, 1.13, 5.23, 17.44, 38.21 by columns. The resultant data show relatively strong fluctuation on rows and increasing wider trend on columns. Here, the results manifest the uncertain effect of data quantity on inverting this section, which indicates that it is possible to obtain decent inversion outcomes with fewer data. Also, MP is influenced by the data quality; larger data error will increase the width of uncertainty region, and especially, this effect is stronger when the corruption magnitude is larger than ±1%. Compared to the section $\boldsymbol{a}-\boldsymbol{b}$, the robustness of the inverse model is weaker on this section.

Furthermore, the results provide some extra information on data quantity and data errors. When the number of sampled wells is reduced to 3, the accuracy exhibit good robustness to the data corruption while the precision is not high, which is similar to the conclusion from the section $\boldsymbol{a}-\boldsymbol{b}$. For the precision, the robustness is more noticeable due to very narrow uncertainty region, especially when the worst result from ±10% error is removed. Both of these facts imply that the decrease of data quantity can strengthen the robustness of the model to data errors.

$\boldsymbol{d}-\boldsymbol{a}$: The MA and MP analysis results show some distinct features. Generally, with deteriorated conditions, MA exhibits fluctuation and MP shows increasing lower trend.

MA analysis results show 0.11, -1.98, -0.01; -0.02, -2.11, 4; -0.15, -2.44, 13.79 along the diagonals of the Table 5.11. Here, the fluctuation is exhibited by alternative signs, and the general trend implies that worse condition can generate larger deviation from the true BCs. Meanwhile, when head data are corrupted by the error with less ±5% magnitude, MA shows a relatively good robustness to condition deterioration. MP analysis results show 7.72, 8.34, 15.89; 7.33, 8.68, 17.97; 7.21, 9.48, 28.63 along the diagonal of the Table 5.12. A relatively clear deterioration trend is obtained from the resultant MPs. While the condition is progressively worse, the uncertainty region of MP becomes wider. In particular, when the sampling wells are reduced to 3 wells, the region always shows a longer width.

MA analysis results show the uncertainty of 1.24, 1.12, 15.6 by rows; MA analysis results show the uncertainty 1.95, 1.96, 2.1, 6.44, 16.75 by columns. In general, data quantity has little influence on the accuracy uncertainty for this section unless the sampling wells are too limited, such as 3 wells. Data quality plays a relatively dominant role in MA fluctuation while the oscillation is mild when the data error is less than ±2% of THV.

MP analysis results show the uncertainty of 9.27, 7.94, 12.74 by rows; MP analysis results show the uncertainty of 10.24, 9.09, 8.68, 8.49, 12.75 by columns. The MP behavior on this section is slightly different from MA. The deterioration trend is weaken, especially for the increase of data errors, while the fluctuation is weaker which indicates a better robustness. Both of them demonstrate that the inverse model on this section is robust to the data quality perturbation or data quantity change. Also, when data error magnitude is extremely large, such as ±10%, or data quantity is too low, such as 3 wells, the MP behavior can be adversely affected.

From the resultant Table 5.11 and Table 5.12, some distinct information is also obtained. First, the data quantity need is not demanding for this section. Unlike the section of $\boldsymbol{a}-\boldsymbol{b}$ or $\boldsymbol{b}-\boldsymbol{c}$, the data quantity is a little influential to MA on this section. For MP, sufficient data, such as more than 3 wells, and the data with relatively less error, such as less than ±10% of THV, can support relatively decent inverted outcomes and stable inversion results.

5.3.2.4 Discussion on Data Quantity and Data Quality

Each factor has a stronger impact on different model state variable. Data quality determined the MA behavior and the uncertainty is little influenced by data quantity. This

outcome renders the prediction on model performance more feasible. In particular, within the region of some data error, the MA behavior will be stable; a leap deterioration takes place when data error exceed this region. Data quantity plays a prominent role in MP uncertainty during this experiment. Specifically, MP uncertainty is influenced by data quality when the error is too large. The analysis above reveals that data error should be control to a certain region to ensure the stable model performance.

Like the previous section, different characteristics of each BC section are also revealed by this co-effect experiment. The section $\boldsymbol{a}-\boldsymbol{b}$ is still robust to data error and data quantity from relative speed of model deterioration. Data corruption causes the largest fluctuation in this section also. The section $\boldsymbol{b}-\boldsymbol{c}$ and the section $\boldsymbol{c}-\boldsymbol{d}$ behave similarly in MP uncertainty. However, the section $\boldsymbol{b}-\boldsymbol{c}$ possesses larger uncertainty in MA than the section $\boldsymbol{c}-\boldsymbol{d}$. The section $\boldsymbol{d}-\boldsymbol{a}$ has a similar MA uncertainty behavior to the section $\boldsymbol{cd}$. Compared to the section $\boldsymbol{d}-\boldsymbol{a}$, MP is more stable for the section $\boldsymbol{c}-\boldsymbol{d}$. With respect to accurate inverted results, the section $\boldsymbol{c}-\boldsymbol{d}$ and the section $\boldsymbol{d}-\boldsymbol{a}$ are insensitive to data corruption if the data error is not outrageous. The section $\boldsymbol{d}-\boldsymbol{a}$ has most stable behavior in MP uncertainty in terms of data quantity. Generally, extrapolation regions will yield the larger MA uncertainty region and mild MP fluctuation. Also, reducing data quantity can generate the increasingly biased recovered results and uncertainty region can be wider for each piece of the boundary line. Data errors can mildly affect MA, except when the error magnitude is increased to $\pm 10\%$, while MP is little influenced by this factor. Finally, the data quality and data quantity could be balanced. Proper data errors can improve the results from lower data quantity.

5.3.3 Data Quality and Resolution

5.3.3.1 Experimental Conditions

The third experiment is to examine the co-effect of data quantity and data quality on the inverted Ks and BCs. The condition of this experiment is set as decreased heterogeneity resolution, i.e., SIS grids, SA grids, and Coarsening grids, and the increasing data error, i.e., $\pm 1\%$, $\pm 2\%$, $\pm 5\%$, and $\pm 10\%$, based on THV. The different grids are generated by the same data sets and SIS simulation results are modified by SA and Coarsening. Here, 12 sampling wells are chosen to generate observed data. The data errors, of which the magnitude is based on THV, are added to observed hydraulic heads. Under these conditions, several experiments are conducted and experimental results are illustrated

by Figure 5.24, Figure 5.25, Figure 5.26, Figure 5.27, Figure 5.28, Figure 5.29, and Figure 5.30.

5.3.3.2 K, MA, and MP

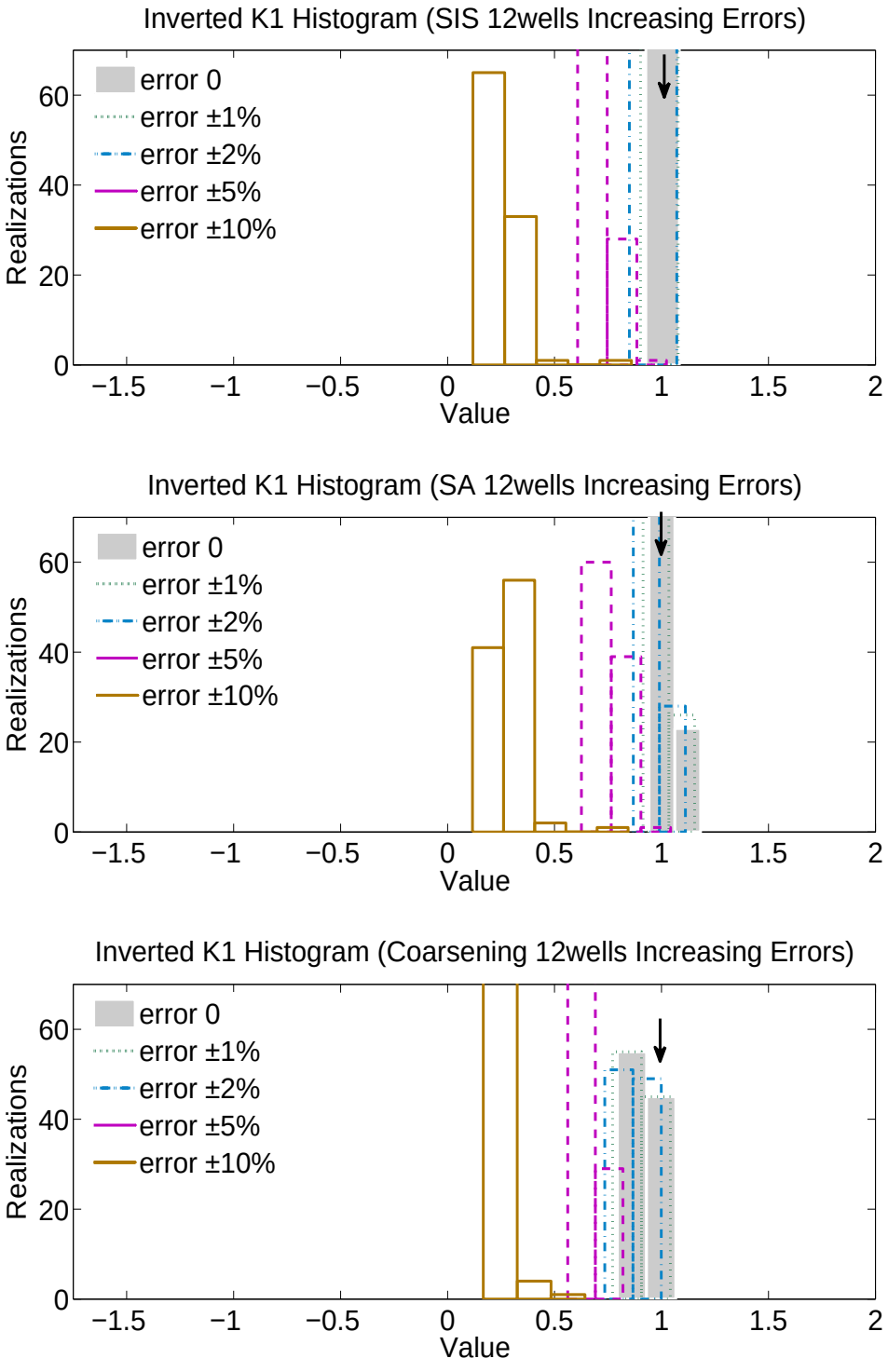

FIGURE 5.24: K_1 uncertainty analysis based on data quality and heterogeneity resolution. The arrows point to the true values. The realizations denote the frequency within different value range which reflects uncertainty regions.

TABLE 5.13: MA analysis from inverted K_1 based on two-dimensional experiment. The two dimensions are heterogeneity resolution (rows) and data quality(columns). The value in each cell denotes the center line of different resultant distributions generated under the correspondent condition.

DQl / HR	0	±1%	±2%	±5%	±10%
SIS	1	0.97	0.93	0.71	0.24
SA	1.03	1.00	0.96	0.74	0.27
Coarsening	0.92	0.91	0.86	0.67	0.26

TABLE 5.14: MP analysis from inverted K_1 based on two-dimensional experiment. The two dimensions are data quantity (rows) and data quality(columns). The value in each cell denotes the length of the resultant uncertainty region generated under the correspondent condition.

DQl / HR	0	±1%	±2%	±5%	±10%
SIS	0.15	0.17	0.19	0.26	0.29
SA	0.24	0.24	0.24	0.26	0.31
Coarsening	0.24	0.27	0.26	0.26	0.17

TABLE 5.15: MA analysis from inverted K_2 based on two-dimensional experiment. The two dimensions are heterogeneity resolution (rows) and data quality(columns). The value in each cell denotes the center line of different resultant distributions generated under the correspondent condition.

DQl / HR	0	±1%	±2%	±5%	±10%
SIS	9.97	9.87	9.71	8.97	7.26
SA	9.98	9.87	9.71	8.92	7.18
Coarsening	9.61	9.51	9.35	8.59	6.93

MA results show 1, 1, 0.86; 0.97, 0.96, 0.67; 0.93, 0.74, 0.26 for K_1 along the diagonal of the Table 5.13 and 9.97, 9.87, 9.35; 9.87, 9.71, 8.59; 9.71, 8.92, 6.93 for K_2 along the diagonal of the Table 5.15. The resultant data show some mild deterioration trend which is more related to heterogeneity resolution. In general, MA exhibits good stability unless the data error is too large.

MP results show 0.15, 0.24, 0.26; 0.17, 0.24, 0.26; 0.19, 0.26, 0.17 for K_1 along the diagonal of the Table 5.14 and 0.46, 0.65, 0.81; 0.58, 0.89, 0.65; 0.61, 0.95, 0.81 for K_2 along the diagonal of the Table 5.16. MP exhibits some fluctuation while the general trend shows worse data conditions resulting in slightly lower precision. However, the precision is relatively stable under different conditions and the inverse model possesses decent precision all the time.

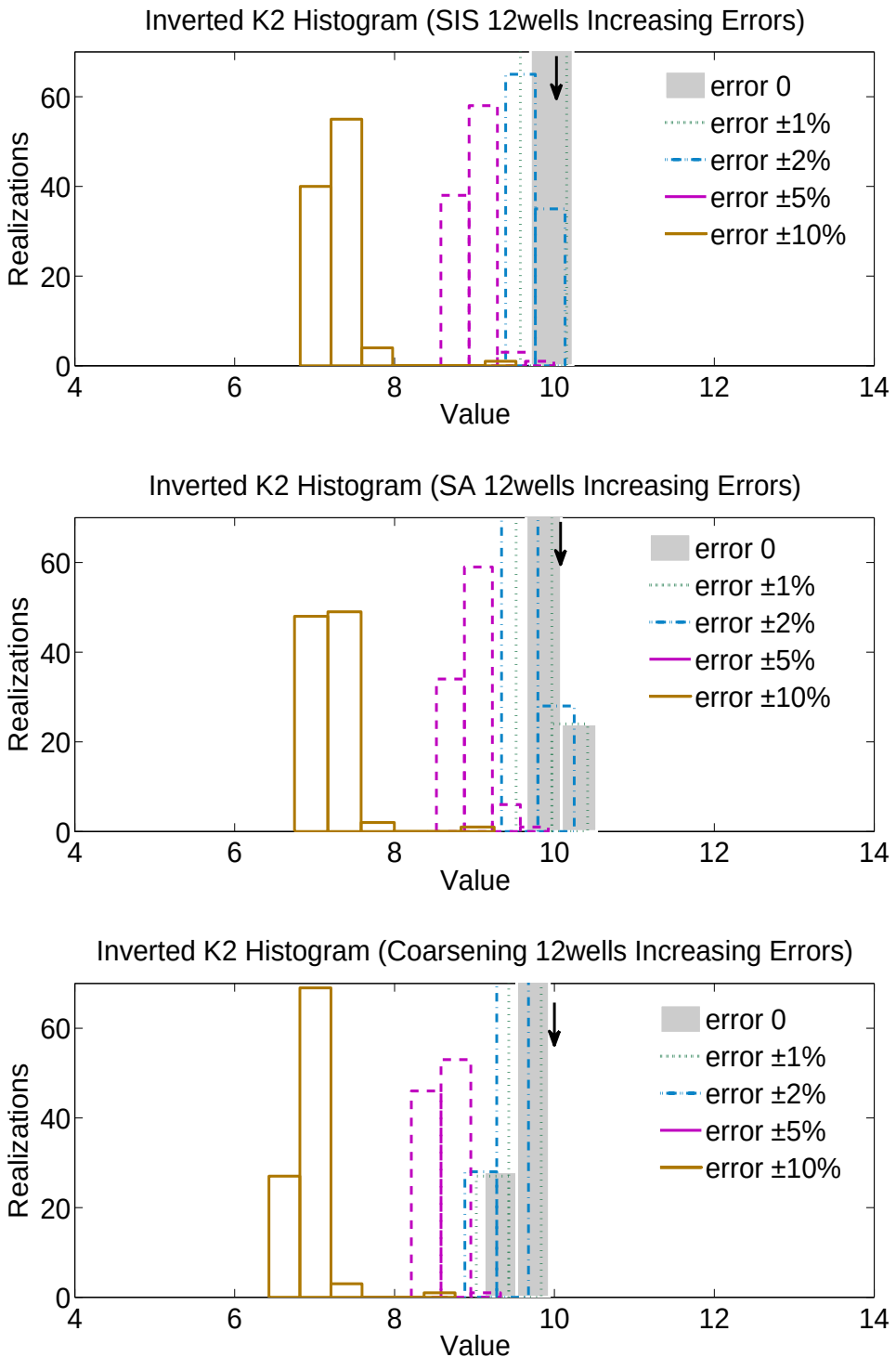

FIGURE 5.25: K_2 uncertainty analysis based on data quality and heterogeneity resolution. The arrows point to the true values. The realizations denote the frequency within different value range which reflects uncertainty regions.

TABLE 5.16: MP analysis from inverted K_2 based on two-dimensional experiment. The two dimensions are data quantity (rows) and data quality(columns). The value in each cell denotes the length of the resultant uncertainty region generated under the correspondent condition.

DQl / HR	0	±1%	±2%	±5%	±10%
SIS	0.46	0.58	0.61	0.89	0.98
SA	0.66	0.65	0.89	0.95	0.99
Coarsening	0.73	0.81	0.81	0.65	0.81

MA analysis results show the uncertainty of 0.76, 0.76, 0.66 for K_1 and 2.71, 2.80, 2.68 for K_2 by rows; MA analysis results show the uncertainty of 0.11, 0.09, 0.1, 0.07, 0.03 for K_1 and 0.37, 0.36, 0.36, 0.38, 0.33 for K_2 by columns. Data error and heterogeneity resolution both have little impact on the accuracy uncertainty. From the uncertainty region length, heterogeneity resolution presumably influences the model more than data quality, and inverse model shows accuracy uncertainty robustness to data errors.

MP analysis results show the uncertainty of 0.14, 0.07, 0.1 for K_1 and 0.52, 0.34, 0.08 for K_2 by rows; MP analysis results show the uncertainty of 0.09, 0.1, 0.07, 0, 0.16 for K_1 and 0.27, 0.23, 0.28, 0.30, 0.18 for K_2 by columns. Similar to the findings from MA uncertainty, the analysis results reveal that data error and heterogeneity resolution have limited influence on MP uncertainty behavior. Here, these two factors show some equal impact on the model.

From the analysis above, the relation between data quality and heterogeneity resolution is better understood. First, data quality determines MA. When the data error increases, the MA deterioration is more severe. Within a certain error range, such as less than ±2% of THV, relatively good MA can be preserved. Next, heterogeneity resolution influences MP. Generally speaking, lower resolution can generate poorer precision. Meanwhile, these two factors can be used to balance model deterioration by each of them. Limited data errors can recover the loss from resolution reduction and lower resolution helps model to be robust to data errors. Last but not least, MA and MP uncertainties both exhibit good stability when data are corrupted and resolution is smoothen, which indicates that it is possible to predict the model behavior using the knowledge of current status and change trend.

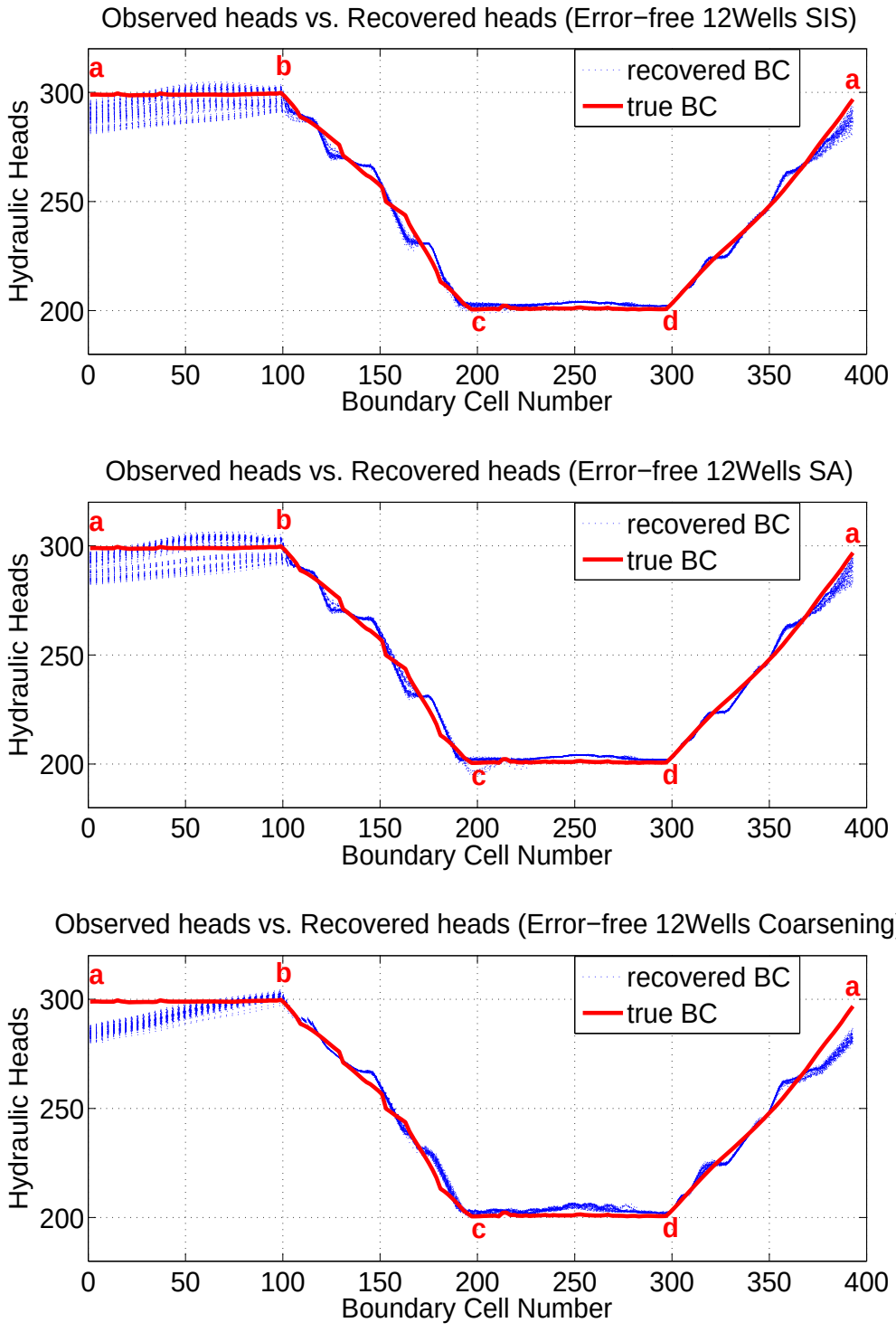

FIGURE 5.26: *BCs* uncertainty analysis based on different resolutions and error-free data. The letters of alphabet denote the boundary locations. Hydraulic heads are recovered conditions and boundary cell number is the index of each boundary cell.

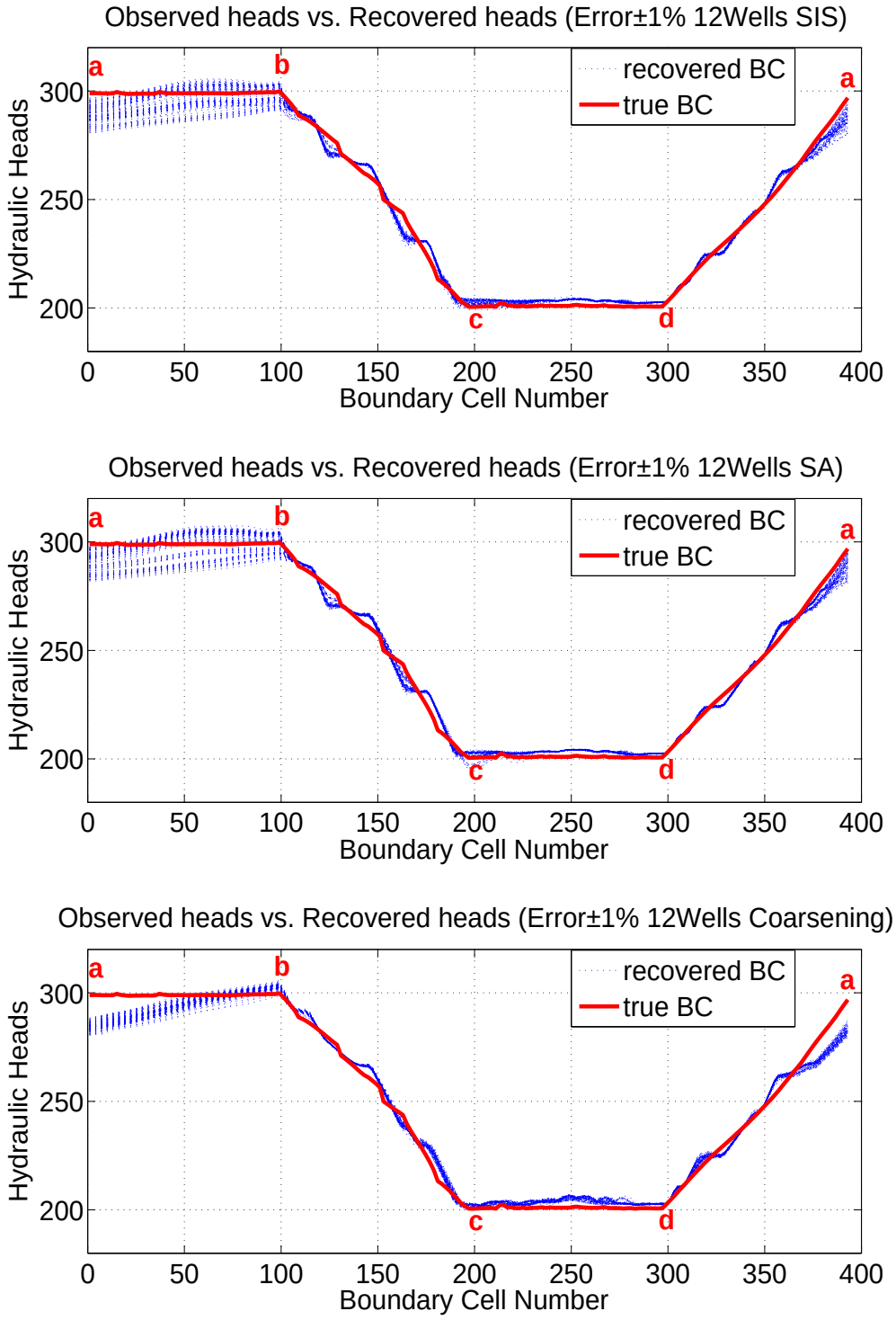

FIGURE 5.27: *BCs* uncertainty analysis based on different resolutions and data with the ±1% error of THV. The letters of alphabet denote the boundary locations. Hydraulic heads are recovered conditions and boundary cell number is the index of each boundary cell.

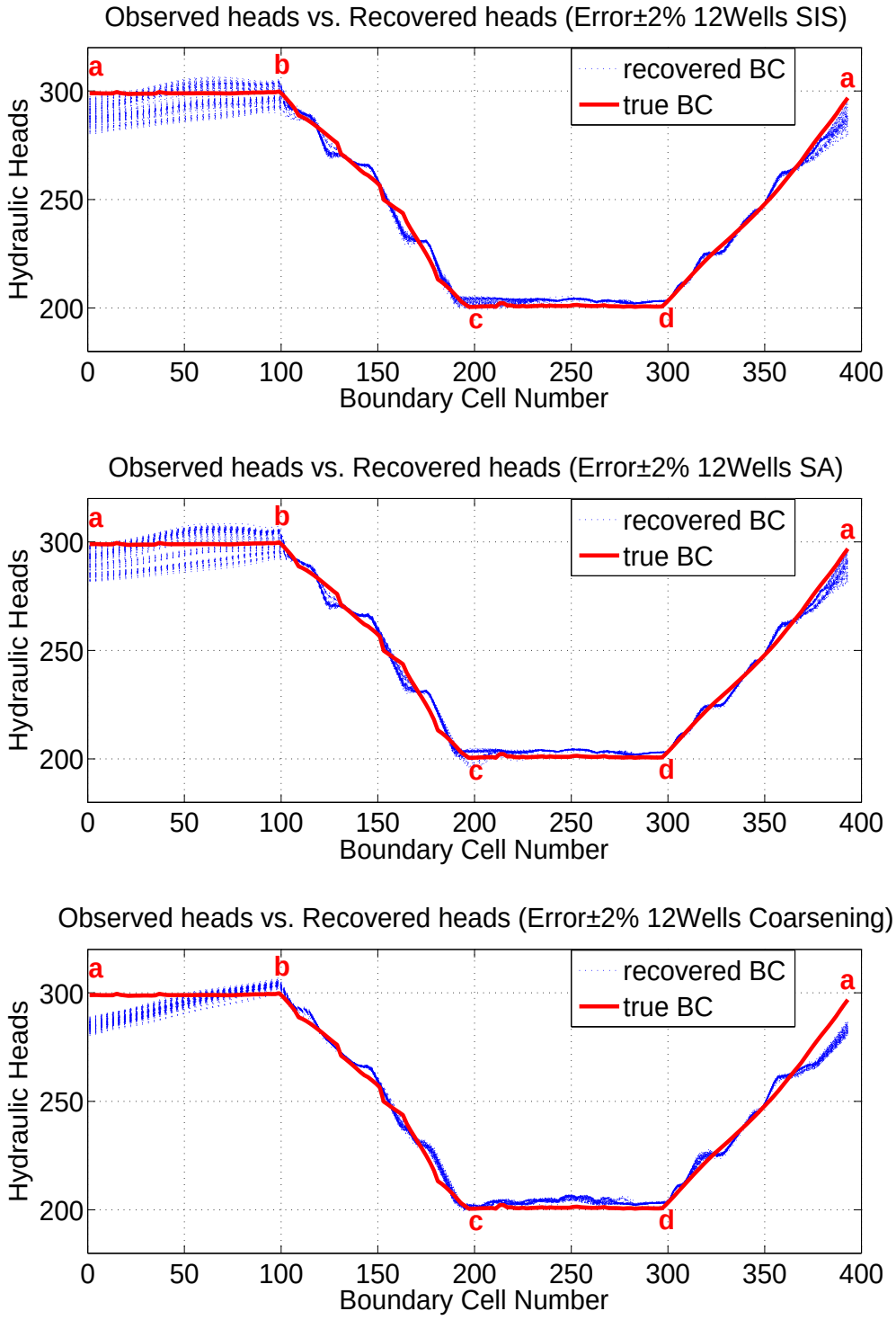

FIGURE 5.28: *BCs* uncertainty analysis based on different resolutions and data with the ±2% error of THV. The letters of alphabet denote the boundary locations. Hydraulic heads are recovered conditions and boundary cell number is the index of each boundary cell.

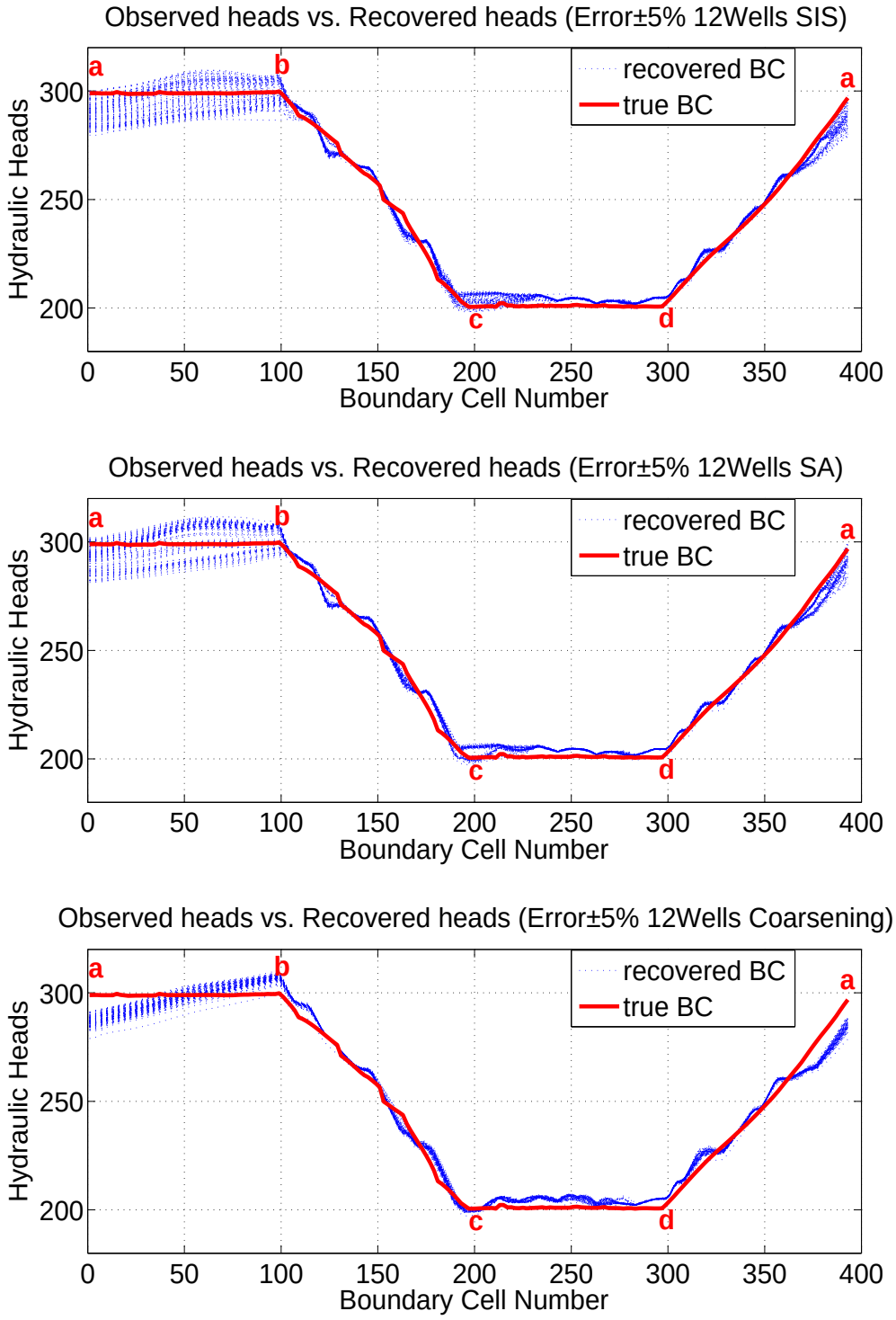

FIGURE 5.29: *BCs* uncertainty analysis based on different resolutions and data with the ±5% error of THV. The letters of alphabet denote the boundary locations. Hydraulic heads are recovered conditions and boundary cell number is the index of each boundary cell.

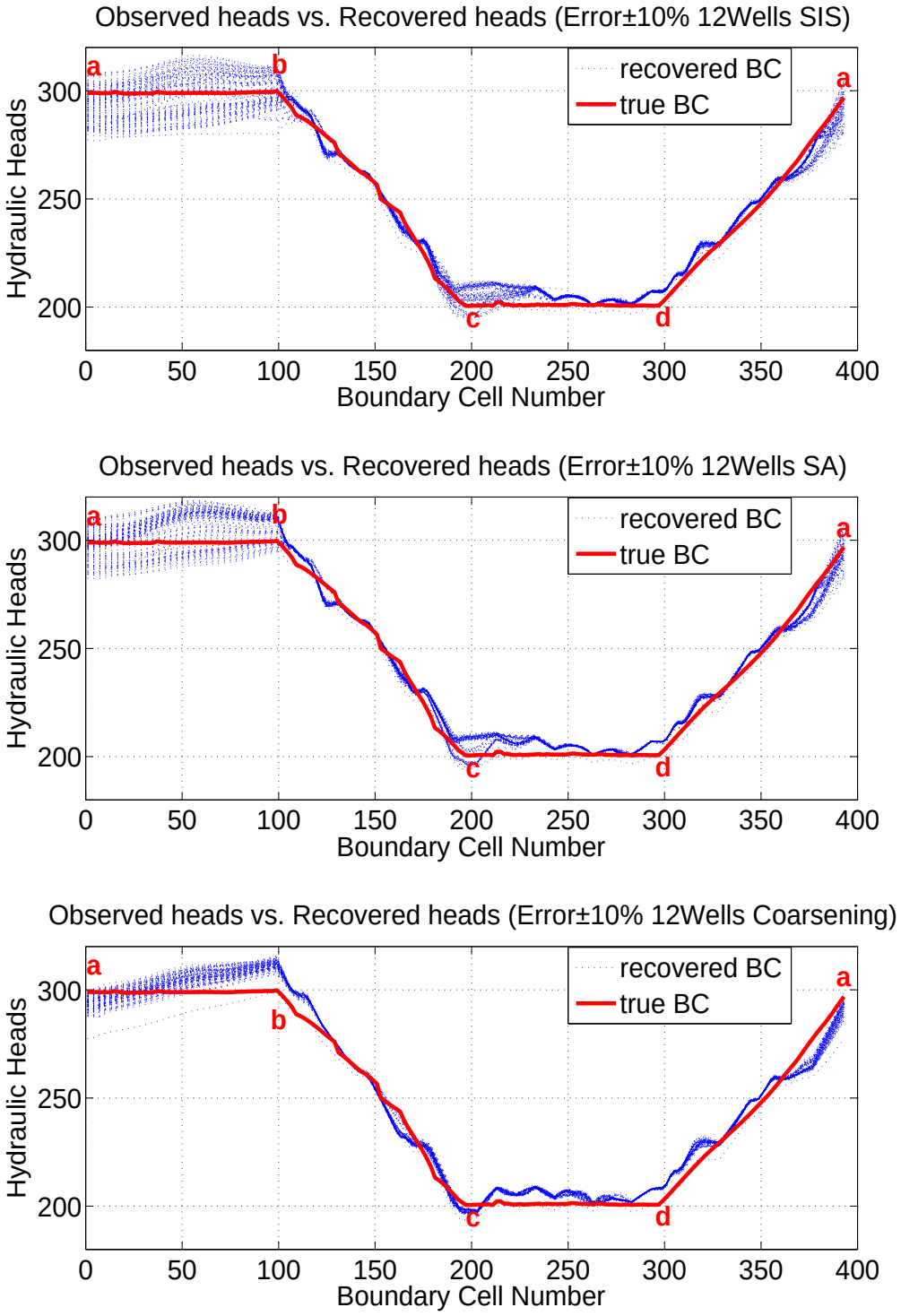

FIGURE 5.30: *BCs* uncertainty analysis based on different resolutions and data with the ±10% error of THV. The letters of alphabet denote the boundary locations. Hydraulic heads are recovered conditions and boundary cell number is the index of each boundary cell.

TABLE 5.17: MA analysis from inverted BCs based on two-dimensional experiment. Here, the two dimensions are data quality (columns) and heterogeneity resolution (rows). Tabulated inverted results are the deviations of resulting distributions from the true conditions at different sections of the entire boundary.

section ***ab***					
	0	±1%	±2%	±5%	±10%
SIS	6.51	6.56	6.55	6.06	3.82
SA	4.88	4.55	4.14	2.41	-2.11
Coarsening	10.17	9.70	9.11	6.60	-0.03
section ***bc***					
	0	±1%	±2%	±5%	±10%
SIS	2.31	1.98	1.65	0.65	-1.03
SA	0.21	-0.54	-1.29	-3.60	-7.57
Coarsening	0.88	-0.02	-0.94	-3.81	-8.92
section ***cd***					
	0	±1%	±2%	±5%	±10%
SIS	0.67	0.52	0.39	0.11	0.04
SA	0.33	0.15	-0.01	-0.38	-0.60
Coarsening	-1.20	-1.57	-1.92	-2.84	-3.94
section ***da***					
	0	±1%	±2%	±5%	±10%
SIS	0.11	-0.02	-0.15	-0.52	-1.13
SA	-0.45	-0.60	-0.75	-1.17	-1.80
Coarsening	-1.93	-1.61	-1.27	-0.25	1.53

5.3.3.3 BC, MA, and MP

The BC analysis structure, based on four sections including $\boldsymbol{a}-\boldsymbol{b}$, $\boldsymbol{b}-\boldsymbol{c}$, $\boldsymbol{c}-\boldsymbol{d}$, and $\boldsymbol{d}-\boldsymbol{a}$, is also followed here.

$\boldsymbol{a}-\boldsymbol{b}$: The MA and MP analysis results reveal some distinct features. Generally, with deteriorated conditions, MA exhibits fluctuation and MP shows increasing lower trend. MA analysis results show 6.51, 4.55, 9.11; 6.56, 4.14, 6.60; 6.55, 2.41, -0.03 along the diagonals of the Table 5.17. In general, the accuracy indicates model behaviors are more robust here since the fluctuation is relatively mild. Also, these data reveal that model deterioration is more uncertain, and it is possible that data with large error, such as ±10% of THV, and relatively low resolution, such as Coarsening grids, can provide decent MA, such as the deviation of -0.03. MP analysis results show 18.02, 20.15, 9.51; 18.81, 21.10, 13.23; 19.58, 24.22, 22.86 along the diagonal of the Table 5.18. MP exhibits model improvement by Coarsening grids on data corruption. The compensation

TABLE 5.18: MP analysis from inverted BCs based on two-dimensional experiment. MP analysis from inverted BCs based on two-dimensional experiment. Here, the two dimensions denote data quality (columns) and heterogeneity resoluiton (rows). Listed inverted Ks are the maximum fluctuation range of resulting distributions.

section ***ab***					
	0	±1%	±2%	±5%	±10%
SIS	18.02	18.81	19.58	22.67	35.50
SA	19.19	20.15	21.10	24.22	30.37
Coarsening	9.71	9.50	9.51	13.23	22.86
section ***bc***					
	0	±1%	±2%	±5%	±10%
SIS	18.21	19.01	19.80	22.95	36.27
SA	19.48	20.49	21.48	24.35	30.38
Coarsening	9.50	9.33	9.31	12.94	21.69
section ***cd***					
	0	±1%	±2%	±5%	±10%
SIS	8.91	10.40	11.90	16.51	24.89
SA	9.16	9.62	10.07	11.35	13.24
Coarsening	5.67	5.67	5.93	9.43	14.88
section ***da***					
	0	±1%	±2%	±5%	±10%
SIS	7.72	7.33	7.21	9.73	16.48
SA	8.74	8.74	8.71	9.29	15.86
Coarsening	6.69	6.68	6.67	7.48	9.85

relation between heterogeneity and data quality is more discernable here although SA grids induce limited bias compared to the results from SIS grids.

MA analysis results show the uncertainty of 2.74, 6.99, 10.20 by rows; MA analysis results show the uncertainty of 5.29, 5.15, 4.97, 4.19, 5.93 by columns. From the uncertainty data, the MA stability is progressively worse with the lower heterogeneity resolution. Concerning data quality, MA shows strong robustness of uncertainty to data errors in that the length of uncertainty region is basically similar.

MP analysis results show the uncertainty of 17.48, 10.46, 13.15 by rows; MP analysis results show the uncertainty of 9.48, 10.65, 11.59, 10.99, 12.64 by columns. The resultant data shows relatively mild fluctuation by rows and columns. The results imply that the change of heterogeneity resolution has little impact on MP stability. In particular, the resultant precision uncertainty remains a very stable width, which indicates that MP deterioration by aggravated data corruption is able to be cured by heterogeneity resolution modification.

Furthermore, some other valuable model behaviors on data quality and heterogeneity resolution are provided. First, grid modification yields some mildly instable model outcomes. Since our medication methods exhibits some randomness and limited conditioning scheme, upscaling may cause occasional change in model behavior. This fact manifests that upscaling strategy is crucial for inverse modeling and a smart upscaling scheme can preserve good stability of model outcomes, even improve the model robustness. Next, the possibility of compensation between data quality and heterogeneity resolution reveals that they presumably have equal impact on model behavior. This revelation implies that there is a possibility to heal data corruption using upscaling strategy, which involves error correctness modeling.

$\boldsymbol{b-c}$: Concerning the primary model behavior, the section $\boldsymbol{b-c}$ is similar to the section $\boldsymbol{a-b}$ in MP, and a little different from the section $\boldsymbol{a-b}$ in MA. MA analysis results show 2.31, -0.54, -0.94; 1.98, -1.29, -3.81; 1.65, -3.60, -8.92 along the diagonals of the Table 5.17. In general, the MA behavior is fluctuated when parameters are both worsen. When the data errors are extremely large, model deterioration will appear and be severe. MP analysis results show 18.21, 20.49, 9.31; 19.01, 21.48, 12.94; 19.80, 24.35, 21.69 along the diagonal of the Table 5.18. Compared to MA, the MP fluctuation is more discernable when both conditions are increasingly worse. Especially, Coarsening grid offers significant MP improvement which is similar to the case for the section $\boldsymbol{a-b}$.

MA analysis results show the uncertainty of 3.34, 7.78, 9.80 by rows; MA analysis results show the uncertainty of 2.1, 2.52, 2.94, 4.46, 7.89 by columns. MA uncertainty region is increasingly wider when data errors increase or resolution is lower. In particular, the MA uncertainty reveals good model robustness when the data error magnitude is less than $\pm 2\%$. Also, there is no big difference between SIS grids and Coarsening grids in accuracy uncertainty. MP analysis results show the uncertainty of 18.06, 10.90, 12.19 by rows; MP analysis results show the uncertainty of 9.98, 11.16, 12.17, 11.41, 14.58 by columns. The fluctuation behavior is preserved for both of the uncertainty experiments. Compared to data error, heterogeneity resolution exhibits relatively stronger fluctuation on precision uncertainty. From this fact, it is implied that heterogeneity resolution may have stronger impact on MP stability than data quality.

From the analysis above, some useful model strategies are informed. Upscaling is a good technique to heal the data corruption while a grid modification requires a clever scheme. This model alleviation performs well when data errors are not high, such as more than $\pm 5\%$ of THV. Data errors also have a potential to balance the loss of MA

from resolution reduction. Both of these factors may have equal impact on model and possibly compensate for the error by each other.

c*−*d: MA analysis results show 0.67, 0.15, -1.92; 0.52, -0.01, -2.84; 0.39, -0.38, -3.94 along the diagonals of the Table 5.17. The model accuracy shows a very decent robustness to the condition perturbation. Although some fluctuation and slight deterioration still exist, the resultant MAs are basically steady and close to the true conditions. MP analysis results show 8.91, 9.62, 5.93; 10.40, 10.07, 9.43; 11.90, 11.35, 14.88 along the diagonal of the Table 5.18. The change of MP is relatively mild also, especially if the two extreme results, i.e., 5.93 and 14.88, are removed.

MA analysis results show the uncertainty of 0.71, 0.93, 2.74 by rows; MA analysis results show the uncertainty of 1.87, 2.09, 2.31, 2.95, 3.98 by columns. The MA uncertainty analysis also proves the robustness of the inverse model on this section. If the results from some worst cases, such as Coarsening grids and ±10% data errors, are taken out, the fluctuation magnitude of the rest data is less than 0.5% of THV. MP analysis results show the uncertainty of 15.98, 4.08, 9.21 by rows; MP analysis results show the uncertainty of 3.49, 4.73, 5.97, 7.08, 11.65 by columns. The MP uncertainty becomes mildly larger when data error increases. Grid modification has uncertain impact on the precision uncertainty in this section.

The analyses above show some distinct features of inverse model on the section ***c*−*d***. The model behaves robustly, regardless of under data corruption or heterogeneity resolution upscaling. Especially, proper upscaling plus relatively lower data errors can result in decent model performance. Hence, the inverse model provides the outcomes with higher confidence on this section.

$\boldsymbol{d} - \boldsymbol{a}$: MA analysis results show 0.11, -0.60, -1.27; -0.02, -0.75, -0.25; -0.15, -1.17, 1.53 along the diagonals of the Table 5.17. MA becomes much more stable. Even when the perturbation is very large, such as Coarsening grid and ±10% error, the model still performs very well on accuracy. MP analysis results show 7.72, 8.74, 6.67; 7.33, 8.71, 7.48; 7.21, 9.29, 9.85 along the diagonal of the Table 5.18. Although the results from precision is not as impressive as from MA, the data still exhibits little fluctuation and relatively high precision. Based on the resultant data, the mild oscillation shows some closer correlation with heterogeneity resolution.

MA analysis results show the uncertainty of 1.24, 2.25, 3.46 by rows; MA analysis results show the uncertainty of 2.04, 1.59, 1.12, 0.92, 3.33 by columns. In general, the MA uncertainty exhibits stable results and validates the model robustness. From specific

perspective, the MA uncertainty reveals some correlation trend more with heterogeneity resolution than data quality, expect when the data error is extremely high, such as larger than ±10% of THV.

MP analysis results show the uncertainty of 9.78, 7.12, 3.18 by rows; MP analysis results show the uncertainty of 2.05, 2.06, 2.04, 2.25, 6.63 by columns. The data errors have much weaker impact on the MP uncertainty, especially when the some extreme case, such as ±10% error, is removed. The uncertainty exhibits the width less than 0.2% of THV when data error is not more than ±5%. In addition, the precision uncertainty is improved when the grid heterogeneity resolution is lower. This fact also implies that grid heterogeneity has relatively strong impact on the inverse model in terms of the section $\boldsymbol{d}-\boldsymbol{a}$.

The robustness revealed by the analysis above informs us some useful sampling strategy for this region. Data error corruption has very limited impact on model quality, so the sampling strategy along this region is not demanding. Also, heterogeneity resolution has potentials to heal the data corruption even if some clever upscaling scheme is required. The results above also demonstrate that proposed inverse model is most effective to similar regions to the section $\boldsymbol{d}-\boldsymbol{a}$ due to its robustness to data error and heterogeneity resolution.

5.3.3.4 Discussion on Data Quality and Heterogeneity Resolution

Some distinct relation between data quality and heterogeneity resolution are detected. From inverted Ks, heterogeneity resolution has less influence on model deterioration by data quality than data quantity. Therefore, the dominant role of data quality in MA is more discernable. However, the model deterioration resulting from data corruption is relieved by heterogeneity smoothing. MP also exhibits relatively stable status. These facts manifest that model status prediction is much easier when the input parameters are data quality and heterogeneity resolution.

Different features are also exhibited by each section of BC in this experiment. The section $\boldsymbol{a}-\boldsymbol{b}$ is more robust to data error than to heterogeneity resolution. The MP uncertainty also reveals this characteristic. The section $\boldsymbol{a}-\boldsymbol{b}$ and the section $\boldsymbol{b}-\boldsymbol{c}$ behave similarly in MP uncertainty. For MA, the section $\boldsymbol{b}-\boldsymbol{c}$, the section $\boldsymbol{c}-\boldsymbol{d}$, and the section $\boldsymbol{d}-\boldsymbol{a}$ show similar trends in uncertainty results. Concerning relative sensitivity, the section $\boldsymbol{b}-\boldsymbol{c}$ is highest to condition changes, the section $\boldsymbol{d}-\boldsymbol{a}$ is lower, and the section $\boldsymbol{c}-\boldsymbol{d}$

is lowest. Unlike the section $\boldsymbol{a} - \boldsymbol{b}$, these three sections indicate that data quality and heterogeneity resolution have equal impact on the BC inversion accuracy. Regarding MP, the section $\boldsymbol{d} - \boldsymbol{a}$ exhibits more stable and higher precision, which implies the precision on this section is robust to data error or heterogeneity upscaling. Generally, extrapolation areas show stable precision and robustness to data errors. Heterogeneity resolution usually has limited influence on each section except extrapolation regions. Data quality still determines model accuracy and relative smaller data errors do not cause severe model deterioration. Larger data corruption can lead to unstable model behavior which is reflected by leap change in related uncertainty. Therefore, data errors should be still limited to ensure model quality.

Chapter 6

Conclusions

This research reveals the model quality under different conditions using uncertainty analysis. To reach this goal, model reliability to the real problem has been tested and computation performance is much improved. For model reliability testing, forward modeling is conducted to build a synthetic confined aquifer with specific boundary conditions. Within the synthetic aquifer, well drilling is conducted to sample observed hydraulic heads, fluxes and hydraulic conductivities. Based on different data sets, dynamic data integration and static data integration are both adopted to assimilate these data. Static data integration employed Sequential Indicator Simulation (Variogram-based Geostatistics) to assess the hydraulic conductivity distribution patterns and dynamic data integration is conducted using the physically-based inverse method proposed by Irsa and Zhang (2012). The inverted results are evaluated by examining the inverted Ks and recovered BCs. From the inverted result distribution, inverted Ks are centered at the true value with decent uncertainty region; recovered BCs are spread over the true condition and uncertainty region is narrow. Both of these facts indicate the physically based inverse model is reliable to practical problems. The success of the data integration breaks through the limitation from data quantity and renders it possible to solve large scale aquifer inversion using the inverse approach.

Computation performance is also much improved from respects of serial solver and parallel computing. The proposed method yields a linear equation system solved by LSQR solver and exhibiting severe ill-condition which slows down the convergence of this iterative solver. Therefore, CN is mainly discussed to explore the condition improvement schemes. The related research is categorized into induced problem improvement and inherent problem improvement. In terms of induced problem, coordinate transform and

equation scaling are adopted to ameliorate ill-condition; concerning inherent problem, Gaussian Noise Perturbation is employed to reduce the condition number of large coefficient matrix, thus improving the condition. After these techniques, the computation time is reduced by order of magnitude and a 200×200 problem can be correctly solved in 1 hour. These serial solver improvements have made it possible to conduct large scale stochastic inversion efficiently in PC. Also, some precision and accuracy reduction should be noticed by users.

Next, parallel solver is developed to further improve this performance. A scalability study is conducted to explore a scalable solver which is independent from the number of processors and problem sizes. To take full advantage of this solver, the coefficient matrix produced by proposed method is reorganized to a diagonal sparse matrix and random entry based matrix using permutation. After this operation, this scalable solver is sped up due to diagonal features in the matrix. Using 100 processors, a 500×500 problem can be solved in 2 minutes based on CPU time. This parallel study helps the inverse model to behave more efficiently and the users who possess parallel computers can apply this model to more complex and larger problems.

After the testing and improvements, uncertainty analysis becomes feasible. This research conducted the uncertainty analysis to examine three factors, including data quantity, data quality, and heterogeneity resolution. Different factors play different roles in inverse model quality. From the corresponding results, data quantity plays more important role in model precision; data quality determines the model accuracy; heterogeneity resolution has least influence on model reliability. Considering co-effect analysis results, heterogeneity resolution is overshadowed by data quality and data quantity; the roles of data quality and data quantity are enhanced when both of them are tested simultaneously. Hence, it is concluded that higher model precision requires more observed data, better model accuracy demands lower data errors, and heterogeneity resolution could be traded for better computation performance. According to different the requirements, different model strategies needs to be conducted when this physically-based inverse method.

Future work can be extended to many sources based on the current analysis results. First, sensitivity analysis a crucial topic to explore. Data quantity analysis result reveals the relatively high instability to model input, and as a matter of fact, this model behavior results from spatial information input amount. With the drastic decrease of data quantity, total information will be reduced undoubtedly; however, the mild decrease does not determine poor inversion outcome because spatial location possesses different amounts of information. Sensitivity analysis is capable of revealing this knowledge

and thus, the sampling strategy will be optimized using data sampling at the location with higher spatial information. The common sensitivity analysis methods include local methods and global methods, such as One-at-a-time (OAT) Method and Sobol Method. Next, more factors can be examined using DoE approach. Here, only three factors are tested by two dimensional DoE, however, the influential factors are much more than three and high dimensional DoE is required for a decent uncertainty analysis on a real large problem. In addition, fractured aquifers should be tested for this inversion method. In a real world, geological formations usually possess some fractures which changes the regular permeability distribution pattern. This structural alteration brings more challenges for flow pattern assessment, and thus, accurate parameter estimation on fractured aquifers becomes increasingly important topic. Finally, three dimensional stochastic inversion and transient flow can be further researched. After these further explorations, the new physically based inversion method will be sound and in use to solve more real problems.

Bibliography

[1] Juraj Irsa and Ye Zhang. A Direct Method of Parameter Estimation for Steady State Flow in Heterogeneous Aquifers with Unknown Boundary Conditions. *Water Resour. Res.*, 48:W09526, 2012. doi: 10.1029/2011WR011756.

[2] Richard L. Chambers, Jeffrey M. Yarus, and Kirk B. Hird. Petroleum Geostatistics for Nongeostatisticians. *The Leading Edge*, 19(5):474–479, 2000. doi: 10.1190/1.1438630.

[3] He Huang, John M. Dennis, Liqiang Wang, and Po Chen. A Scalable Parallel LSQR Algorithm for Solving Large-Scale Linear System for Tomographic Problems: A Case Study in Seismic Tomography. *the 2013 International Conference on Computational Science (ICCS)(main track)*, 2013.

[4] W. W.-G. Yeh. Review of Parameter Identification Procedures in Groundwater Hydrology: The Inverse Problem. *Water Resour. Res.*, 22(2):95–108, 1986. doi: 10.1029/WR022i002p00095.

[5] T. R. Ginn and J. H. Cushman. Inverse Methods for Subsurface Flow: A Critical Review of Stochastic Techniques. *Stochastic Hydrol. Hydraul.*, 4(1):1–26, 1990. doi: 10.1007/BF01547729.

[6] D. McLaughlin and L. R. Townley. A Reassessment of the Groundwater Inverse Problem. *Water Resour. Res.*, 32(5):11311161, 1996. doi: 10.1029/96WR00160.

[7] G. de Marsily, J.P. Delhomme, and A.M. Lavenue. Four Decades of Inverse Problems in Hydrogeology. *Spec. Pap. Geol. Soc. Am.*, 348:117, 2000.

[8] J. Carrera, A. Alcolea, A. Medina, J. Hidalgo, and L. Slooten. Inverse Problem in Hydrogeology. *Hydrogeol. J.*, 13:206222, 2005. doi: 10.1007/s10040-004-0404-7.

[9] J. A. Vrugt, P. H. Stauffer, T. Wohling, B. A. Robinson, and V. V. Vesselinov. Inverse Modeling of Subsurface Flow and Transport Properties: A Review with New Developments. *Vadose Zone J.*, 7:843864, 2008a. doi: 10.2136/vzj2007.0078.

[10] M. C. Hill and C. R. Tiedeman. *Effective Groundwater Model Calibration: With Analysis of Data, Sensitivities, Predictions, and Uncertainty.* Wiley-Interscience, Hoboken, N. J., 2007.

[11] R. L. Cooley. Incorporation of Prior Information on Parameters into Nonlinear Regression of Groundwater Flow Models: 1. Theory. *Water Resour. Res.*, 18(4): 965976, 1982.

[12] R. L. Cooley. Incorporation of Prior Information on Parameters into Nonlinear Regression of Groundwater Flow Models: 2. Application. *Water Resour. Res.*, 19 (3):662–676, 1983.

[13] J. Carrera and S. P. Neuman. Estimation of Aquifer Parameters under Transient and Steady State Conditions: 1. Maximum Likelihood Method Incorporating Prior Information. *Water Resour. Res.*, 22(2):199210, 1986a.

[14] P. K. Kitanidis. Generalized Priors in Bayesian Inversion Problems. *Adv. Water Resour.*, 36:3–10, 2012. doi: 10.1029/WR022i002p00199.

[15] J. P. Delhomme. Kriging in the Hydrosciences. *Adv. Water Resour.*, 1(5):251–266, 1978. doi: 10.1016/0309-1708(78)90039-8.

[16] B. J. Wagner. Sampling Design Methods for Groundwater Modeling under Uncertainty. *Water Resour. Res.*, 31(10):2581–2591, 1995. doi: 10.1029/95WR02107.

[17] T. Asefa, M. W. Kemblowski, G. Urroz, M. McKee, and A. Khalil. Support Vectorsbased Groundwater Head Observation Networks Design. *Water Resour. Res.*, 40:W11509, 2004. doi: 10.1029/2004WR003304.

[18] G. M. C. M. Janssen, J. R. Valstar, and A. E. A. T. M. van der Zee. Measurement Network Design Including Traveltime Determinations to Minimize Model Prediction Uncertainty. *Water Resour. Res.*, 44:W02405, 2008. doi: 10.1029/2006WR005462.

[19] J. Doherty and D. Welter. A Short Exploration of Structure Noise. *Water Resour. Res.*, 46:W05525, 2010. doi: 10.1029/2009WR008377.

[20] D. A. Zimmerman and et al. A Comparison of Seven Geostatistically Based Inverse Approaches to Estimate Transmissivities for Modeling Advective Transport by Groundwater Flow, journal=Water Resour. Res., volume=34, year=1998, pages=1373-1413, number=6, doi=10.1029/98WR00003.

[21] R. J. Hunt, J. Doherty, and M. J. Tonkin. Are Models Too Simple? Arguments for Increased Parameterization. *Ground Water*, 45(3):254262, 2007. doi: 10.1111/j.1745-6584.2007.00316.x.

[22] M. Tonkin and J. Doherty. Calibration-constrained Monte Carlo Analysis of Highly Parameterized Models Using Subspace Techniques. *Water Resour. Res.*, 45: W00B10, 2009. doi: 10.1029/2007WR006678.

[23] X. Liu and P. K. Kitanidis. Large-scale Inverse Modeling with and Application in Hydraulic Tomography. *Water Resour. Res.*, 47:W02501, 2011. doi: 10.1029/2010WR009144.

[24] S. A. McKenna and E. P. Poeter. Field Example of Data Fusion in Site Characterization. *Water Resour. Res.*, 31(12):32293240, 1995. doi: 10.1029/95WR02573.

[25] N.-Z. Sun, M. C. Jeng, and W. W.-G. Yeh. A Proposed Geological Parameterization Method for Parameter Identification in Three-dimensional Groundwater Modeling. *Water Resour. Res.*, 31(1):89102, 1995. doi: 10.1029/94WR02276.

[26] S. P. Tsou, M.-S.and Perkins, X. Zhan, D. O. Whittemore, and L. Zheng. Inverse Approaches with Lithologic Information for A Regional Groundwater System in Southwest Kansas. *J. Hydrol.*, 318:292300, 2006. doi: 10.1016/j.jhydrol.2005.06.027.

[27] R. M. Gailey, A. S. Crowe, and S. M. Gorelick. Coupled Process Parameter Estimation and Prediction Uncertainty Using Hydraulic Head and Concentration Data. *Adv. Water Resour.*, 14(5):301314, 1991. doi: 10.1016/0309-1708(91)90041-L.

[28] A. Medina and J. Carrera. Coupled Estimation of Flow and Solute Transport Parameters. *Water Resour. Res.*, 32(10):30633076, 1996. doi: 10.1029/96WR00754.

[29] E. R. Anderman, M. C. Hill, and E. P. Poeter. Two-dimensional Advective Transport in Groundwater Flow Parameter Estimation. *Ground Water*, 34(6):10011009, 1996. doi: 10.1111/j.1745-6584.1996.tb02165.x.

[30] R. Weiss and L. Smith. Parameter Space Methods in Joint Parameter Estimation for Groundwater Flow Models. *Water Resour. Res.*, 34(4):647661, 1998a. doi: 10.1029/97WR03467.

[31] D. W. Hyndman, J. M. Harris, and S. M. Gorelick. Coupled Seismic and Tracer Test Inversion for Aquifer Property Characterization. *Water Resour. Res.*, 30(7): 19651977, 1994. doi: 10.1029/94WR00950.

[32] F. Day-Lewis, J. W. Lane, and S. M. Gorelick. Combined Interpretation of Radar, Hydraulic, and Tracer Data from a Fractured-rock Aquifer. *Hydrogeol. J.*, 14(1-2): 114, 2006. doi: 10.1007/s10040-004-0372-y.

[33] S. M. Ronayne, M. J.and Gorelick and J. Caers. Identifying Discrete Geologic Structures that Produce Anomalous Hydraulic Response: An Inverse Modeling Approach. *Water Resour. Res.*, 44:W08426, 2008. doi: 10.1029/2007WR006635.

[34] M. Camporese, G. Cassiani, R. Deiana, and P. Salandin. Assessment of Local Hydraulic Properties from Electrical Resistivity Tomography Monitoring of a Three-dimensional Synthetic Tracer Test Experiment. *Water Resour. Res.*, 47:W12508, 2011. doi: 10.1029/2011WR010528.

[35] A. D. Woodbury and L. Smith. Simultaneous Inversion of Hydrogeologic and Thermal Data: 2. Incorporation of Thermal Data. *Water Resour. Res.*, 24(3):356–372, 1988. doi: 10.1029/WR024i003p00356.

[36] H. R. Bravo, F. Jiang, and R. J. Hunt. Using Groundwater Temperature Data to Constrain Parameter Estimation in a Groundwater Flow Model of a Wetland System. *Water Resour. Res.*, 38(8):1153, 2002. doi: 10.1029/2000WR000172.

[37] H. R. Bravo, F. Jiang, and R. J. Hunt. Heat as a Groundwater Tracer. *Ground Water*, 43(6):951968, 2005. doi: 10.1111/j.1745-6584.2005.00052.x.

[38] R. W. Nelson. In Place Measurement of Permeability in Heterogeneous Media: 1. Theory of a Proposed Method. *J. Geophys. Res.*, 65:17531760, 1960. doi: 10.1029/JZ065i006p01753.

[39] R. W. Nelson. In Place Measurement of Permeability in Heterogeneous Media: 2. Experimental and Computational Considerations. *J. Geophys. Res.*, 66:24692478, 1961. doi: 10.1029/JZ066i008p02469.

[40] R. W. Nelson. In Place Determination of Permeability Distribution of Heterogeneous Porous Media through Analysis of Energy Dissipation. *Soc. Pet. Eng. J.*, 3: 3342, 1968.

[41] D. Kleinecke. Use of Linear Programing for Estimating Geohydrologic Parameters of Groundwater Basins. *Water Resour. Res.*, 7(2):367374, 1971.

[42] W. W.-G. Yeh, Y. S. Yoon, and K. S. Lee. Aquifer Parameter Identification with Kriging and Optimum Parametrization. *Water Resour. Res.*, 19(1):225233, 1983. doi: 10.1029/WR019i001p00225.

[43] N.-Z. Sun. *Inverse Problems in Groundwater Modeling, Theory Appl. Transp. Porous Media, vol. 6.* Kluwer Acad., Dordrecht, Netherlands, 1994.

[44] J. Irsa and A. N. Galybin. Stress Trajectories Element Method for Stress Determination from Discrete Data on Principal Directions. *Eng. Anal. Boundary Elem.*, 34:423432, 2010. doi: 10.1016/j.enganabound.2009.12.004.

[45] A. N. Galybin and J. Irsa. On Reconstruction of Three-dimensional Harmonic Functions from Discrete Data. *Proc. R. Soc. London, Ser. A*, 466:19351955, 2010. doi: 10.1098/rspa.2009.0471.

[46] J. Irsa. *Stress Trajectories Element Method and Its Modifications for Potential Problems Reconstruction, PhD thesis.* Wessex Inst. of Technol., Univ. of Wales, Ashurst, U. K., 2011.

[47] V. Shevnin, O. Delgado-Rodrguez, A. Mousatov, and A. Ryjov. Estimation of Hydraulic Conductivity on Clay Content in Soil Determined from Resistivity Data. *Geofsica Internacional*, 45(3):195–207, 2006.

[48] J. F. Zhu and T. C. J. Yeh. Characterization of Aquifer Heteroography. *Water Resour. Res.*, 41:W07028, 2005. doi: 10.1029/2004WR003790.

[49] Deqiang Mao, Tian-Chyi J. Yeh, Li Wan, Kuo-Chin Hsu, Cheng-Haw Lee, and Jet-Chau Wen. Necessary Conditions for Inverse Modeling of Fow through Variably Saturated Porous Media. *Adv. Water Resour.*, 52:50–61, 2013.

[50] Toshihiro Sakaki, Christophe C. Frippiat, and Tissa H. Illangasekare. On the Value of Lithofacies Data for Improving Groundwater Flow Model Accuracy in a Three-dimensional Laboratory-scale Synthetic Aquifer. *Water Resour. Res.*, 45:W11404, 2009. doi: 10.1029/2008WR007229.

[51] Geir Evensen. *Data Assimilation: The Ensemble Kalman Filter.* Springer, New York, 2 edition, 2009.

[52] Michael J. Pyrcz and Clayton V. Deutsch. *Geostatistical Reservoir Modeling.* Oxford University Press, New York, 2 edition, 2014.

[53] C. V. Deutsch and A. G. Journel. *Geostatistical Software Library and Users Guide (GSLIB)*. Oxford University Press, New York, 1998.

[54] M. Wang and C. Zheng. Aquifer Parameters Estimation under Trasient and Steady-state Conditions Using Genetic Algorithms. *in Calibration and Reliability in Groundwater Modeling, Proceedings of the Model-CARE 96 Conference*, 237: 21–30, 1996.

[55] J. Morshed and J. J. Kaluarachchi. Parameter Estimation Using Artficial Neural Network and Genetic Algorithm for Free-product Migration and Recovery. *Water Resour. Res.*, 34(5):1101–1113, 1998. doi: 10.1029/98WR00006.

[56] En-Jui Lee, He Huang, John M. Dennis, Po Chen, and Liqiang Wang. An Optimized Parallel LSQR Algorithm for Seismic Tomography. *Computers and Geosciences*, 61:184–197, 2013.

[57] J.N. Sharma. *Numerical Methods for Engineers and Scientists*. Alpha Science, Oxford, U.K., 2 edition, 2007.

[58] He Huang, Liqiang Wang, En-Jui Lee, and Po Chen. An MPI-CUDA Implementation and Optimization for Parallel Sparse Equations and Least Squares (LSQR). *the 2012 International Conference on Computational Science (ICCS)(main track)*, 2012.